DISSERTATION

BIOPHYSICAL STUDIES OF MOTIONS AND INTERACTIONS OF MEMBRANE PROTEINS

Submitted by

Peter William Winter

Graduate Degree Program in Cell and Molecular Biology

In partial fulfillment of the requirements

For the Degree of Doctor of Philosophy

Colorado State University

Fort Collins, Colorado

Fall 2011

Doctoral Committee:

Advisor: B. George Barisas
Co-Advisor: Deborah A. Roess

Debbie C. Crans
James R. Bamburg

ABSTRACT

BIOPHYSICAL STUDIES OF MOTIONS AND INTERACTIONS OF MEMBRANE PROTEINS

We have utilized a variety of biophysical techniques to quantitatively examine the motions and interactions of transmembrane proteins on living cells at the single-molecule level. These include both widefield and confocal optical microscopic methods such as single particle tracking, Förster resonance energy transfer and ratiometric imaging of phase-sensitive probes of lipid order, together with spectroscopic fluctuation methods such as fluorescence correlation spectroscopy and photon counting histogram analysis. Our studies indicate that; 1. Luteinizing hormone receptors on CHO cells and KGN human granulosa cells exhibit restricted lateral diffusion and increased self-association after exposure to human chorianic gonadotropin; 2. In addition to insulin receptor and IGF1 receptor homodimers, rat basophilic leukemia 2H3 cells express significant levels of insulin receptor-IGF1 receptor heterodimers; 3. Clustering of insulin receptors after exposure to insulin on rat basophilic leukemia 2H3 cells is affected by disruption of actin-filaments but not by extraction of membrane cholesterol; 4. Chromium Picolinate and Bis(maltolato)oxovandium(IV) both restrict the lateral diffusion of insulin receptors on rat basophilic leukemia cells and; 5. Individual Fcε receptors on rat basophilic leukemia cells exhibit orientation fluctuations on millisecond timescales.

ACKNOWLEDGEMENTS

Thank you to my research advisors, George Barisas and Deborah Roess and my graduate committee for their guidance and support during my time at Colorado State University. Thank you to Nancy Levinger and Alan Van Orden for their support of my research endeavors. Thank you to Lori Williams and Janet Moder for their kindness and support. Thank you to Guy Hagen and Ivan Raska for allowing me the opportunity to collaborate on a series of experiments at Charles University and thank you to Pavel Krizek for his assistance during that time. Thank you to the members of the Barisas/Roess and Van Orden research groups past and present for their assistance and kindness during my time here. Thank you to Tim Formosa for his guidance during my time at University of Utah. Thank you to Peter Thorsness for his guidance and support during my time at University of Wyoming and a special thank you to Neena Grover and the faculty of the chemistry department for their guidance and support during my time at Colorado College. Finally, thank you to Michael Tivilini and Sheila McCarthy for their guidance and support during my time at Whitfield School. This work was supported in part by grants CHE0628260 and MCB1024669 from the National Science Foundation and grant RR023156 from the National Institutes of Health.

Dedication

This dissertation is dedicated to my family for their guidance and unwavering support.

TABLE OF CONTENTS

INTRODUCTION

BIOPHYSICAL STUDIES OF MOTIONS AND INTERACTIONS OF MEMBRANE PROTEINS

We have utilized a variety of biophysical techniques to quantitatively examine the motions, interactions and local environments of transmembrane proteins on living cells at the single-molecule level. These include both widefield and confocal optical microscopic methods such as single particle tracking, Förster resonance energy transfer and ratiometric imaging of phase-sensitive probes of lipid order, together with spectroscopic fluctuation methods such as fluorescence correlation spectroscopy and photon counting histogram analysis.

The quantitative examination of the motions, interactions and local environment of membrane proteins, particularly transmembrane receptor proteins, is of considerable interest to both scientists and medical professionals. Since the introduction of the fluid mosaic model describing biological membranes by Singer and Nicolson in the early 1970's [1], which built on the work of Frye and Edidin [2] and of Loor et al. [3], it has become evident that changes in the motions and interactions of membrane-localized proteins in response to extracellular or cytoplasmic chemical species significantly affects the behavior of live cells.

Increased interest in the complex and heterogeneous composition of biological membranes has followed. Originally proposed by Simons and Ikonen [4], the "lipid raft" hypothesis suggests that certain lipids and amphipathic molecules self-associate in biological

membranes creating a variety of both highly transient and semi-permanent membrane structures of differing size and composition. More recently, it has been established that, in addition to the effects of lipid-delineated structures such as lipid rafts, the behavior of membrane-localized proteins is also regulated by cytoskeletal structures such as actin filaments [5]. These subsurfaceactin and actin-associated protein structures compartmentalize membrane proteins such as transmembrane receptors.

Lateral segregation of membrane proteins, such as transmembrane protein receptors, within both lipid and cytoskeletal delineated membrane structures has been shown to play a significant role in the regulation of cell signaling events. This appears to arise from the increased likelihood of receptor aggregation or interactions with other membrane localized species while confined within such structures. Binding of ligands or other regulatory molecules along with compositional changes in the membrane itself often initiate changes in the motions and interactions of membrane proteins such as transmembrane receptor proteins.

Herein, we describe the application of both microscopic and spectroscopic biophysical methods to quantitate the effects of ligand binding and membrane composition on the motions and interactions of several transmembrane receptor proteins. Often it is only with biophysical methods such as these that meaningful information regarding dynamics of individual molecules on living cells can be obtained. Our studies indicate that luteinizing hormone receptors, insulin receptors, insulin-like growth factor one receptors and the high affinity IgE receptor all exhibit significant changes in either their motions or interactions with other lipids and proteins after exposure to receptor-specific ligands or to reagents that alter membrane composition.

[1] S.J. Singer and G.L. Nicolson, The fluid mosaic model of the structure of cell membranes. Cell membranes are viewed as two-dimensional solutions of oriented globular proteins and lipids Science 175 (1972) 720-731.

[2] L.D. Frye and M. Edidin, The rapid intermixing of cell surface antigens after formation of mouse-human heterokaryons Journal of Cell Science 7 (1970) 319-335.

[3] F. Loor, Lectin-induced lymphocyte agglutination. An active cellular process? Experimental Cell Research 82 (1973) 415-425.

[4] K. Simons and E. Ikonen, Functional rafts in cell membranes Nature 387 (1997) 569-572.

[5] K. Ritchie, R. Iino, T. Fujiwara, K. Murase and A. Kusumi, The fence and picket structure of the plasma membrane of live cells as revealed by single molecule techniques (review) Molecular Membrane Biology 20 (2003) 13-18.

CHAPTER I: Peter W. Winter performed fluorescence correlation spectroscopy shown in Figure 4 and Figure 5 and photon counting histogram analysis shown in Table 5.

RESTRICTED LATERAL DIFFUSION OF LUTEINIZING HORMONE RECEPTORS IN MEMBRANE MICRODOMAINS

Amber L. Wolf-Ringwall[1,*], Peter W. Winter[2,*], Jingjing Liu[3], Alan K. Van Orden[4], Deborah A. Roess[1,2] and B. George Barisas[2,4]

[1]Department of Biomedical Sciences, Colorado State University, Fort Collins, CO 80523, [2]Cell and Molecular Biology Program, Colorado State University, Fort Collins, CO 80523, [3]Tufts Medical Center, Boston, MA 02111, [4]Department of Chemistry, Colorado State University, Fort Collins, CO 80523, *These authors contributed equally.

Running title: Restricted Diffusion of Luteinizing Hormone Receptors

Address all correspondence and requests for reprints to: B. George Barisas, Department of Chemistry, Colorado State University, Fort Collins, CO 80523. Phone: (970) 491-6641 Fax: (970) 491-1801 e-mail: barisas@lamar.colostate.edu

Single particle tracking was used to evaluate lateral motions of individual FLAG-tagged human luteinizing hormone (LH) receptors expressed on Chinese hamster ovary (CHO) cells and native LH receptors on both KGN human granulosa-derived tumor cells and M17 human neuroblastoma cells before and after exposure to human chorionic gonadotropin (hCG). Compared to LH receptors on untreated cells, LH receptors on cells treated with 100 nM hCG exhibit restricted lateral diffusion and are confined in small, nanometer-scale, membrane compartments. Like LH receptors labeled with Au-hCG, LH receptors labeled with Au-deglycosylated hCG, an hCG antagonist, also exhibit restricted lateral diffusion and are confined in nanoscale membrane compartments on KGN cells treated with 100 nM hCG. LH receptor point mutants lacking potential palmitoylation sites remain in large compartments despite treatment with 100 nM hCG as do LH receptors on cells treated with cytochalasin D. Finally, both polarization homo-transfer fluorescence resonance energy transfer imaging and photon counting histogram analysis indicate that treatment with hCG induces aggregation of YFP-coupled LH receptors stably expressed on CHO cells. Taken together, our results demonstrate that binding of hCG induces aggregation of LH receptors within nanoscale, cell-surface membrane compartments, that hCG binding also affects the lateral motions of antagonist binding LH receptors, and that receptor surface densities must be considered in evaluating the extent of hormone-dependent receptor aggregation.

Signal transduction by luteinizing hormone[1] (LH) receptor plays an essential role in the normal reproductive function of both male and female mammals by promoting ovulation, follicle maturation, corpus luteum formation and steroidogenesis. LH receptor signaling in response to saturating concentrations of LH or human chorionic gonadotropin (hCG) involves

substantial changes in receptor lateral and rotational dynamics (1,2) as well as the association of LH receptors with membrane rafts (3). Fluorescence resonance energy transfer (FRET) techniques (4) and electron microscopy (5) indicate that functional hormone-receptor complexes can also become self-associated into dimers/oligomers following ligand binding. Previous experimental strategies have examined changes in receptor motions on collections of cells or large numbers of fluorescently-tagged molecules on single cells. It is now possible, however, to examine the lateral motions of *individual* LH receptors on living cells using microscope-based single particle tracking (SPT) techniques (6).

Although the mechanism involved in retention of hCG-occupied LH receptors in small membrane compartments is still unclear, exposure to saturating concentrations of hCG results in confinement of the majority of LH receptors within small cell-surface compartments. LH receptors remain within these compartments for comparatively long times and appear to diffuse pseudo-randomly before being captured within another compartment of similar size (7). Similar behavior has been described and analyzed by Kusumi and coworkers (6) for selected phospholipids and for transferrin receptors (8) and by Daumas and coworkers (9) for the μ opioid receptor. Daumas argues that the μ opioid receptor can both diffuse within the bulk membrane and exhibit confinement within a microdomain that itself diffuses slowly. Kusumi and coworkers (6) suggest that particles may be confined by proteins forming a barrier that is either continuous or discontinuous, leading to receptor diffusion within small membrane regions accompanied by intermittent escape from compartments and periods of unrestricted diffusion in the bulk membrane.

Our previous studies of LH receptor lateral and rotational diffusion suggest that actin microfilaments or membrane protein interactions with the cytoskeleton may provide organizing structures that restrict the lateral motions of receptors (1,2). However, the mechanism of hormone-initiated LH receptor confinement in small compartments has not previously been examined in detail at the single molecule level. In the present work, we compared the lateral

dynamics of individual LH receptors that were either FLAG-tagged and identified using FLAG-specific antibodies with the diffusion of native receptors occupied by gold nanoparticle-hCG conjugates (Au-hCG) or Au-deglycosylated DG-hCG (Au-DG-hCG). The latter material is an hCG antagonist (10) that binds LH receptors with high affinity and can block hCG binding for more than 24 hrs (11). This allowed us to determine whether LH receptor motions are dependent on hCG concentration and limited to hCG-occupied receptors or, alternatively, whether hCG binding to a fraction of available receptors has global effects on LH receptor diffusion regardless of whether they have been activated by hCG. We also explored whether point mutations to palmitoylation sites on the LH receptor C-terminus, known to eliminate LH receptor translocation into membrane rafts (12) affected receptor confinement within small compartments and to what extent the actin cytoskeleton is responsible for the restriction of LH receptor lateral motions. Because slower lateral diffusion may result from extensive self-association of membrane proteins, polarization homo-transfer FRET (homoFRET) and photon counting histogram (PCH) analysis were utilized to evaluate increased oligomerization of YFP-coupled human LH receptors (YFP-LHR) stably expressed on individual, viable, CHO cells in response to increasing concentrations of hCG. Fluorescence correlation spectroscopy (FCS) was used to determine the equilibrium dissociation constant (K_D) of hCG binding to native LH receptors on KGN cells and to estimate the number of native LH receptors on these cells. FCS was also used estimate the number of YFP-LHR stably expressed on the CHO cells used in homoFRET and PCH analysis studies. Finally, we considered how changes in receptor cell surface density might contribute to the apparent aggregation of YFP-LHR stably expressed on CHO cells.

EXPERIMENTAL PROCEDURES

Materials and cell culture ─ CHO cells were maintained in high glucose Dulbecco's Modification of Eagle's Medium (DMEM) (Mediatech, Inc., Manassas, VA) supplemented with 10% fetal bovine serum (FBS), 2 mM L-glutamine, 100 units of penicillin/ml, 100 μg

streptomycin/ml (Gemini Bio-Products, Woodland, CA) and 1x MEM non-essential amino acid solution (Sigma-Aldrich, Inc., St. Louis, MO). KGN cells, a human granulosa-like tumor cell line developed by Dr. Yoshihiro Nishi and Dr. Toshihiko Yanase at Kyusyu University (13), were kindly provided by Dr. James Dias at the Wadsworth Center (New York State Department of Health, Albany, NY). KGN cells were maintained in DMEM/Ham's F12 medium supplemented with 10% FBS, 2 mM L-glutamine and 100 units of penicillin/mL as previously described (13). M17 human neuroblastoma cells which express LH receptors (14) were purchased from ATCC (Manassas, VA) and maintained in Minimum Eagle's Medium (MEM)/Ham's F12 medium (Mediatech, Inc., Manassas, VA) supplemented with 10% FBS, 2 mM L-glutamine, 100 units of penicillin/mL, 100 μg streptomycin/mL (Gemini Bio-Products, Woodland, CA), 1.5 g/L sodium bicarbonate, 1 mM sodium pyruvate and 0.1 mM MEM non-essential amino acid solution (Sigma-Aldrich, Inc., St. Louis, MO). All cells were grown in 5% CO_2 at 37ºC in a humidified environment. Geneticin (G418 sulfate) was purchased from Mediatech, Inc. (Manassas, VA). Monoclonal anti-FLAG antibody directed against the FLAG epitope tag was purchased from Sigma-Aldrich, Inc. (St. Louis, MO). 40 nm gold colloid was obtained from Ted Pella, Inc. (Redding, CA). Highly purified hCG (Fitzgerald Industries, Inc., Concord, MA) was prepared in 1x PBS. Dr. George Bousfield, Wichita State University, kindly provided deglycosylated hCG used in single particle tracking studies on KGN and M17 cells. Deglycosylated hCG was prepared using modifications of the method described by Edge et al. (15). Rather than using a desalting column as described, deglycosylated protein was incubated in 0.5 M sodium acetate buffer, pH 6.0, overnight at 37 C to re-associate dissociated subunits and the heterodimer fraction was then isolated using Superdex 75 gel filtration chromatography. To monitor the extent of LH receptor signaling in M17 cells, levels of intracellular cAMP were assessed following exposure to hCG using a TiterFluor Direct Cyclic AMP Enzyme Immunoassay Kit (Assay Designs, Ann Arbor, MI).

CHO cell lines expressing FLAG or YFP tags ─ Dr. K.M. Menon from the University of Michigan kindly provided us with N-terminal FLAG-tagged LHR subcloned into the pFLAG vector (FLAG-LHR) (Sigma-Aldrich, Inc., St. Louis, MO). A stable cell line expressing FLAG-tagged palmitoylation-deficient LH receptors was prepared as previously described (12). For homoFRET, FCS and PCH experiments, we used a stable CHO cell line expressing human YFP-LHR at the C-terminus as previously described (16).

Single particle tracking of individual LH receptors on live cells ─ Lateral dynamics and the size of compartments accessed by individual FLAG-LHR on CHO cells or native LH receptors on KGN and M17 cells were evaluated using single particle tracking methods as described by Kusumi and coworkers (17). To identify FLAG-LHR, 40 nm nanogold particles were conjugated with a mixture of anti-FLAG monoclonal antibody and BSA at the lowest possible total protein concentration, typically 40 μg/mL, needed to stabilize the gold solution. To identify individual native LH receptors expressed on KGN or M17 cells, 40 nm gold particles were coupled to Au-hCG or Au-DG-hCG using the same protocol. For labeling cells, the ratio of antibody or hormone to BSA, typically 1:100 by weight, was selected to give 10 to 20 particles bound per cell. The binding of anti-FLAG antibody or hormone was specific: when cells were preincubated with a 10-fold excess of anti-FLAG antibody or Au-tagged hormone, no gold particles were detected on cells. Cells were labeled with Au-coupled probes for 1 hour at 4°C. After receptor labeling, cells were treated with 0.1 nM, 1 nM or 100 nM hCG for 1 hour at 37°C. Because the off rates for hCG and DG-hCG are on the order of 24-48 hours (11,18), it is unlikely that Au-tagged hormones were displaced from LH receptors by introduction of hCG on the timescale of these experiments. In some experiments, cells grown on coverslips placed in 60 mm^2 petri dishes were pre-treated with 40 μg/mL cytochalasin D for 1 hour prior to labeling with gold-conjugated anti-FLAG antibody.

Individual gold nanoparticles were imaged by differential interference contrast using a 1.4 N.A. 63x oil objective in a Zeiss Axiovert 135 TV inverted microscope. Images were

acquired using a Dage IFG-300 camera and were recorded for two minutes (3600 frames) at approximately 30 nm/pixel under the control of Metamorph software (Molecular Devices). Trajectories of individual gold particles were measured over time and then segmented into compartments by calculation of statistical variance in particle position (6,9,19). The variance of a particle's position was calculated within windows of varying duration which were translated along the particle trajectory, producing a variance plot that exhibited peaks indicating inter-compartment boundaries. These results were analyzed using custom analysis programs to yield the compartment size and residence time for each particle. Effective macroscopic diffusion coefficients (D) were calculated as the square of the compartment diagonal divided by four times the residence time in the compartment as previously described (19). Data are presented either as the mean ± S.E.M. or mean ± S.D. as indicated in the figure legends. Significance was assessed using Student's t-test and p values are indicated ($p < 0.05$).

Polarization homo-transfer FRET measurements ─ We investigated aggregation of human LH receptors in response to 0.1 nM, 1 nM and 100 nM hCG using polarization homo-transfer FRET or energy migration FRET. Homo-transfer FRET assesses energy transfer between identical fluorescent donor and acceptor molecules by measuring fluorescence anisotropy as probe molecules are photobleached (20). Increasing anisotropy as probe molecules are progressively photobleached is indicative of FRET. CHO cells stably expressing YFP-LHR were plated overnight in Willco 35 cm^2 #1.5 glass bottom petri dishes (Warner Instruments, Hamden, CT). FRET between YFP molecules on single cells were analyzed using an Olympus FV 300 confocal microscope with a polarizing beam splitter placed in front of the detection PMTs, allowing two orthogonally-polarized fluorescence images to be recorded simultaneously. YFP was excited with the 488 nm line of an argon laser and appropriate barrier and dichroic filters were selected for YFP emission. Individual cells with ring-like fluorescence from YFP at their plasma membrane were imaged. A sequence of cell images, typically about 20, was obtained as YFP was progressively photobleached until approximately 10% of the initial average

intensity remained. Each anisotropy measurement was accompanied by acquisition of g-factor and background images. Imaging analysis was performed with custom analysis programs. Total intensity (s) and fluorescence anisotropy (r) were calculated as $s=I_{\parallel} + 2I_{\perp}$ and $r=(I_{\parallel} - I_{\perp})/s$, where $I_{\parallel}$ and $I_{\perp}$ are fluorescence emission polarized parallel and perpendicular, respectively, to the polarization of linearly polarized excitation light (21,22).

Fluorescence correlation spectroscopy and photon counting histogram analysis ─ PCH analysis was used to evaluate oligomerization of YFP-LHR stably expressed on CHO cells in response to increasing concentrations of hormone. The related technique FCS was used to determine the K_D of hCG binding to native LH receptors on KGN cells and obtain estimates of the number of LH receptors on KGN cells and on CHO cells expressing YFP-LHR. KGN cells were seeded onto sterile dishes, grown to 50% confluence, washed, and treated with 0.01 – 500 nM hCG for 45 min. Cells were then washed and sequentially treated with anti-hCG rabbit IgG (Upstate) for 30-40 min, 600 nM anti-rabbit-biotin IgG (Sigma) for 30 min, and 600 nM FITC-avidin for 20 min before observation. CHO cells stably expressing YFP-LHR were grown to 50% confluence on sterile dishes and examined directly. Both FCS and PCH experiments were performed on a modified Nikon TE1000 inverted microscope equipped with a 100x, 1.25 NA, oil-immersion objective, an Omnichrome Melles-Griot multi-line air-cooled argon ion laser operating at 514.5 nm, two 570/32 nm bandpass filters, two PerkinElmer single photon counting modules (SPCM-AQR-14), an ALV-6010 digital hardware correlator and a Becker and Hickl GmbH PMS-400 multichannel photon counter as previously described (23). The $1/e^2$ radius of the excitation beam at the sample was experimentally determined to be 241 nm using aqueous rhodamine 6G. In live cell studies, the laser excitation beam was vertically positioned on the apical cell membrane by adjusting the objective z-position to maximize detector count rates and minimize diffusional correlation times (τ_D) as described by Ries and Schwille (24). All FCS and PCH experiments were conducted at room temperature. In both FCS and PCH experiments samples were illuminated for approximately 10 sec before collection of data to allow for the

irreversible photobleaching of immobile particles (25). FCS data were then collected for two consecutive 10 sec intervals, while PCH data were collected for 30 sec. During acquisition of FCS and PCH data the average fluorescence from the sample was relatively uniform as indicated by the avalanche photodiode signal readouts. Analysis of FCS data, including determination of τ_D and the normalized initial $g(\tau)$ were accomplished according to established procedures using Igor Pro 5.05A (24,26-28). Using FCS, the number of receptors per μm^2 was determined from the effective number of correlating particles detected in the illuminated area (N_{eff}) at saturating concentrations of fluorophore conjugated receptor-specific probe and the radius of the laser interrogation area. The K_D for hCG was determined by fitting FCS data to a hyperbolic function describing a single-site binding model. For PCH, detected photons were accumulated into successive 1 μs counting channels and rebinned into 9 μs channels to improve signal-to-noise. Rebinned photon counts were then simultaneously subjected to autocorrelation, pseudo-crosscorrelation and PCH. Weighted least-squares fitting was used to obtain estimates of N_{eff}, the average molecular brightness (ε) of detected particles and the out-of-focus emission ratio (F) as previously described (29-31).

RESULTS

Reduced lateral diffusion and increased compartmentalization of LH receptors follows treatment with hCG ─ Single particle tracking methods were used to examine the lateral diffusion of individual LH receptors and receptor compartmentalization in response to binding of hCG (Figure 1.1). Treating CHO cells expressing FLAG-LHR with 0.1 nM hCG did not have a statistically significant effect on either receptor diffusion (lower panel) or average size of compartments containing LH receptors (upper panel). However 1 nM hCG and 100 nM hCG significantly increased the number of receptors appearing in compartments of less than 100 nm in diameter to 62% and 91% of the total receptor population, respectively (Figure 1.2). Individual

FLAG-LH receptors on cells treated with 100 nM hCG, also exhibited significantly slower lateral diffusion (Figure 1.1, lower panel).

To examine the lateral dynamics of native LH receptors on viable KGN granulosa-like tumor cells and M17 human neuroblastoma cells, 10-20 receptors per cell were tagged with Au-hCG. When KGN cells were exposed to 1 nM and 100 nM unlabeled hCG, Au-tagged LH receptors became confined in small membrane compartments of less than 100 nm diameter (Figure 1, upper panel). For cells treated with 0.1 nM hCG, 16% of hCG-occupied LH receptors on KGN cells were confined in these small compartments and this number increased to 48% when cells were treated with 100 nM hCG. The diffusion rate of individual LH receptors was also reduced from 0.7±0.2 $x10^{-11}cm^2sec^{-1}$ to 0.3±0.1 $x10^{-11}cm^2sec^{-1}$ after 100 nM hCG treatment (Table 1.1). We observed similar dose-dependent effects of hCG on the diameter of compartments accessed by hCG-occupied LH receptors on M17 neuroblastoma cells. With increasing concentrations of hCG, more Au-hCG occupied LH receptors were confined in small membrane compartments. Au-hCG occupied LH receptors on cells treated with 100 nM were located in smaller compartments with an average diameter of 131±18 nm. In M17 cells the average rate of diffusion was reduced from 0.9±0.3 $x10^{-11}cm^2sec^{-1}$ to 0.4±0.1 $x10^{-11}cm^2sec^{-1}$ after treatment with 100 nM hCG (Table 1.2).

Activation of LH receptors also resulted in increased levels of intracellular cAMP. There was a 1.6±0.2-fold and a 2.5±0.9-fold increase in cAMP response over basal levels, respectively, in response to treatment with 100 nM hCG and 20 nM forskolin.

Non-functional receptor complexes exhibit reduced lateral diffusion and increased compartmentalization in response to hCG ─ Differences in the effects of hCG on the lateral motions of FLAG-LHR and native receptors on KGN and M17 cells were anticipated, particularly at lower hormone concentrations. When cells are treated with lower concentrations of hCG, FLAG-tagged receptors are not necessarily occupied by hCG. In contrast, *only* Au-hCG-occupied receptors are examined in single particle tracking of receptors on KGN and M17 cells.

To determine whether hCG binding to LH receptors produced global effects on LH receptor motions or, alternatively, affected only hCG-occupied receptors, native LH receptors on KGN cells were labeled with 10-20 Au-DG-hCG molecules as probes for non-signaling receptors. Compared to Au-hCG occupied LH receptors, Au-DG-hCG occupied LH receptors exhibited relatively faster lateral diffusion within somewhat larger 217±27 nm diameter regions. When KGN cells were treated with 100 nM hCG, Au-DG-hCG occupied receptors also exhibited significantly slower lateral diffusion and became confined in smaller compartments, although neither receptor lateral diffusion nor average compartment size were affected by hormone treatment to the same extent as seen for Au-hCG occupied receptors. The results from these experiments are summarized in Table 1.1.

Mutation of palmitoylation sites on LH receptors or disruption of actin microfilaments prevents hormone-mediated receptor confinement ─ We examined LH receptor lateral motions and confinement in small compartments on cells expressing LH receptors in which cysteine was mutated to serine at positions 621 and 622 (LHR-C621, 622S), previously described as palmitoylation sites for the LH receptor (32,33). The average values for the compartment diameters accessed by either untreated or hCG-treated LHR-C621, 622S are approximately 200 nm (Table 1.3). In addition, FLAG-LHR on CHO cells treated with 40 μg/mL cytochalasin D, an actin-filament disrupter (34-37), exhibit fast lateral diffusion within large compartments both before and after exposure to 100 nM hCG. After treatment with cytochalasin D, hCG had no effect on the average diffusion coefficient or the average compartment diameter accessed by FLAG-LHR. This may be a result of the disruption of cell-surface compartments defined by cytoskeletally-anchored proteins (38). Individual LHR-C621, 622S were also generally not confined in small compartments although their diffusion coefficients were slower than those of either untreated wild type LH receptors or LH receptors on cells treated with cytochalasin D (Table 1.3).

Human LH receptors self-associate in response to increasing concentrations of hCG — Aggregation of LH receptors in response to hormone treatment was assessed using CHO cells stably expressing YPF-LH receptors and both homo-transfer FRET confocal imaging and PCH analysis (39). In homo-FRET studies, fluorescence emission anisotropy was measured as YFP molecules were irreversibly photobleached. Progressive loss of YFP molecules via irreversible photobleaching reduces the likelihood that two YFP molecules are in close proximity to one another and available for resonance energy transfer. Thus the anisotropy of fluorescence emission will increase with increasing photobleaching of the YFP fluorophore. The average percent increase in anisotropy for untreated CHO cells expressing human YFP-LHR was 11%, 26% for cells treated with 0.1 nM hCG, 36% for cells treated with 1 nM hCG and 54% for cells treated with 100 nM hCG (Figure 1.3). FRET efficiencies (E), calculated as described by Rao and Major (40), increased from about 9% for untreated cells to over 30% in response to increasing concentrations of hCG (Table 1.4).

Similarly, PCH analysis suggests that YFP-LHR undergo aggregation after exposure to hCG. The average photon counts detected per molecule per sampling time, often referred to as ε (31,41) for YFP-LHR on live CHO cells was 0.07 ± 0.01 before treatment with hCG. After treatment with increasing concentrations of hCG, the ε of detected YFP-LHR rose significantly to 0.13-0.14 (Table 1.5) suggesting increased aggregation of LH receptors in response to binding of ligand.

Finally, FCS was used to determine the number of YFP-LHR per μm^2 on the surface of the stably transfected CHO cells and to compare that to native LH receptor density on KGN cells. Figure 1.4 shows the distribution of YFP-LHR densities on individual CHO cells and indicates that the majority of these cells have LH receptor densities ranging from 10 receptors μm^{-2} to 100 receptors μm^{-2}. This was similar to the number of YFP-LHR observed during PCH analysis (Table 1.5). Also, on average, the density of LH receptors on KGN cells (Figure 1.5), which we estimate to be 86 receptors μm^{-2}, is greater than the receptor density on the transfected

CHO cells. These experiments also indicate that native LH receptors on KGN cells bind hCG with K_D of approximately 210 pM which is similar to previously determined values obtained using alternative methods (42). Using known estimates of CHO cell surface area (43), we calculate that each transfected CHO cell expresses approximately 33,000 total YFP-LHR.

DISCUSSION

We have previously shown that binding of saturating concentrations of hCG to rat LH-wt receptors results in redistribution of essentially all LH receptors from the bulk membrane into cholesterol-enriched membrane rafts (7) and that LH or hCG treatment cause a marked reduction in the fraction of mobile receptors (44). In contrast to methods used in these previous studies, single particle tracking techniques probe the lateral motions of *individual* LH receptors rather than a large population of receptors and so permit analysis of specific sub-populations of receptors exhibiting unique diffusive properties. Here we have shown that, when cells were treated with 100 nM hCG, a concentration sufficient to saturate available LH receptors, the average diffusion coefficient for individual receptors was approximately $10^{-12}cm^2sec^{-1}$. This agrees with previous measurements of lateral diffusion for LH receptors on ovine luteal cells (45) and cell lines stably expressing LH receptors covalently coupled to visible fluorescent proteins (46) where most, if not all, LH receptors binding either saturating concentrations of LH or hCG were laterally immobile on the timescale of photobleaching recovery experiments. These laterally immobile receptors had diffusion coefficients estimated to be less than $10^{-12}cm^2sec^{-1}$ (47), a practical detection limit for fluorescence photobleaching recovery measurements.

It appears that the extent of receptor occupancy by hormone is related to LH receptor retention in small compartments where individual particles exhibit slower diffusion. These should be considered distinct from membrane rafts (48) which are small microdomains within the membrane that may be transiently organized as proteins and small numbers of associated lipids or may be more persistent in the membrane (49). Hormone-treated LH receptors were not confined

in small membrane compartments when treated with cytochalasin D, a disruptor of the actin-based cytoskeleton (34-37), suggesting that the compartments evaluated with single particle tracking methods are bounded by protein fences or cytoskeletally-anchored protein networks that limit lateral diffusion of transmembrane proteins (6). It is also possible that the restriction of LH receptor lateral motions involves both lipid rafts and protein delineated networks nested in a hierarchical fashion as has recently been proposed (50).

Interestingly, individual LHR-C621,622S were generally not confined in small compartments. Nevertheless, their diffusion coefficients were slower than those of either untreated FLAG-LH receptors or FLAG-LH receptors on cells treated with cytochalasin D. Although palmitoylation-deficient mutant LH receptors are not found in rafts (12), they retain their ability to signal via cAMP (32,33) as do dopamine D1 (51) and serotonin 4a (52) receptors with similar mutations. These results suggest that either prolonged LH receptor retention in small membrane compartments is not required for LH receptor-mediated signal transduction or, alternatively, that interactions of mutant receptors with the molecular contents of small compartments are more short-lived than for wild type receptors but still sufficient to initiate downstream signaling events.

Single particle tracking studies of endogenous LH receptors demonstrated that native hCG-occupied LH receptors on KGN human granulosa or M17 human neuroblastoma cells exhibited a dose-dependent increase in receptor compartmentalization in response to increasing concentrations of hCG which, in M17 cells, corresponded to increases in cAMP. The relationship between receptor compartmentalization and cAMP signals in these neuronal tissue may be important in aging where elevated LH levels are associated with decreased cognition in animal models (53). It may also suggest a role for deglycosylated hCG or other hCG antagonists in reducing compartmentalization of LH receptors, particularly if compartmentalization of LH receptors increases local concentrations of LH receptors and contributes to declines in cognition with aging.

However, the question of whether binding of hCG has global effects on the motions and compartmentalization of both hormone-occupied and unoccupied LH receptors remains unresolved. In KGN cells, DG-hCG-tagged LH receptors were confined in smaller compartments when cells were exposed to saturating concentrations of hCG (100 nM) suggesting that some non-functional hormone-receptor complexes may redistribute into small membrane compartments together with hCG-occupied receptors. It is important to note that high concentrations of DG-hCG alone do not alter the molecular motions of LH receptors or lead to accumulation of LH receptors into small membrane microdomains. The rotational diffusion coefficients for LH receptors remain fast when receptors are occupied by DG-hCG (54) and there is no evidence of raft localization or confinement of DG-hCG occupied LH receptors in small nanoscale membrane microdomains using SPT (7). Similarly, non-functional hormone receptor complexes formed by binding of hCG to non-signaling LH receptor mutants exhibit faster rotational diffusion (54) than do functional hormone-occuped LH receptors (55), no increase in FRET in response to ligand (4) and are not confined in either raft domains or membrane microdomains examined using SPT (7). These results suggest that the slower lateral dynamics observed for Au-DG-hCG when cells are treated with hCG may result from a bystander effect on Au-DG-tagged receptors that may include direct interactions between hCG-occupied LH receptors and the Au-DG-hCG occupied receptors similar to LH receptor trans-activation described by Ji and coworkers (56).

These studies do no resolve the extent to which LH receptors may exist as pre-aggregated dimers or low molecular weight oligomers prior to binding hormone. Analysis of such structures on living cells would require single molecule methods for evaluating, for example, single molecule measurements of FRET analogous to SPT measurements of lateral diffusion. Nevertheless, it is clear that there are hCG-dependent increases in the extent of LH receptor aggregation regardless of whether the receptor exists initially as a monomer, dimer or larger structure. Using homo-transfer FRET techniques to evaluate interactions between stably expressed YFP-LHR, we show that hormone-treated LH receptors exhibit a higher degree of self-

association than untreated LH receptors and that the extent of receptor interactions is dependent on hormone concentrations. Similar results were also observed in PCH analysis of changes in ε of YFP-LHR aggregation on CHO cells after hormone treatment.

The hCG-dependent increase in ε also argues against a conformational change in LH receptors leading to increased FRET. There have, in addition, been previous observations of FRET made using fluorescein isothiocyanate (FITC)-hCG and tetramethylrhodamine isothiocyanate (TrITC)-hCG as a donor/acceptor pair under conditions where the formation of large molecular weight complexes containing LH receptors was assessed. Using membrane preparations from porcine granulosa cells, the GTP-dependent progression from "active" LH receptors to "desensitized" LH receptors was accompanied by an increase in FRET efficiency from values less than 1% to over 10%. Increased FRET efficiency was accompanied by slower receptor rotational dynamics indicative of receptors within large molecular weight structures (57). Because both active and desensitized LH receptors in these studies were occupied by hCG, the absence of FRET between "active" receptors also suggests that FRET does not result from an agonist-stabilized receptor conformation.

Importantly, the surface density of stably-transfected LH receptors on these CHO cells was comparable to that of native LH receptors expressed by KGN cells. This suggests that CHO cells were not expressing unrealistically high levels of YFP-LHR. Nonetheless, evidence for some energy transfer between LH receptors expressed at physiologically-relevant numbers raises questions about the role of receptor density in receptor-receptor interactions. Figure 6 shows the extent E of spontaneous FRET arising from an increase in molecular density. As shown in Figure 6, the probability of energy transfer for receptors expressed at a uniform surface density of 20 receptors μm^{-2} and a Förster critical distance (r_0) of 4.5 nm is less than 1%. The likelihood of receptor interactions, simply as a function of receptor density, increases with increased receptor expression. For acceptor molecules confined to a plane and having a surface density σ, the

efficiency of transfer for given value of r_0 is shown to be $1-\exp[-(2\pi^2/3\sqrt{3})\sigma r_0^2]$ (see Supplemental Material).

From estimates of spontaneous FRET shown in Figure 6, it seems likely those CHO cells stably expressing LHR-GFP with receptor densities that are 2-3 fold greater than the average number of receptors/cell may contribute the FRET efficiencies observed for untreated cells in this study. Substantial FRET will be observed even for homogeneously-distributed molecules if expressed at higher, but commonly encountered, levels. For instance, ErbB1 expressed at levels of 50,000-200,000 receptors per cell is monomeric. At receptor numbers greater than 500,000, approximately 30% of these receptors are in pre-formed dimers (58). Moreover, lateral compartmentalization can only increase the likelihood of apparent FRET. If an acceptor molecule with r_0 of 5 nm in a hetero-FRET pair or a donor molecule in homo-FRET is expressed at an *average* density of 500 μm^{-2} but is confined in lateral compartments occupying 10% of the cell- surface, then an apparent FRET efficiency of 50% would arise *solely* from molecular crowding.

Nonetheless, these FRET results agree with previous studies showing increased interactions between LH receptors following hCG treatment. These studies have measured FRET between FITC- and TrITC-derivatized hormones or between LH receptors tagged with either visible fluorescent protein (VFP) donor or acceptor. VFP-tagged wild type rat LH receptors occupied by either LH or hCG had FRET efficiencies of 13-17%. More importantly, most LH receptors interacted only after binding ligand (44) and only functional ligand-receptor complexes or constitutively active LH receptors showed evidence of such interactions (16). In the absence of ligand, values for energy transfer efficiency between stably expressed, VFP-tagged hLHR-wt receptors on individual cells were typically less than 1% while constitutively active receptors also appeared to be constitutively self-associated with values for energy transfer efficiency greater than 10% (16). These various FRET results agree with electron microscopy studies of rat granulosa cells performed by Luborsky and coworkers (59) where only hormone-treated cells

showed evidence of receptor-receptor interactions and with immunofluorescence studies of the LH receptor on rat granulosa cells where large, punctate structures formed on the cell membrane following treatment with hCG (60).

Methodological differences may account, however, for a report by Tao et al. (61) suggesting that LH receptors may self-associate in the endoplasmic reticulum and remain constitutively associated when expressed at the plasma membrane. These studies were performed using immunoprecipitation of receptors following cell solubilization, an approach that has significant drawbacks (62), as well as by bioluminescence resonance energy transfer, $BRET^1$ and $BRET^2$, techniques. Similarly, Urizar et al. (63) have suggested that LH receptors are constitutively self-associated as has Guan et al. (64). As with co-immunoprecipitation studies of the LH receptor, BRET studies examine receptor interactions on large numbers of cells that are transiently transfected and can, under conditions where expression levels are high, lead to random receptor interactions (65) and non-physiological receptor aggregation simply due to molecular crowding (62).

In addition, the number of molecules expressed in individual cells following transient transfection may exhibit larger cell to cell variation than, for example, CHO cells stably expressing YFP-LHR. As an example, flow cytometric analysis of cells transfected with a membrane-targeted form of GFP show that about 17% of cells express detectable levels of GFP (66) and, when cells do express GFP, the amount per cell can vary over 100-fold. In a BRET experiment, signal comes from cells that express the donor/acceptor pair and, amongst this group of cells, a disproportionally high signal will arise from cells that highly express the BRET pair. Although reducing the amount of DNA used to transfect cells reduces protein expression and the average level of fluorescence within a cell population, this would not alter cell-to-cell differences in the number of expressed molecules or the disproportionate contribution to BRET signal by cells that over-express the proteins in question. The use of BRET pairs may also magnify this effect. The r_0 for the BRET pair used in $BRET^2$ experiments is 7.5 nm, the largest value reported

for a resonance energy transfer pair used in biological studies (67), and, as shown in Figure 1.6, the effect of protein density on FRET efficiency is greater for energy transfer pairs with larger r_0.

Finally, ligand-induced receptor conformational changes may increase the likelihood of receptor interactions with the membrane cytoskeleton. Given the dynamic nature of the cytoskeleton, such molecular complexes can be expected to generate apparent compartmentalization of receptor motions over a range of times and distances. Presumably, hCG-induced formation of larger complexes of LH receptors, signaling molecules or other cytoplasmic proteins enhances interaction with elements of the cytoskeleton and reduces the apparent size of the compartments confining the receptors. Nonetheless, understanding the relationship between receptor-mediated signaling and LH receptor palmitoylation, aggregation and confinement in membrane rafts or larger membrane compartments will require more detailed examination of confined receptors and local signaling events, a process that will likely involve microscopic resolution of membrane microdomains and single molecule detection methods for identifying locally high concentrations of second messengers such as cAMP.

ACKNOWLEDGEMENTS

We would like to thank Dr. Ying Lei and Dr. Steven M. L. Smith for their contributions to this work and for their valuable discussions. We would also like to thank Dr. James Dias (Wadsworth Center, New York State Department of Health, Albany, NY) for providing the KGN human granulosa-like tumor cell line originally developed by Dr. Yoshihiro Nishi and Dr. Toshihiko Yanase at Kyusyu University and Dr. George Bousfield (Wichita State University, Wichita, KS) for providing us with deglycosylated hCG. This work was supported, in part, by NIH grant HD41980 (D.A.R.), the U.S.D.A. Animal Health and Disease Program at Colorado State University (D.A.R.) and NSF grants MCB-1024669 (B.G.B.) and CHE-0628260.

REFERENCES

1. Roess, D. A., Mock, E., Niswender, G. D., and Barisas, B. G. (1988) *Endocrinology* **122**, 261-269

2. Roess, D. A., Jewell, M. A., Philpott, C. J., and Barisas, B. G. (1997) *Biochim Biophys Acta* **1357**, 98-106

3. Roess, D. A., and Smith, S. M. L. (2003) *Biol Reprod* **69**, 1765-1770

4. Roess, D. A., Horvat, R. D., Munnelly, H., and Barisas, B. G. (2000) *Endocrinology* **141**, 4518-4523

5. Luborsky, J. L., and Behrman, H. R. (1979) *Molecular and Cellular Endocrinology* **15**, 61-78

6. Murase, K., Fujiwara, T., Umemura, Y., Suzuki, K., Iino, R., Yamashita, H., Saito, M., Murakoshi, H., Ritchie, K., and Kusumi, A. (2004) *Biophys J* **86**, 4075-4093

7. Smith, S. M., Lei, Y., Liu, J., Cahill, M. E., Hagen, G. M., Barisas, B. G., and Roess, D. A. (2006) *Endocrinology* **147**, 1789-1795.

8. Sako, Y., and Kusumi, A. (1994) *J Cell Biol.* **125**, 1251-1264

9. Daumas, F., Destainville, N., Millot, C., Lopez, A., Dean, D., and Salomé, L. (2003) *Biophys J* **84**, 356-366

10. Sairam, M. R., and Manjunath, P. (1983) *J Biol Chem* **258**, 445-449

11. Dunkel, L., Jia, X. C., Nishimori, K., Boime, I., and Hsueh, A. J. (1993) *Endocrinology* **132** , 763-769

12. Lei, Y., Hagen, G., Smith, S., Barisas, B. G., and Roess, D. (2005) *Biochem Biophys Res Commun* **337**, 430-434

13. Nishi, Y., Yanase, T., Mu, Y.-M., Oba, K., Ichino, I., Saito, M., Nomura, M., Mukasa, C., Okabe, T., Goto, K., Takayanagi, R., Kashimura, Y., Haji, M., and Nawata, H. (2001) *Endocrinology* **142**, 437-445

14. Bowen, R., Verdile, G., Liu, T., Parlow, A., Perry, G., Smith, M., Martins, R., and Atwood, C. (2004) *J Biol Chem* **279**, 20539-20545

15. Edge, A. S. B., Faltynek, C. R., Hof, L., Reichert, L. E., and Weber, P. (1981) *Analytical Biochem* **118**, 131-137

16. Lei, Y., Hagen, G., Smith, S., Liu, J., Barisas, B. G., and Roess, D. (2007) *Mol Cell Endo* **260-262**, 65-72

17. Dietrich, C., Yang, B., Fujiwara, T., Kusumi, A., and Jacobson, K. (2002) *Biophys J* **82**, 274-284

18. Zeng, H., Phang, T., Song, Y. S., Ji, I., and Ji, T. H. (2001) *J Biol Chem* **276** (5), 3451-3458

19. Barisas, B. G., Smith, S. M., Liu, J., Song, J., Hagen, G. M., Pecht, I., and Roess, D. A. (2007) *Biophys Chem* **126**(1-3), 209-217

20. Bader, A. N., Hoetzl, S., Hofman, E. G., Voortman, J., van Bergen en Henegouwen, P. M. P., van Meer, G., and Gerritsen, H. C. (2011) *ChemPhysChem* **12**, 475–483

21. Lidke, D., Nagy, P., Barisas, B., Heintzmann, R., Post, J., Lidke, K., Clayton, A., Arndt-Jovin, D., and Jovin, T. (2003) *Biochem Soc Trans* **31**, 1020-1027

22. Varma, R., and Mayor, S. (1998) *Nature* **394**(20), 798-801

23. Fogarty, K., McPhee, J., Scott, E., and Van Orden, A. (2009) *Anal. Chem.* **81:**, 465-472

24. Ries, J., and Schwille, P. (2008) *Phys Chem* **10**(24), 3487-3497

25. Chiantia, S., Ries, J., and Schwille, P. (2009) *Biochim Biophys Acta* **1788**, 225-233

26. Ruan, Q., Chen, Y., Gratton, E., Glaser, M., and Mantulin, W. W. (2002) *Biophys J* **83**(6), 3177-3187

27. Chen, Y., Munteanu, A. C., Huang, Y.-F., Phillips, J., Zhu, Z., Mavros, M., and Tan, W. (2009) *Chemistry - A European Journal* **15**(21), 5327-5336

28. Schwille, P., Haupts, U., Maiti, S., and Webb, W. W. (1999) *Biophys J* **77**, 2251–2265

29. Jung, J., and A, V. O. (2006) *J. Am.Chem. Soc.* **128**, 1240-1249

30. Jung, J., Ihly, R., Scott, E., Yu, M., and Van Orden, A. (2008) *J. Phys Chem* **112**, 127-133

31. Perroud, T., Huang, B., Wallace, M. I., and Zare, R. (2003) *Chem Phys Chem* **4**, 1121-1123

32. Kawate, N., and Menon, K. M. J. (1994) *J Biol Chem* **269**(48), 30651-30658

33. Kawate, N., Peegel, H., and Menon, K. (1997) *Mol Cell Endo* **127**, 211-219

34. Casella, J. F., Flanagan, M. D., and Lin, S. (1981) Nature **293**(5830), 302-305

35. Flanagan, M. D., and Lin, S. (1980) *J Biol Chem* **255** (3), 835-838

36. Sampath, P., and Pollard, T. D. (1991) *Biochemistry* **30**(7), 1973-1980

37. Schulze, C., Müller, K., Käs, J. A., and Gerdelmann, J. C. (2009) *Cell Motility and the Cytoskeleton* **66**(4), 193-201

38. Ritchie, K., Iino, R., Fujiwara, T., Murase, K., and Kusumi, A. (2003) *Molecular Membrane Biology* **20**, 13-18

39. Ganguly, S., Clayton, A. H. A., and Chattopadhyay, A. (2011) *Biophys J* **100**(2), 361-368

40. Rao, M., and Mayor, S. (2005) *Biochim Biophys Acta* **1746**, 221-233

41. Chen, Y., Muller, J., So, P., and Gratton, E. (1999) *Biophys J* **77**, 553-567

42. Puett, D., Bhowmick, N., Fernandez, L. M., Huang, J., Wu, C., and Narayan, P. (1996) *Molecular and Cellular Endocrinology* **125**(1-2), 55-64

43. Coorssen, J., Schmitt, H., and Almers, W. (1996) *EMBO J* **15**, 3787-3791

44. Horvat, R. D., Barisas, B. G., and Roess, D. A. (2001) *Mol Endo* **15**(4), 534-542

45. Niswender, G. D., Roess, D. A., Sawyer, H. R., Silvia, W. J., and Barisas, B. G. (1985) *Endocrinology* **116**(1), 164-169

46. Horvat, R. D., Nelson, S., Clay, C. M., Barisas, B. G., and Roess, D. A. (1999) *Biochem. Biophys. Res. Comm.* **255**, 382-385

47. Dragsten, P., Henkart, P., Blumenthal, R., Weinstein, J., and Schlessinger, J. (1979) *Proceedings of the National Academy of Science (USA)* **76**(10), 5163-5167

48. Day, C., and Kenworthy, A. (2009) *Biochim Biophys Acta* **1788**, 245-253

49. Brameshuber, M., Weghuber, J., Ruprecht, V., Gombos, I., Horváth, I., Vigh, L., Eckerstorfer, P., Kiss, E., Stockinger, H., and Schutz, G. (2010) *J Biol Chem* **285**(53), 41765-41771

50. Kusumi, A., Shirai, Y. M., Koyama-Honda, I., Suzuki, K. G. N., and Fujiwara, T. K. (2010) *FEBS Letters; Frontiers in Membrane Biochemistry* **584**(9), 1814-1823

51. Jin, H., Zastawny, R., George, S., and O'Dowd, B. (1997) *Eur J Pharmacol* **324**, 109-116

52. Ponimaskin, E., Heine, M., Joubert, L., Sebben, M., Bickmeyer, U., Richter, D., and Dumuis, A. (2002) J Biol Chem **277**, 2534-2546

53. Barron, A. M., Verdile, G., Taddei, K., Bates, K. A., and Martins, R. N. (2010) *Endocrinology* **151**(11), 5380-5388

54. Roess, D. A., Brady, C. J., and Barisas, B. G. (2000) *Biochim Biophys Acta* **1464**(2), 242-250.

55. Roess, D. A., Rahman, N. A., Kenny, N., and Barisas, B. G. (1992) *Biochimica et Biophysica Acta* **1137**, 309-31656. Ji, I., Lee, C., Song, Y., Conn, P., and Ji, T. (2002) *Mol Endo* **16**(6), 1299-1308

57. Hunzicker-Dunn, M., Barisas, G., Song, J., and Roess, D. A. (2003) *J Biol Chem* **278**(44), 42744-42749

58. Nagy, P., Claus, J., Jovin, T. M., and Arndt-Jovin, D. J. (2010) *P roc Nat Acad Sci (USA)* **107** (38), 16524-16529

59. Luborsky, J. L., Slater, W. T., and Behrman, H. R. (1984) *Endocrinology* **115**(6), 2217-2226

60. Amsterdam, A., Berkowitz, A., Nimrod, A., and Kohen, F. (1980) *Proc Nat Acad Sci (USA)* **77**, 3440-3445

61. Tao, Y.-X., Johnson, N. B., and Segaloff, D. L. (2004) *J Biol Chem* **279**, 5904-5914

62. Szidonya, L., Cserzo, M., and Hunyada, L. (2008) *J Endocrinology* **196**, 435-453

63. Urizar, E., Montanelli, L., Loy, T., Bonomi, M., Swillens, S., Gales, C., Bouvier, M., Smits, G., Vassart, G., and Costagliola, S. (2005) *Embo J* **24**, 1954-1964

64. Guan, R., Feng, X., Wu, X., Zhang, M., Zhang, X., Hebert, T., and Segaloff, D. (2009) *J Biol Chem* **284**, 7483-7494

65. James, J. R., Oliveira, M. I., Carmo, A. M., Iaboni, A., and Davis, S. J. (2006) *Nat Methods* **3**(12), 1001-1006

66. Chu, Y.-W., Wang, R., Schmid, I., and Sakamoto, K. (1999) *Cytometry* **36**, 333-339

67. Dacres, H., Wang, J., Dumancic, M. M., and Trowell, S. C. (2009) *Anal Chem* **82**, 432-435

68. Saxton, M. J. (1997) *Biophys J* **72**, 1744-1753

[1]Abbreviations used in this manuscript; luteinizing hormone (LH), human chorionic gonadatropin (hCG), fluorescence resonance energy transfer (FRET), single particle tracking (SPT), gold nanoparticle-hCG conjugate (Au-hCG), Au-deglycosylated-hCG (Au-DG-hCG), homo-transfer FRET (homoFRET), photon counting histogram (PCH), YFP-coupled human LH receptor (YFP-LHR), fluorescence correlation spectroscopy(FCS), equilibrium dissociation constant (K_D), Dulbecco's modification of Eagle's Medium (DMEM), fetal bovine serum (FBS), Minimun Eagle's Medium, (MEM), Geneticin (G418 sulfate), FLAG-tagged LH receptors (FLAG-LHR), macroscopic diffusion coefficient (D), total intensity (s), fluorescence anisotropy (r), diffusional correlation time (τ_D), effective number of detected particles (N_{eff}), molecular brightness (ε), out-of-focus emission ratio (F), LH receptor point cysteine point mutants (LHR-C621, S622), homoFRET efficiency (E), fluorescein isothiocynate (FITC), tetramethylrhodamine isothiocynate (TRITC), Förster critical distance (r_0), visible fluorescent protein (VFP), bioluminescence resonance energy transfer (BRET).

FIGURE LEGENDS

Figure 1: Compartment sizes (upper panel) and diffusion coefficients (lower panel) for CHO cells expressing FLAG-LHR and for native LH receptors on KGN and M17 cells before and after treatment with 0.1 nM to 100 nM hCG. Data shown are the mean ± S.E.M. where data groups marked a, b, c, d, e and f differ significantly ($p<0.05$).

Figure 2: Distribution of compartment sizes accessed by FLAG-LH receptors stably expressed on CHO cells before (●) and after treatment with 0.1 nM hCG (○), 1.0 nM hCG (▼) or 100 nM hCG (△).

Figure 3: Initial and final anisotropy measured before and after photobleaching of YPF coupled to LHR. Data shown are the mean and S.E.M. of at least 20 measurements on individual cells where data groups marked a,b,c,d,e and f differ significantly ($p<0.01$). The origin of the smaller S.E.M. for the difference (r_{final}-$r_{initial}$) relative to separate values of $r_{initial}$ and r_{final} is explained in the text.

Figure 4: Distribution of stably expressed YFP-LHR surface-densities for 58 individual CHO cells as determined by fluorescence correlation spectroscopy.

Figure 5: Number of hCG molecules bound to LH receptors on KGN cells within the focused laser spot as determined by fluorescence correlation spectroscopy. KGN cells were treated with hCG and sequentially labeled with rabbit anti-hCG IgG, biotinylated anti-rabbit IgG and FITC-avidin as described in Materials and Methods. Each point (●) shown is the mean ± S.D. of measurements from at least 14 individual cells.

Figure 6: Degree of spontaneous homoFRET arising from various molecular surface densities. Values shown are for r_0 of 4.5 nm (◊), 6.0 nm (○) and 7.5 nm (■).

Table 1.1: Effects of hCG treatment on single particle tracking of individual human LH receptors on KGN cells using Au-hCG or Au-DG-hCG probes.[a]

Au probe	Treatment [hCG]	Compartments[b] per trajectory	$D_{0\text{-}1}$[c] ($10^{-11}cm^2sec^{-1}$)	$D = L_r^2/4t$[d] ($10^{-11}cm^2sec^{-1}$)	Time[e] (sec)	Compartment[f] Size (nm)
Au-hCG	None	5 ± 2	2.8 ± 0.3	0.7 ± 0.2	24 ± 21	186 ± 21^1
Au-hCG	0.1	5 ± 2	2.2 ± 0.2	0.5 ± 0.1	24 ± 20	156 ± 17
Au-hCG	1	6 ± 2	2.4 ± 0.2	0.6 ± 0.2	21 ± 17	148 ± 16^2
Au-hCG	100	6 ± 2	2.0 ± 0.2	0.3 ± 0.1	20 ± 13	108 ± 11^2
Au-DG-hCG	None	4 ± 2	2.0 ± 0.2	1.6 ± 0.9	27 ± 26	217 ± 27^1
Au-DG-hCG	100	5 ± 1	2.1 ± 0.2	0.5 ± 0.2	25 ± 18	145 ± 20^2

[a] Each data point shown is the mean ± S.E.M. from measurements on 10-15 individual cells.
[b] The average number of compartments accessed by an individual LH receptor during a 2 min, 3600 frame image sequence.
[c] $D_{0\text{-}1}$: Diffusion coefficient within compartment calculated from the first two points of MSD vs. time plot as described by Daumas et al. (9).
[d] D represents the diffusion coefficient within a compartment as calculated from compartment size (L_r) and particle residence time (t) as $D = L_r^2/4t$ as described by Saxton (68).
[e] Average particle residence time within a compartment.
[f] The average size of an individual compartment was calculated as described by Daumas et al. (9) and Murase et al. (6). Values with subscript 2 differ significantly from values with subscript 1($p<0.05$).

Table 1.2: Effects of hCG treatment on single particle tracking of individual native LH receptors on M17 human neuroblastoma cells using Au-hCG or Au-DG-hCG probes.[a]

Au probe	Treatment [hCG]	Compartments[b] per trajectory	$D_{0\text{-}1}$[c] ($10^{-11}cm^2sec^{-1}$)	$D = L_r^2/4t$[d] ($10^{-11}cm^2sec^{-1}$)	Time[e] (sec)	Compartment[f] Size (nm)
Au-hCG	None	5 ± 1	2.1 ± 0.2	0.9 ± 0.3	25 ± 18	219 ± 22^1
Au-hCG	0.1	4 ± 1	2.1 ± 0.2	0.8 ± 0.3	28 ± 20	195 ± 26^1
Au-hCG	1	4 ± 2	2.3 ± 0.3	0.4 ± 0.1	27 ± 21	143 ± 17^2
Au-hCG	100	5 ± 2	1.9 ± 0.2	0.4 ± 0.1	22 ± 16	131 ± 18^2

[a] Each data point shown is the mean ± S.E.M. from measurements on 10-15 individual cells.
[b] The average number of compartments accessed by an individual LH receptor during a 2 min, 3600 frame image sequence.
[c] $D_{0\text{-}1}$: Diffusion coefficient within compartment calculated from the first two points of MSD vs. time plot as described by Daumas et al. (9).
[d] D represents the diffusion coefficient within a compartment as calculated from compartment size (L_r) and particle residence time (t) as $D = L_r^2/4t$ as described by Saxton (68).
[e] Average particle residence time within a compartment.
[f] The average size of an individual compartment was calculated as described by Daumas et al. (9) and Murase et al. (6). Values with subscript 2 differ significantly from values with subscript 1($p<0.05$).

Table 1.3: Effects of cytochalasin D treatment on single particle tracking of individual human FLAG-tagged LHR-C621, 622S and FLAG-LHR on CHO cells using an Au-anti-FLAG probe.

Cell Line	Treatments [hCG]	Compartments[(a)] per trajectory	$D_{0\text{-}1}$[(b)] ($10^{-11}cm^2sec^{-1}$)	$D = L_r^2/4t$[(c)] ($10^{-11}cm^2sec^{-1}$)	Time[(d)] (sec)	Compartment[(e)] Size (nm)
CHO FLAG-LHR	None Cytochalasin D	2 ± 1	3.6 ± 0.9	2.8 ± 0.5^1	25 ± 18	221 ± 80^1
CHO FLAG-LHR	100 nM hCG Cytochalasin D	2 ± 1	2.8 ± 0.4	2.2 ± 0.4^1	29 ± 14	204 ± 66^1
CHO FLAG-LHR 621,622S	None	3 ± 1	1.1 ± 0.1	0.4 ± 0.2^2	29 ± 12	204 ± 74^1
CHO FLAG-LHR 621,622S	100 nM hCG	3 ± 1	1.0 ± 0.2	0.1 ± 0.1^2	32 ± 1	195 ± 47^1

[(a)] Each data point shown is the mean ± S.E.M. from measurements on 10-20 individual cells.
[(b)] The average number of compartments accessed by an individual LH receptor during a 2 min, 3600 frame image sequence.
[(c)] $D_{0\text{-}1}$: Diffusion coefficient within compartment calculated from the first two points of MSD vs. time plot as described by Daumas et al. (9).
[(d)] D represents the diffusion coefficient within a compartment as calculated from compartment size (L_r) and particle residence time (t) as $D = L_r^2/4t$ as described by Saxton (68).
[(e)] Average particle residence time within a compartment.
[(f)] The average size of an individual compartment was calculated as described by Daumas et al. (9) and Murase et al. (6). Values with subscript 2 differ significantly from values with subscript 1($p<0.05$).

Table 1.4: Effects of hCG treatment on efficiency of homoFRET between YFP-LHR on CHO cells.[a]

Treatment [hCG]	$r_{initial}$	r_{final}	E (%)[b]
None	0.18 ± 0.02	0.21 ± 0.03	10%
0.1 nM	0.15 ± 0.01	0.19 ± 0.04	20%
1.0 nM	0.17 ± 0.05	0.23 ± 0.05	26%
100 nM	0.17 ± 0.04	0.26 ± 0.06	34%

[a] Data points shown are the mean ± S.D.
[b] FRET efficiencies (E) were estimated from average initial and final anisotropy values shown in Figure 3 as $\%E = (1- r_{initial}/r_{final}) \times 100$.

Table 1.5: Effects of hCG treatment on PCH analysis of YFP-LHR on CHO cells.

hCG (nM)	N_{eff}[a]	ε (kHz)[b]
None	12.5±2.6	0.07±0.01
1	13.6±3.3	0.10±0.03
10	13.4±5.6	0.13±0.03[c]
100	15.2±4.2	0.13±0.02[c]
1000	15.3±3.4	0.14±0.04[c]

[a] Each data point shown is the mean ± SEM of measurements on at least 6 individual cells.
[b] Estimates of ε were obtained using a detector bin time of 9 μs and *F* values from 0.5-0.7. Data points shown are the mean ± SD.
[c] Values were statistically different from cells not treated with hCG using students t-test ($p<0.02$).

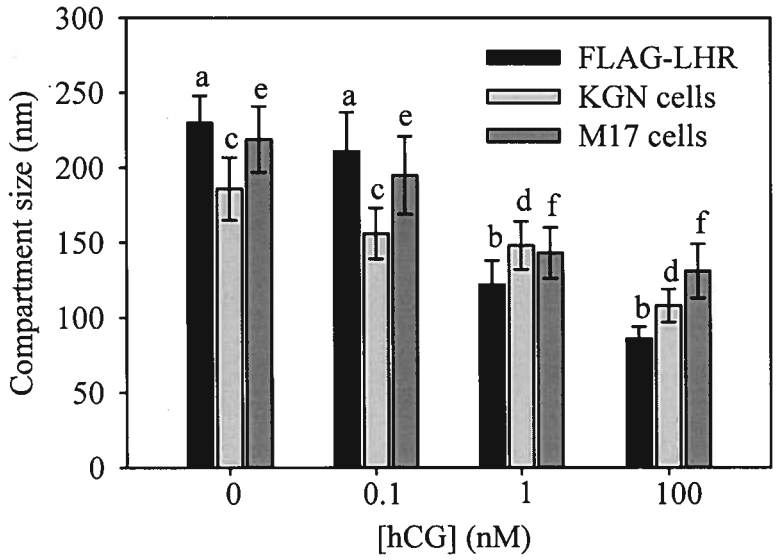
Compartment size (nm)
300
250
200
150
100
50
0
FLAG-LHR
KGN cells
M17 cells
a
c
e
a
c
e
b
d
f
b
d
f
0
0.1
1
100
[hCG] (nM)

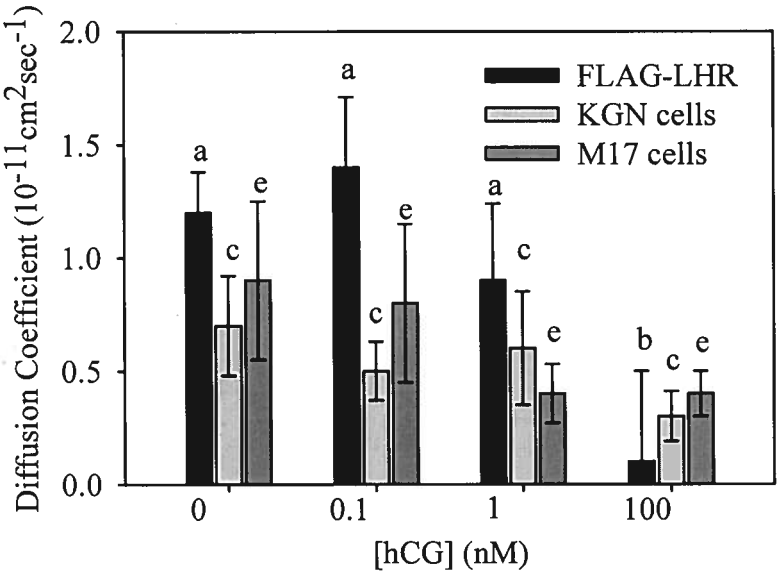
Diffusion Coefficient ($10^{-11}cm^2sec^{-1}$)
2.0
1.5
1.0
0.5
0.0
FLAG-LHR
KGN cells
M17 cells
a
c
e
a
c
e
a
c
e
b
c
e
0
0.1
1
100
[hCG] (nM)

Figure 1.1

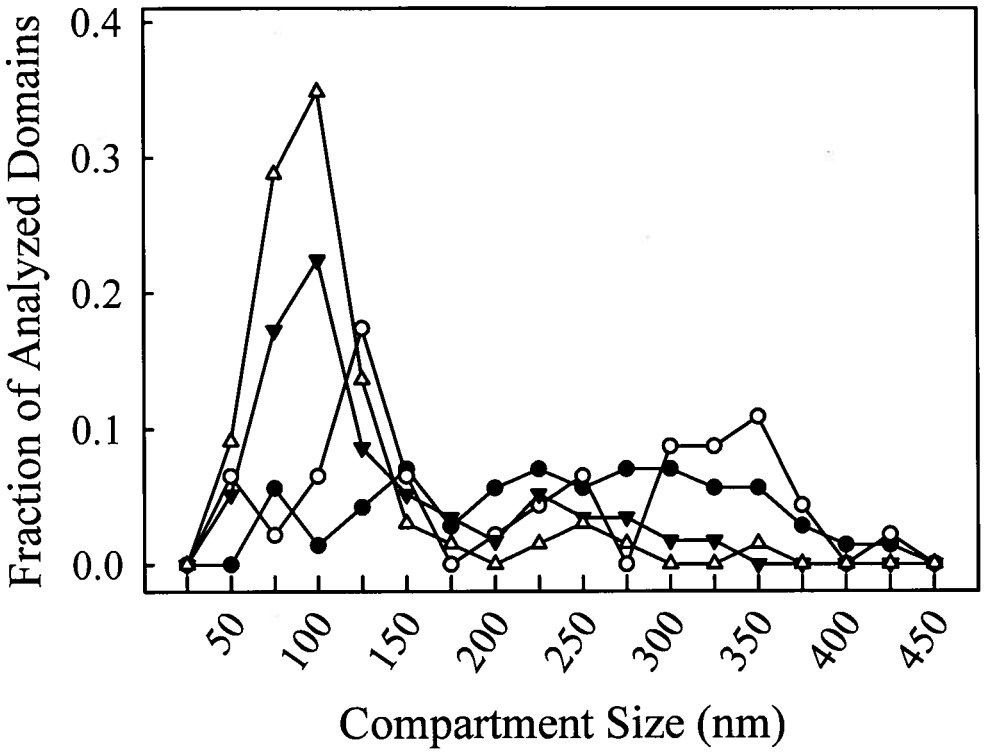
Fraction of Analyzed Domains
0.4
0.3
0.2
0.1
0.0
50
100
150
200
250
300
350
400
450
Compartment Size (nm)

Figure 1.2

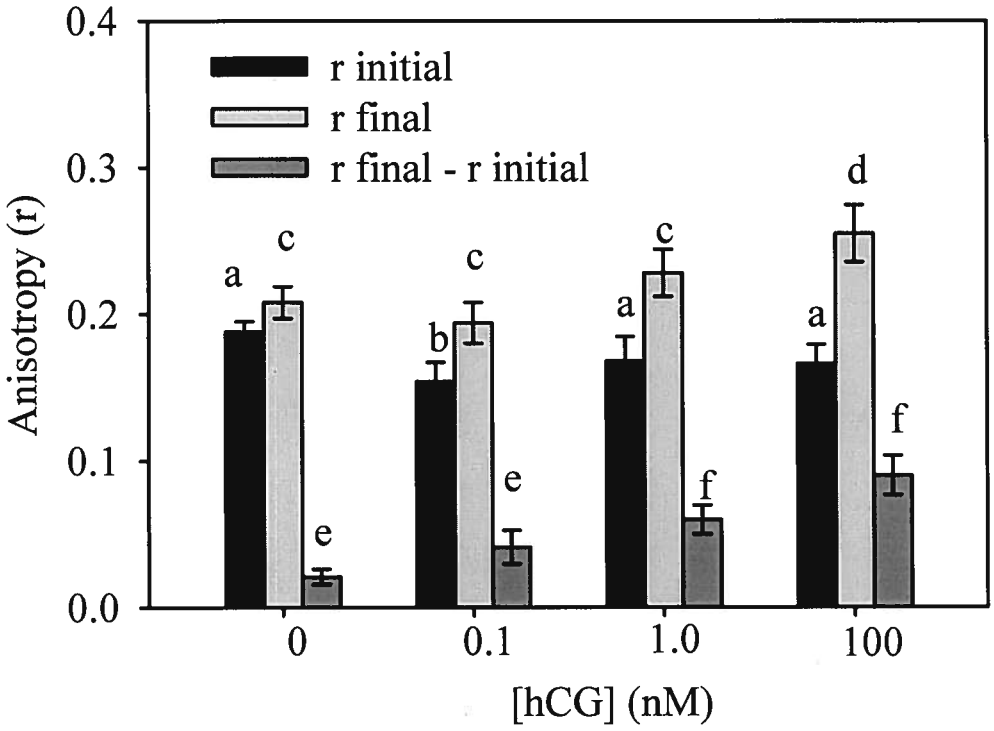
0.4
0.3
0.2
0.1
0.0
Anisotropy (r)
r initial
r final
r final - r initial
a
c
e
b
c
e
a
c
f
a
d
f
0
0.1
1.0
100
[hCG] (nM)

Figure 1.3

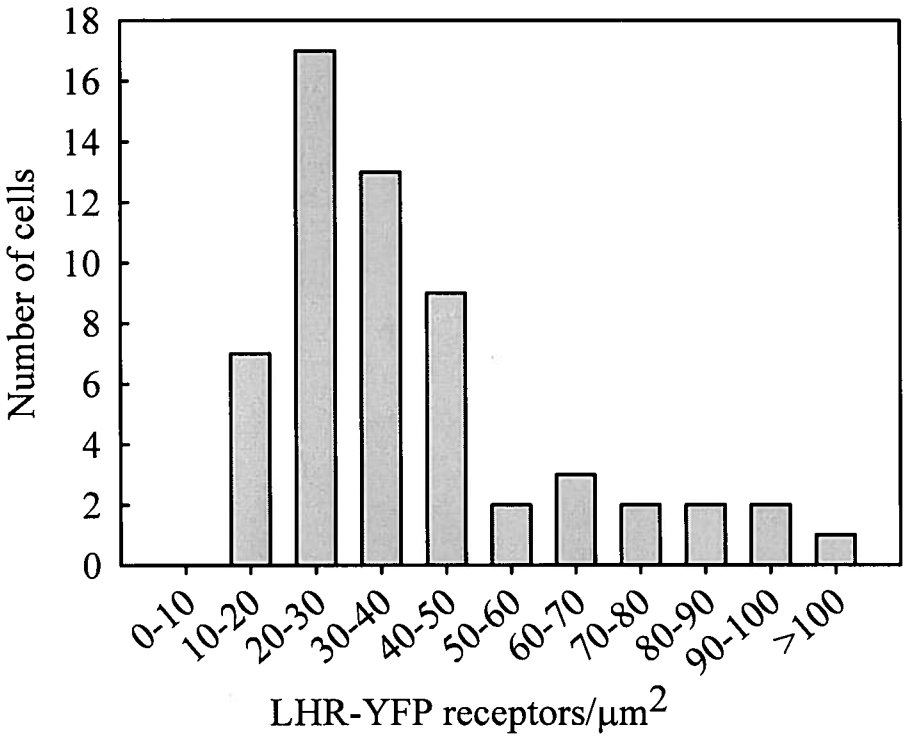
18
16
14
12
10
8
6
4
2
0
Number of cells
0-10
10-20
20-30
30-40
40-50
50-60
60-70
70-80
80-90
90-100
>100
LHR-YFP receptors/μm2

Figure 1.4

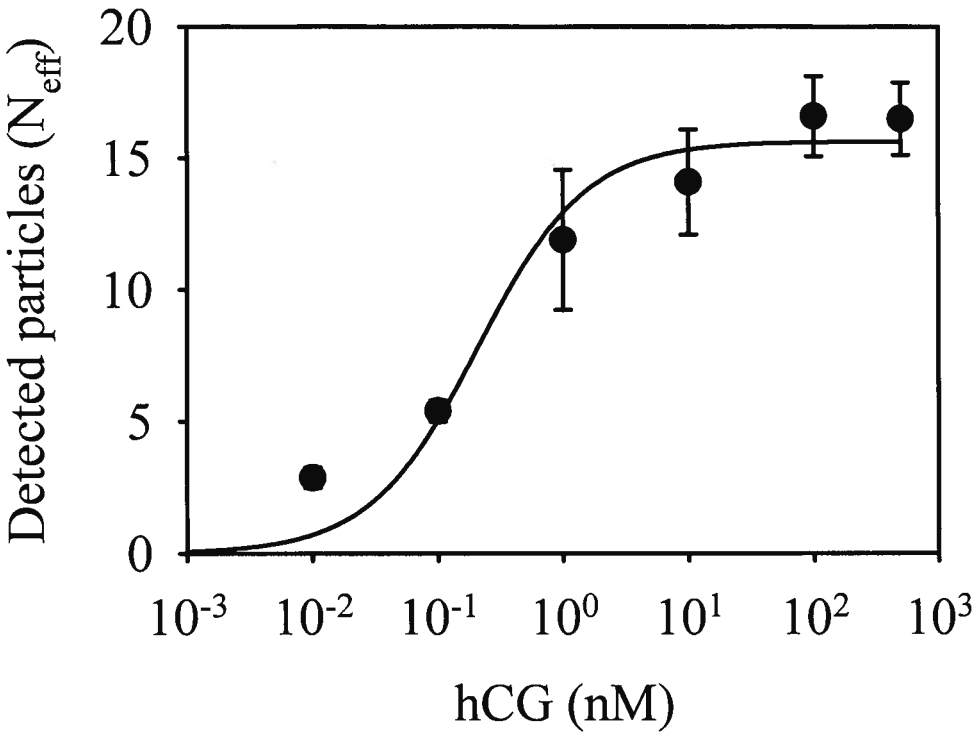
Detected particles (N_{eff})
20
15
10
5
0
10^{-3}
10^{-2}
10^{-1}
10^{0}
10^{1}
10^{2}
10^{3}
hCG (nM)

Figure 1.5

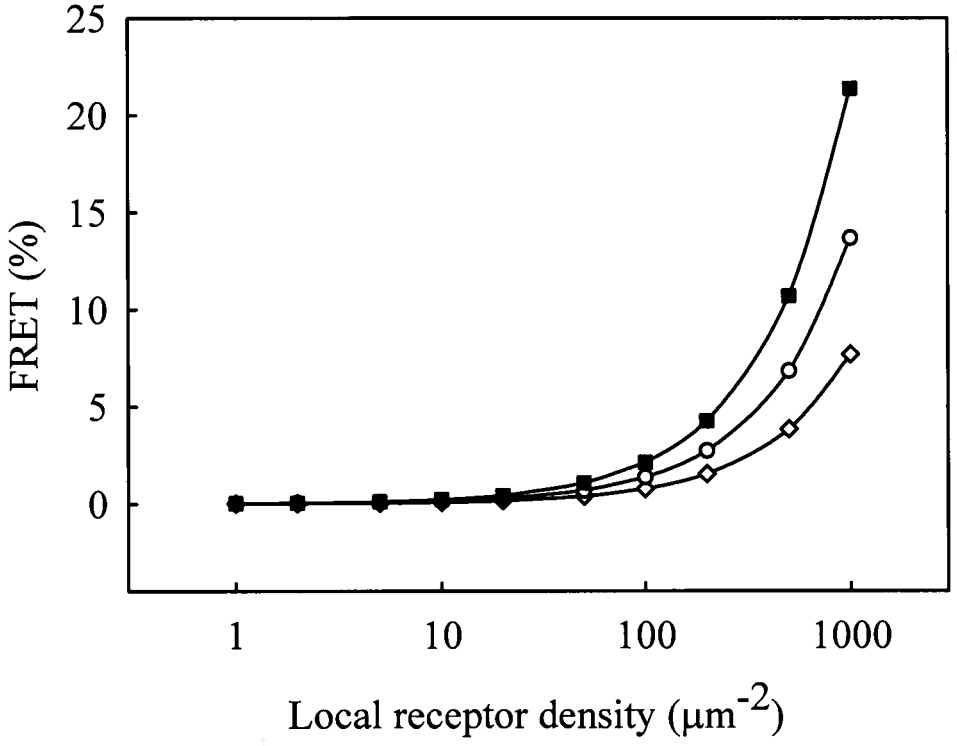

Figure 1.6

CHAPTER II: Peter W. Winter performed all of experiments described herein.

CHARACTERIZING INSULIN AND IGF-1 BINDING TO LIVE CELLS BY FLUORESCENCE CORRELATION SPECTROSCOPY

Peter W. Winter[a], Jeffrey T. McPhee[b], Alan K. Van Orden[b], Deborah A. Roess[a,c] and B. George Barisas[a,b].

[a]Cell and Molecular Biology Program, [b]Department of Chemistry, [c]Department of Biomedical Sciences

Colorado State University, Fort Collins, Colorado 80523,

Address all correspondence and requests for reprints to: Dr. B. George Barisas, Department of Chemistry, Campus Mail 1872, Colorado State University, Fort Collins, CO 80523. Phone: (970) 491-6641 Fax: (970) 491-1801 Email: barisas@lamar.colostate.edu

We used fluorescence correlation spectroscopy to examine the binding of insulin, insulin-like growth factor type-1 (IGF1) and anti-receptor antibodies to insulin receptors (IR) and insulin-like growth factor one receptors (IGF1R) on individual 2H3 rat basophilic leukemia cells. Experiments revealed two distinct classes of insulin binding sites, 15,000 high-affinity and 39,000 low-affinity sites with K_D of 0.11 nM and 75 nM, respectively. IGF1 competes with insulin for 21,000 low-affinity sites with K_D of 0.14 nM and with high-affinity sites with K_D of 10 nM. Dissociation rate constants of insulin and IGF1 were determined to be 0.015 min^{-1} and 0.013 min^{-1}, respectively, allowing estimation of ligand association rates. Combined, our results suggest that, in addition to IR and IGF1R homodimers, substantial numbers of hybrid IR-IGF1R heterodimers are present on the surface of these cells and that significant fractions of insulin and IGF1 binding to these cells involves non-cognate receptors and IR-IGF1R hybrids.

KEYWORDS

Fluorescence Correlation Spectroscopy; Insulin; IGF1; Receptor Surface Density; Ligand Binding Kinetics

HIGHLIGHTS

- FCS permits examination of dynamic interactions between biologically relevant molecules on individual live cells.
- 2H3-RBL cells express substantial levels of IR and IGF1R homodimers, as well as, hybrid IR-IGF1R heterodimers.
- Insulin and IGF1 compete with differing affinities for available binding sites on these cells.
- These results support random-association of IR and IGF1R monomers in the endoplasmic reticulum.

1. INTRODUCTION

Traditional approaches for the examination of cell surface receptor density and ligand binding often rely on radio-labeled ligands or fluorescence intensity measurements on bulk solutions [1, 2]. Unfortunately, these methods suffer from inherent drawbacks such as the need for large numbers of cells and, in cases where receptor numbers are very low, can fail to detect specific binding. In contrast, fluorescence correlation spectroscopy (FCS) is a versatile technique capable of examining interactions between small numbers of biological molecules under physiological conditions [3, 4]. Initially introduced in the 1970's [5-7], FCS has since become a versatile tool for the characterization of dynamic biological processes [8, 9]. FCS extracts information from the fluctuations in fluorescence intensity that occur as molecules move into and out of a femtoliter-size observation volume [10]. This optically-defined interrogation volume, coupled with high photon sensitivity, permits the examination of as few as 1-2 fluorescing molecules at specific points of interest on the cell membrane or within the cell interior [11, 12], allowing real-time measurement of interactions between receptors and ligands [13]. Variations of FCS have recently been used in live cells to examine epidermal growth factor receptor clustering [14], the kinetics of RhoGTPase-Cdc42 effector complex dissociation [15] and interactions between Src peptides and DNA [16]. Ease of use with live cells, the ability to monitor molecular dynamics across a broad timescale and the relatively short time needed for data acquisition make FCS particularly well suited for the examination of molecular interactions at the single molecule level.

We report here the use of FCS to determine the surface densities and ligand binding thermodynamics and kinetics of insulin receptors (IR) and insulin-like growth factor 1 receptors (IGF1R) on live 2H3 rat basophilic leukemia (2H3-RBL) cells. IR and IGF1R are two structurally similar tyrosine kinase receptors with differential effects on cell growth and energy metabolism [17-19]. Because of their physiological importance [20], considerable work has

focused on understanding the subtle differences between the two receptors, their ligands and signaling networks [21]. In solution, each receptor is capable of binding both insulin and IGF1 with nM affinity [20, 22, 23]. Also, due to random receptor-dimer assembly in the endoplasmic reticulum, a significant fraction of native receptors in some cell types appear to be IR-IGF1R hybrids [24-27], further complicating the analysis of insulin and IGF1 binding kinetics. However, despite considerable literature describing IR, IGF1R and IR-IGF1R hybrid signaling *in vitro*, details of insulin and IGF1 binding to receptors in live cells at the single-molecule level remain elusive.

Our results demonstrate that 2H3-RBL cells express detectable levels of both IR and IGF1R. We also show that insulin and IGF1 each bind to two distinct classes of sites on these cells and that both insulin and IGF1 compete with differing affinities for these binding sites. Finally, we demonstrate that dissociation of FITC-insulin from receptors is sensitive to the concentration of excess insulin available in solution, but is not sensitive to the initial FITC-insulin labeling concentration. Taken together, our results suggest that, in addition to IR and IGF1R homodimers, hybrid IR-IGF1R heterodimers are present on the surface of 2H3-RBL cells and that a significant portion of insulin and IGF1 binding to these cells involves non-cognate receptors and IR-IGF1R hybrids.

2. EXPERIMENTAL PROCEDURES

2.1 Materials

2H3-RBL cells were purchased from ATCC (Manassas, VA). Human-recombinant-insulin monovalently-labeled at the *N*-terminus with fluorescein isothiocynate (FITC-insulin) and human-recombinant-IGF1 were purchased from Invitrogen (Carlsbad, CA). Insulin, bovine serum albumin (BSA), anti-rabbit biotin secondary antibody and FITC-avidin were purchased from Sigma (St. Louis, MO). Anti-IRα, anti-IRβ and anti-IGF1Rα antibodies were purchased

from Santa Cruz Biotech (Santa Cruz, CA). Anti-Type I IgE receptor (FcεRI) antibody, FcεRIα was purchased from Upstate Cell Signaling Solutions (Billerica, MA). Rhodamine 6G (R6G) was purchased from Allied Chemical (Vadodara, Gujarat, India). Minimal essential medium (MEM) was purchased from Cellgro (Manassas, VA). Fetal bovine serum (FBS), penicillin G, streptomycin and Fungizone were purchased from Gemini (Sacramento, CA).

2.2 Preparation of cell samples

2H3-RBL cells were maintained in plastic tissue culture dishes in MEM supplemented with 10% FBS, 200 mM L-glutamine, 10,000 U/mL penicillin G, 10 µg/mL streptomycin and 25 µg/mL fungizone. 24-36 hr before experiments cells were seeded onto sterile #1.5 glass-bottom culture dishes, grown to approximately 50% confluence and, unless otherwise indicated, incubated in medium without FBS for at least 12 hr before use. All cell labeling protocols were performed in phosphate-buffered saline pH 7.4 (PBS) containing 0.1% BSA (PBS-BSA), except as indicated. All washes were in 1mL of PBS-BSA buffer for 30 sec. Before use, all antibodies, peptides and fluorescent probes were spun for 10 min at maximum speed in a tabletop microcentrifuge to remove aggregates. Cell samples were immersed in 400 µL of buffer during FCS data acquisition, except as noted. To reduce the effects of endocytosis on receptor internalization, all cell labeling and data acquisition were conducted at room temperature.

2.3 Antibody labeling of receptors

To label FcεRI, cells were incubated for 30 min with rabbit-derived primary antibody and washed 4 times. Cells were then incubated for 15 min in 500 nM anti-rabbit biotin secondary antibody again followed by 4 washes. Finally, cells were incubated in 250 nM FITC-avidin for 15 min, followed by 4 washes. To label the insulin receptor α-subunit (IRα), cells were serum starved or treated with 10 µM insulin for 1 hr or 10% FBS in MEM for 1 hr and then incubated

for 30 min with rabbit-derived primary antibody and washed 4 times. Cells were then incubated for 15 min in 500 nM biotin conjugated anti-rabbit secondary antibody again followed by 4 washes. Finally, cells were incubated in 250 nM FITC-avidin for 15 min, followed by 4 washes. To label the insulin receptor β-subunit (IRβ), cells were incubated for 30 min with biotin-conjugated primary antibody followed by 4 washes and then incubated for 15 min in 250 nM FITC-avidin, followed by 4 washes. To label IGF1R, cells were incubated for 30 min with rabbit-derived primary antibody specific against the α-subunit of IGF1R (IGF1Rα) and washed 4 times. Cells were then incubated for 15 min in 500 nM anti-rabbit biotin secondary antibody again followed by 4 washes. Cells were then incubated in 250 nM FITC-avidin for 15 min, followed by 4 washes.

2.4 Hormone labeling of receptors

In FITC-insulin equilibrium binding experiments, cells were incubated in the indicated concentration of FITC-insulin for 30 min, followed by 4 washes. For insulin and IGF1 competition binding experiments, cells were simultaneously incubated in buffer solutions containing the indicated concentration of FITC-insulin and increasing amounts of either insulin or IGF1for 30 min, and then washed 4 times. In experiments using cells pre-incubated with IGF1, cells were first incubated in the indicated concentration of IGF1 for 30 min and then in a combination of both the indicated amount of IGF1 and 250 nM FITC-insulin for 30 min, followed by 4 washes. To measure FITC-insulin dissociation, cells were labeled with the indicated amount of FITC-insulin for 30 min, washed 4 times and then examined at the times indicated. Alternatively, to investigate the effects of aqueous insulin on FITC-insulin dissociation, cells were labeled with 250 nM FITC-insulin for 30 min, washed 3 times for 30 sec in 1 mL of buffer and then incubated in the indicated concentration of insulin for 30 min and washed 3 times. To measure IGF1 dissociation, cells were labeled with 10 nM IGF1 for 30 min, washed 4 times and

then incubated in buffer for the indicated time. This was followed by labeling with 250 nM FITC-insulin for 30 min and 4 washes.

2.5 FCS instrumentation

FCS experiments were performed using a modified Nikon TE1000 inverted microscope equipped with a 100x, 1.25 NA oil-immersion objective, an Omnichrome Melles-Griot multi-line air-cooled argon ion laser, two Perkin Elmer single photon counting modules (SPCM-AQR-14) and an ALV-6010 digital hardware correlator. This apparatus has been described in detail previously [28]. Based on FCS measurements of aqueous R6G diffusion, the $1/e^2$ radius r_o of the laser excitation beam at the sample in our system was determined to be 241 nm (data not shown). To obtain the greatest signal-to-noise ratio while minimizing the effects of probe photobleaching on receptor density estimates and ligand binding kinetics, the intensity of the laser excitation beam at the sample was attenuated to <100 μW using neutral density filters [29]. The laser excitation beam was focused on the apical cell membrane by adjusting the objective z-position to maximize detector count rates and minimize diffusional correlation times (τ_D) as described by Ries and Schwille [12]. Relevant portions of individual FCS traces were analyzed by weighted least-squares fitting of $g(\tau)$ to equation (3) to obtain estimates of the effective number of particles detected (N) and the diffusional correlation time (τ_D) for both receptor-bound and aqueous particles.

2.6 Analysis of fluorescence intensity fluctuations

All FCS data were analyzed using methods similar to those previously described by Schwille et al. [3], where the normalized fluctuation intensity autocorrelation function is defined as

$$g(\tau) = \langle \delta F(t) \delta F(t+\tau) \rangle / \langle F(t) \rangle^2 \qquad (1)$$

where F(t) is the mean fluorescence intensity fluctuation at time t and

$$\delta F(t) \equiv \mathrm{F}(t) - \langle F(t) \rangle \qquad (2)$$

is the corresponding fluorescence intensity fluctuation about the mean.

Given a Gaussian excitation spot of $1/e^2$ radius r_o and a substance with diffusion constant *D,* the autocorrelation function describing two-dimensional diffusion within the cell membrane is

$$g(\tau) = \frac{1}{N}\left(\frac{1}{1+\tau/\tau_d}\right) \qquad (3)$$

where N is the effective number of correlating particles detected in the illumination zone and

$$\tau_d = \frac{r_0^2}{4D} \qquad (4)$$

is the characteristic time of correlation decay.

2.7 Analysis of ligand- receptor interactions on live cells

Analysis of FCS data showed that the number N of membrane bound particles detected depended on the concentration of receptor-specific fluorophore and competing ligands. To evaluate the specific binding capacity and equilibrium dissociation constant K_D of each fluorophore-conjugated ligand for receptors, data were fit to hyperbolic functions describing either one or two-site sequential binding.

$$N = \frac{cN_1}{K_{D_1} + c} + \frac{cN_2}{K_{D_2} + c} \qquad (5)$$

where N is the number of particles detected, c is the concentration of fluorophore-conjugated receptor-specific probe and N_1, N_2 are the maximum numbers of bound particles detected at saturating concentration of receptor-specific probe, exhibiting dissociation constants K_{D1} and K_{D2}, respectively. For single-site binding, N_2 is fixed at zero.

The density σ of receptors on the surface of live cells was calculated as

$$\sigma = \frac{N_1 + N_2}{\pi {r_o}^2} \quad (6)$$

When analyzing the competitive binding between two ligands, the concentration $[I]_{1/2}$ of the competing ligand which gave 50% inhibition of probe binding was determined using

$$N = N_o + \frac{N_{max} - N_o}{1 + [I]/[I]_{1/2}} \quad (7)$$

where N_{max} and N_o are the numbers of detected particles at the indicated concentration [L] of fluorophore-conjugated ligand as observed at zero and maximum concentrations of competing ligand, respectively.

From $[I]_{1/2}$ the equilibrium dissociation constant K_I can be calculated according to the method of Cheng et Prusoff [30] as

$$K_I = \frac{[I]_{1/2}}{1 + {[L]}/{K_D}} \quad (8)$$

In ligand-dissociation experiments for both FITC-insulin and IGF1, data were fit to a single component exponential decay function

$$N = N_o + (N_{max} - N_o)e^{-tk_{off}} \quad (9)$$

where t is time and k_{off} is the dissociation rate constant.

2.8 Presentation of Results

Each data point shown in figures represents the combined result of FCS measurements from 14-20 individual 2H3-RBL cells. Values presented in figures, text and tables, excluding Figure 4 and Figure 5a, are the arithmetic mean ± SD. To improve visual clarity, Figure 4 and Figure 5a show the mean ± SEM.

3. RESULTS

3.1 Binding of fluorescent probes to live cells

We used FCS to analyze the dynamics of peptide-conjugated fluorescent probes in solution and when bound to receptors on the membranes of live 2H3-RBL cells. τ_D values for these probes in solution correspond to lateral diffusion constants of approximately $5x10^{-7}$ cm^2s^{-1} as is appropriate for small proteins in solution (Figure 2.1). When bound to receptors on live 2H3-RBL cells the fluorescence emission of the FITC-conjugated receptor-specific probes was localized to the cell-surface and detected particles exhibited τ_D that correspond to lateral diffusion constants of between 10^{-9} cm^2s^{-1} and 10^{-10} cm^2s^{-1} as is appropriate for cell-surface receptors (Figure 2.1). Receptors on live cells labeled with either FITC-insulin or a sandwich of IR-specific antibody, biotinylated-secondary antibody and FITC-avidin had similar diffusion times while antibody-labeled Fcε receptors exhibited somewhat slower diffusion. After an initial (~10sec) illumination phase to deplete immobile particles [3, 31], the photon count rates from both avalanche photodiodes during live cell labeling experiments were steady, indicating that there was no appreciable photobleaching of FITC-insulin over the time-scale of these experiments (data not shown).

To test the specificity of our probes, we performed FCS measurements on cells incubated with FITC-avidin while omitting either primary or secondary antibody or both. No appreciable surface-localized fluorescence was observed under these conditions (data not shown).

3.2 Determination of FcεRI, IR and IGF1R cell-surface densities

2H3-RBL cells are known to express both FcεRI [32] and IR [33]. Figure 2.2a shows correlation data obtained from live 2H3-RBL cells labeled with increasing concentrations of primary antibody specific for an external epitope of FcεRI. Non-linear least-squares analysis of these data using a single-site binding model showed that the FcεRI-specific antibody binds to an

estimated 540 receptors μm^{-2} with K_D of 61 nM (Table 2.1). A total of 170,000 FcεRI per cell was calculated from the receptor surface density assuming 2H3-RBL cells each have an average surface area of 314 μm^2 [32]. This is consistent with previous estimates of between 200,000-300,000 receptors per cell for this cell type [32, 34-37].

Two different primary antibodies specific for external epitopes of either IRα or IRβ, respectively, were then used to determine the density of IR on the surface of live 2H3-RBL cells. Measurements made with both primary antibodies resulted in similar estimates of IR surface density (Figure 2.2b and c). Use of the IRα-specific antibody yielded 190 receptors μm^{-2} or 60,000 per cell, while the IRβ-specific antibody yielded 196 receptors μm^{-2} or 62,000 per cell (Table 2.1). However, despite providing similar estimates of IR density, the two IR-specific antibodies exhibited distinct K_D. The IRα-specific antibody appeared to bind receptors with K_D of 23 nM, while the IRβ-specific antibody appeared to bind with K_D of 163 nM (Table 2.1).

We also estimated the density of IGF1R on these cells using an antibody specific for IGF1Rα. This antibody appeared to bind 161 receptors μm^{-2} or 51,000 per cell with a K_D of 2 nM (Figure 2.2d and Table 2.1).

3.3 Equilibrium binding of FITC-insulin to live cells

To evaluate the binding of insulin to IR on live cells, we used a commercially available *N*-terminally labeled FITC-insulin. In contrast to the binding of receptor-specific antibodies, equilibrium binding of FITC-insulin appeared to fit best to a two-site sequential model (Figure 2.3a). Scatchard analysis of FITC-insulin binding also showed a curvilinear 'concave up' pattern indicating two classes of FITC-insulin binding sites (Figure 2.3b). Using least-squares analysis, we determined the K_D of the two classes of FITC-insulin binding sites to be 0.11 nM and 75 nM with surface densities of 49 sites μm^{-2} and 124 sites μm^{-2}, respectively (Table 2.2). The total

number of FITC-insulin binding sites identified in these experiments was approximately 54,000 per cell.

FITC-insulin binding to receptors on 2H3-RBL cells was almost completely blocked by pre-incubating cells in medium containing 10% FBS or 10 μM insulin (Table 2.3), treatments which had no effect on the binding of the IRα antibody (Figure 2.2b). Binding of 250 nM FITC-insulin was also partially blocked by pre-incubation of cells with between 0.1-10 nM IGF1 (Table 2.3). The diminished binding of FITC-insulin to cells that have been pre-incubated with increasing concentrations of IGF1 is assumed to result from occupancy of the FITC-insulin binding sites by IGF1. This suggests that at least 67 ± 28 μm^{-2} of the low affinity FITC-insulin binding sites, approximately 21,000 ± 9,000 per cell, are able to bind IGF1 with K_D of 0.14 ± 0.04 nM (Figure 2.4).

3.4 Insulin and IGF1 competitive binding to live cells

When cells are labeled simultaneously with FITC-insulin and either insulin or IGF1, equilibrium competition for available binding sites is observed (Figure 2.5a and b). In such competition binding experiments using a probe concentration of 0.1 nM FITC-insulin, insulin competed with K_I of 0.09 nM (Table 2.4). However, the apparent K_I of insulin for FITC-insulin binding sites decreased when probed with increasing concentrations of FITC-insulin. Alternatively, IGF1 competed with 0.1 nM FITC-insulin for binding sites with a K_I of 9.4 nM (Table 2.5). Although, similar to insulin, the apparent K_I of IGF1 for FITC-insulin binding sites decreased when probed with increasing concentrations of FITC-insulin.

3.5 Dissociation rates of FITC-insulin and IGF1 from live cells

The dissociation of FITC-insulin from the surface of 2H3-RBL cells in the absence of excess solution phase insulin was monitored by measuring the number of particles remaining

bound to cells every 3 min for 2 hr. Figure 2.6a shows that, when incubated in insulin-free PBS-BSA buffer, cells labeled with FITC-insulin concentrations ranging from 1-100 nM behaved similarly and exhibited k_{off} values between 0.014 min^{-1} and 0.017 min^{-1} (Table 2.6).

However, dissociation of FITC-insulin was sensitive to the concentration of excess insulin available in solution. Cells labeled with 250 nM FITC-insulin were incubated for 30 min in the indicated concentrations of excess insulin, then washed and observed (Figure 2.6b). It appears that the rate of FITC-insulin dissociation increased in the presence of unlabeled insulin at concentrations below 10^{-8} while, at insulin concentrations greater than 10^{-8} M, the rate of FITC-insulin dissociation decreased.

Dissociation of IGF1 was monitored by examining the partial blocking of FITC-insulin binding at various times after pre-incubating cells with IGF1 (Figure 2.6c). Diminished binding of 250 nM FITC-insulin after pre-incubating cells with 10 nM IGF1 is assumed to result from occupancy of FITC-insulin binding sites by IGF1 as was discussed in Section 3.3. Using this method, we estimated that the k_{off} of IGF1 from receptors on live 2H3-RBL cells is 0.013 min^{-1} (Table 2.6).

3.6 *Estimated association rates for insulin and IGF1 binding to live cells*

Our results provide experimentally-determined values for either K_D or K_I , and k_{off} for FITC-insulin or insulin and IGF1 reversibly binding to receptors on 2H3-RBL cells. From these data we estimated the rate of association k_{on} for each ligand binding to both high and low affinity sites. The k_{on} for high and low affinity FITC-insulin binding sites were estimated to be $1.4x10^8$ $M^{-1}min^{-1}$ and $2x10^5$ $M^{-1}min^{-1}$, respectively. Alternatively, the k_{on} of IGF1 to high affinity IGF1 binding sites identified after pre-incubation with IGF1 was estimated to be $7.1x10^9$ $M^{-1}min^{-1}$, while the k_{on} of IGF1 to low-affinity IGF1 binding sites identified in competitive labeling experiments between IGF1 and FITC-insulin was estimated to be $1.4x10^6$ $M^{-1}min^{-1}$.

4. DISCUSSION

The present work emphasizes the utility of FCS for the quantitative examination of membrane receptor ligand binding in living cells at the single molecule level [14, 15, 34]. Localization of fluorophore-conjugated ligand fluorescence to the cell membrane, specificity of ligand binding, and differences in lateral diffusion between solution-phase and membrane localized fluorophore-conjugated ligands allows specific examination of fluorophore-conjugated ligands bound to membrane receptors even in the presence of solution-phase fluorophore-conjugated ligand [3].

In the present study, use of antibodies specific against either α or β subunits of IR led to initial estimates of between 190-196 receptors μm^{-2} or approximately 60,000 receptors per cell. Labeling of receptors with FITC-insulin led to a slightly lower estimate of approximately 54,000 total receptors. This is similar to previous work by Rigler and coworkers who estimated the density of IR on live human renal cells to be approximately 200 μm^{-2} [38]. Estimation of IGF1R numbers using an IGF1Rα specific antibody also identified 161 receptors μm^{-2} or 51,000 per cell. However, FCS measurements enumerate separately diffusing species binding particular fluorescent ligands, hence apparent numbers of IR and IGF1R estimated using anti-IR or anti-IGF1R antibodies, respectively, also include IR/IGF1R hybrids. Thus, it is likely that neither IR nor IGF1R density are actually this high [27]. We also suggest that similar overestimation of IR and IGF1R occurs when using fluorophore-conjugated peptide ligands such as FITC-insulin, which in addition to binding cognate receptors, also bind with measurable affinity to non-cognate and hybrid IR-IGF1R.

Multiple lines of research have shown that the binding of insulin to IR is negatively cooperative *in vitro* [20, 39] with insulin binding to IR at two sites, each with a distinct K_D [40, 41]. Similarly, our results show that FITC-insulin binds two classes of sites on 2H3-RBL cells

and exhibits an upward curving Scatchard plot. This curvilinear Scatchard plot is commonly seen during examination of insulin binding and was previously observed by Zhong and coworkers when examining rhodamine-labeled insulin (Rh-insulin) binding to human renal cells using FCS [42]. These investigators attributed such curvilinear Scatchard plots either to the negative cooperative binding of insulin to IR or to separate classes of receptors with differing affinities for insulin. However, FCS monitors the number of separately diffusing species and is somewhat insensitive to the absolute brightness of each species. Once a FITC-insulin or Rh-insulin molecule binds to an individual IR, the binding of subsequent fluorophore-labeled insulin molecules to this IR, despite changing the absolute magnitude of fluorescence fluctuations as the receptor enters and exits the interrogation volume, has only a limited effect on the normalized autocorrelation function [3]. With this in mind, we suggest that the majority of receptors observed in the present work on live 2H3-RBL cells that bind FITC-insulin with low affinity, and those observed by Zhong and coworkers that bind Rh-insulin with low affinity [42], may not be IR but are more likely either IGF1R or IR-IGF1R hybrids.

Negative cooperativity in insulin binding to IR was apparent from our measurements of FITC-insulin dissociation. Our results demonstrate that FITC-insulin dissociation varied with the concentration of excess insulin available in solution. FITC-insulin dissociation initially accelerated with increasing concentrations of excess insulin, but then decreased at insulin concentrations above 10^{-8} M. However, in the absence of excess insulin, the dissociation rate of FITC-insulin was independent of the initial labeling concentration. Acceleration of ligand dissociation in response to excess solution-phase ligand can indicate negatively-cooperative binding and, while not necessarily relevant physiologically, the effects of insulin concentrations above 10^{-8} M provide insight into the mechanism of insulin binding to IR and support the harmonic oscillator model of insulin and IGF1 binding proposed by Kiselyov and coworkers [17].

Our results also demonstrate that FITC-insulin, insulin and IGF1 compete for binding to available receptors on live 2H3-RBL cells. At a FITC-insulin labeling concentration of 0.1 nM, approximately equal to FITC-insulin's high-affinity site K_D, the binding of FITC-insulin and insulin are quite similar, indicating that conjugation of fluorescein to insulin does not affect IR binding, and values of K_I obtained for IGF1 competing with 0.1 nM FITC-insulin agree with existing literature showing that IR can bind IGF1 with nM affinity [20]. At higher levels of receptor occupancy, obtained by increasing the labeling concentration of FITC-insulin, the affinities of insulin and IGF1 relative to FITC-insulin appear to decrease. This may result from FITC-insulin binding to a combination of IR, IGF1R and IR-IGF1R hybrids when used at higher labeling concentrations or, alternatively, may result from multivalent binding of FITC-insulin to receptors.

Like IR, IGF1R exhibits complex ligand binding kinetics [43, 44], binding its cognate ligand IGF1 strongly, but also binding insulin with nM affinity [20]. Evidence also suggests that IR-IGF1R hybrids, much like IGF1R, bind IGF1 strongly, but can also bind insulin with nM affinity [45-48]. We found that 67 sites μm^{-2} of the 124 sites μm^{-2} that bind insulin with low affinity also bind IGF1 with high affinity. This suggests that these receptors are likely not IR, but rather are either IGF1R or IR-IGF1R hybrids. However, the total number of receptors identified using FITC-insulin on 2H3-RBL cells was only slightly more than half the combined number of receptors identified using IR- and IGF1R-specific antibodies, suggesting that a substantial portion of these receptors are in fact IR-IGF1R hybrids.

The current model describing the formation of IR and IGF1R homodimers and IR-IGF1R hybrids assumes that IR and IGF1R monomers randomly associate to form dimers within the endoplasmic reticulum [27]. This model predicts that the ratio (R) of IR monomers to IGF1R monomers produces IR homodimers, IR-IGF1R hybrids and IGF1R homodimers at relative fractions of R^2:2R:1 [27]. If the results of receptor-specific antibody experiments are used as a

first approximation of the ratio of IR monomers to IGF1R monomers on these cells, this model predicts that nearly two thirds of the species identified as either IR or IGF1R are actually IR-IGF1R hybrids. Since receptor-specific labeling indicated the surface density of IR monomer-containing species is 190 μm^{-2}, this suggests that only 63 μm^{-2} of these species are actual IR homodimers, which is similar to the 49 receptors μm^{-2} on these cells that bind FITC-insulin with high affinity. This model also predicts an IGF1R homodimer density of approximately 54 μm^{-2}, a value similar to the 67 receptors μm^{-2} we identified that bind IGF1 with high affinity. Given the known similarity between the K_D's of IGF1R and IR-IGF1R hybrids for IGF1, we anticipated that nearly all of the 161 receptors μm^{-2} identified with IGF1R specific antibody would have bound IGF1 with high affinity. However, this discrepancy is likely the result of our inability to directly observe IGF1 binding. Taken together, our results suggest that the ratios of IR to IR-IGF1R hybrids to IGF1R on live 2H3-RBL cells is between 1:2:1 and 2:3:1 and are generally consistent with random association of IR and IGF1R monomers in the endoplasmic reticulum.

5. ACKNOWLEDGEMENTS

We would like to thank Jonathan Gerding for his assistance with alignment of FCS instrumentation. This project was supported in part by the NSF (CHE0628260, MCB1024688) and by the American Heart Association (AHA0650081Z).

6. FIGURE LEGENDS

Figure 1: Normalized autocorrelation functions for fluorescent probes in solution and bound to receptors on the surface of live 2H3-RBL cells. [●] FITC-insulin (aqueous), [○] FITC-avidin (aqueous), [Δ] FITC-insulin (live cells), [▼] FITC-avidin (bound to IR specific antibody on live cells), [■] FITC-avidin (bound to FcεRI specific antibody on live cells). To improve clarity not all time points are shown.

Figure 2: Equilibrium binding of receptor specific antibodies to live 2H3-RBL cells. Binding of FITC-avidin to cells labeled with increasing concentrations of, A) [●] FcεRI specific antibody, B) [●] IRα-specific antibody, also shows that pre-incubation of cells with [▲] 10 μM insulin or medium containing [□] 10% FBS has no effect on antibody labeling of IR, C) [●] IRβ-specific antibody, or D) [●] IGF1Rα-specific antibody before labeling with biotinylated secondary antibody.

Figure 3: A) [●] Equilibrium binding of FITC-insulin to receptors on the surface of serum starved 2H3-RBL cells was fit to a two-site sequential model. B) [●] Scatchard analysis of FITC-insulin binding displays a concave-up curvilinear pattern.

Figure 4: [●] Indirect observation of IGF1 binding to live 2H3-RBL cells. Pre-incubation with increasing concentrations of IGF1 reduced the apparent binding of 250 nM FITC-insulin to live cells.

Figure 5: Competitive binding of insulin and IGF1 to receptors on 2H3-RBL cells. A) Competitive binding of insulin and [●] 0.1 nM, [○] 1 nM, [▼] 10 nM, or [Δ] 50 nM FITC-insulin to receptors on 2H3-RBL cells. B) Competitive binding of IGF1 and [●] 0.1 nM, [○] 1 nM, or [▼] 10 nM FITC-insulin to receptors on 2H3-RBL cells.

Figure 6: Dissociation of insulin and IGF1 from receptors on 2H3-RBL cells. A) Dissociation of [●] 1 nM, [○] 10 nM, or [▼] 100 nM FITC-insulin from receptors on live 2H3-RBL cells in the absence of excess aqueous insulin. For each condition, every data point shown is from a different cell. B) [●] Effects of excess aqueous insulin on the dissociation of FITC-insulin from live 2H3-RBL cells. The k_{off} of FITC-insulin initially increases with increasing insulin concentrations but then, at concentrations of insulin $>10^{-8}$ nM, decreases. C) [●] The dissociation of 10nM IGF1 is shown. Data points represent the reduction in the binding of 250 nM FITC-insulin compared to cells not pre-incubated with IGF1.

7. REFERENCES

[1] B. Goldstein, R.G. Posner, D.C. Torney, J. Erickson, D. Holowka and B. Baird, Competition between solution and cell surface receptors for ligand. Dissociation of hapten bound to surface antibody in the presence of solution antibody Biophysical Journal 56 (1989) 955-966.

[2] J. Erickson, B. Goldstein, D. Holowka and B. Baird, The effect of receptor density on the forward rate constant for binding of ligands to cell surface receptors Biophysical Journal 52 (1987) 657-662.

[3] P. Schwille, U. Haupts, S. Maiti and W.W. Webb, Molecular dynamics in living cells observed by fluorescence correlation spectroscopy with one- and two-photon excitation Biophysical Journal 77 (1999) 2251–2265.

[4] S.A. Kim, K.G. Heinze and P. Schwille, Fluorescence correlation spectroscopy in living cells 4 (2007) 963-973.

[5] D.E. Magde, Elliot; Webb, Watt, Thermodynamic fluctuations in a reacting system-measurement by fluorescence correlation spectroscopy Physical Review Letters 29 (1972) 705-708.

[6] E.L. Elson and D. Magde, Fluorescence correlation spectroscopy. I. conceptual basis and theory Biopolymers 13 (1974) 1-27.

[7] D. Magde, E.L. Elson and W.W. Webb, Fluorescence correlation spectroscopy. II. An experimental realization Biopolymers 13 (1974) 29-61.

[8] W. Webb, Commentary on the pleasure of solving impossible problems of experimental physiology Annual Review of Physiology 68 (2006) 1-28.

[9] H.-T. He and D. Marguet, Detecting nanodomains in living cell membrane by fluorescence correlation spectroscopy Annual Review of Physical Chemistry 62 (2011) in press.

[10] P. Schwille. in Cell Biochemistry and Biophysics, Vol. 34, pp. 383-408, Humana Press Inc. 2001.

[11] P. Schwille, J. Korlach and W. Webb, Fluorescence correlation spectroscopy with single-molecule sensitivity on cell and model membranes Cytometry 36 (1999) 176-182.

[12] J. Ries and P. Schwille, New concepts for fluorescence correlation spectroscopy on membranes Physical Chemistry 10 (2008) 3487-3497.

[13] A. Pramanik and R. Rigler, Ligand-receptor interactions in the membrane of cultured cells monitored by fluorescence correlation spectroscopy Biological Chemistry 382 (2001) 371-378.

[14] S. Saffarian, U. Li, E. Elson and L. Pike, Oligomerization of the EGF receptor investigated by life cell fluorescence intensity distribution analysis Biophysical Journal 93 (2007) 1021-1031.

[15] T. Sudhaharan, P. Liu, Y.H. Foo, W. Bu, K.B. Lim, T. Wohland and S. Ahmed, Determination of in vivo dissociation constant, KD, of Cdc42-effector complexes in live mammalian cells using single wavelength fluorescence cross-correlation spectroscopy Journal of Biological Chemistry 284 (2009) 13602-13609

[16] V. Vukojevic, D.K. Papadopoulos, L. Terenius, W.J. Gehring and R. Rigler, Quantitative study of synthetic Hox transcription factor DNA interactions in live cells Proceedings of the National Academy of Sciences 107 (2010) 4093-4098

[17] V.V. Kiselyov, S. Versteyhe, L. Gauguin and P. De Meyts, Harmonic oscillator model of the insulin and IGF1 receptors' allosteric binding and activation 5 (2009).

[18] L. Gauguin, B. Klaproth, W. Sajid, A.S. Andersen, K.A. McNeil, B.E. Forbes and P. De Meyts, Structural basis for the lower affinity of the insulin-like growth factors for the insulin receptor Journal of Biological Chemistry 283 (2008) 2604-2613

[19] J. Dupont and D. LeRoith, Insulin and insulin-like growth factor 1 receptors: similarities and differences in signal transduction Hormone Research 55 (2001) 22-26.

[20] P. De Meyts and J. Whittaker, Structural biology of insulin and IGF1 receptors: implications for drug design Nature Reviews, Drug Discovery 1 (2002).

[21] C.M. Taniguchi, B. Emanuelli and C.R. Kahn, Critical nodes in signalling pathways: insights into insulin action 7 (2006) 85-96.

[22] M.C. Lawrence, N.M. McKern and C.W. Ward, Insulin receptor structure and its implications for the IGF-1 receptor Current Opinion in Structural Biology Catalysis and regulation / Proteins 17 (2007) 699-705.

[23] C. Ward, M. Lawrence, V. Streltsov, T. Garrett, N. McKern, M.-Z. Lou, G. Lovrecz and T. Adams, Structural insights into ligand-induced activation of the insulin receptor Acta Physiologica 192 (2008) 3-9.

[24] H. Zhang, A. Pelzer, D. Kiang and D. Yee, Down-regulation of Type 1 insulin-like growth factor receptor increases sensitivity of breast cancer cells to insulin Cancer Research 67 (2007) 391-397.

[25] G. Pandini, R. Vigneri, A. Costantino, F. Frasca, A. Ippolito, Y. Fujita-Yamaguchi, K. Siddle, A. Goldfine and A. Belfiore, Insulin and insulin-like growth factor-1 (IGF-1) receptor overexpression in breast cancer leads to insulin/IGF-1 hybrid receptor overexpression: evidence for a second mechanism of IGF-1 signaling Clinical Cancer Research 5 (1999) 1935-1944.

[26] A.M. Rowzee, D.L. Ludwig and T.L. Wood, Insulin-like growth factor type 1 receptor and insulin receptor isoform expression and signaling in mammary epithelial cells Endocrinology 150 (2009) 3611-3619.

[27] E. Bailyes, B. Nave, M. Soos, S. Orr, A. Hayward and K. Siddle, Insulin receptor/IGF-1 receptor hybrids are widely distributed in mammalian tissues: quantification of individual receptor species by selective immunoprecipitation and immunoblotting Biochemical Journal 327 (1997) 209-215.

[28] K. Fogarty, J. McPhee, E. Scott and A. Van Orden, Probing the ionic atmosphere of single-stranded DNA using continuous flow capillary electrophoresis and fluorescence correlation spectroscopy Anal. Chem. 81: (2009) 465-472.

[29] T.J. Stasevich, F. Mueller, A. Michelman-Ribeiro, T. Rosales, J.R. Knutson and J.G. McNally, Cross-validating FRAP and FCS to quantify the impact of photobleaching on in vivo binding estimates Biophysical Journal 99 (2010) 3093-3101.

[30] Y. Cheng and W.H. Prusoff, Relationship between the inhibition constant (K1) and the concentration of inhibitor which causes 50 per cent inhibition (I50) of an enzymatic reaction Biochem Pharmacol. 22 (1973) 3099-108.

[31] S. Chiantia, J. Ries and P. Schwille, Fluorescence correlation spectroscopy in membrane structure elucidation Biochimica et Biophysica Acta 1788 (2009) 225-233.

[32] R. Das, S. Hammond, D. Holowka and B. Baird, Real-time cross-correlation image analysis of early events in IgE receptor signaling Biophysical Journal 94 (2008) 4996-5008.

[33] D.A. Roess, S.M.L. Smith, P. Winter, J. Zhou, P. Dou, B. Baruah, A.M. Trujillo, N.E. Levinger, X. Yang, B.G. Barisas and D.C. Crans, Effects of vanadium-containing compounds on membrane lipids and on microdomains used in receptor-mediated signaling Chemistry & Biodiversity 5 (2008) 1558-1570.

[34] Y. Chen, A.C. Munteanu, Y.-F. Huang, J. Phillips, Z. Zhu, M. Mavros and W. Tan, Mapping receptor density on live cells by using fluorescence correlation spectroscopy Chemistry - A European Journal 15 (2009) 5327-5336.

[35] N. Andrews, K. Lidke, J. Pfeiffer, A. Burns, B. Wilson, J. Oliver and D. Lidke, Actin restricts FcεRI diffusion and facilitates antigen-induced receptor immobilization Nature Cell Biology 10 (2008) 955-963.

[36] N.L. Andrews, J.R. Pfeiffer, A.M. Martinez, D.M. Haaland, R.W. Davis, T. Kawakami, J.M. Oliver, B.S. Wilson and D.S. Lidke, Small, mobile FcεRI receptor aggregates are signaling competent Immunity 31 (2009) 469-479.

[37] W.S. Hlavacek, A.S. Perelson, B. Sulzer, J. Bold, J. Paar, W. Gorman and R.G. Posner, Quantifying aggregation of IgE-FcεRI by multivalent antigen Biophysical journal 76 (1999) 2421-2431.

[38] R. Rigler, A. Pramanik, P. Jonasson, G. Kratz, O.T. Jansson, P.-Ã. Nygren, S. Stahl, K. Ekberg, B.-L. Johansson, S. Uhlen, M. Uhlen, H. Jörnvall and J. Wahren, Specific binding of proinsulin C-peptide to human cell membranes Proceedings of the National Academy of Sciences of the United States of America 96 (1999) 13318-13323

[39] L. Schäffer, A model for insulin binding to the insulin receptor European Journal of Biochemistry 221 (1994) 1127-1132.

[40] L. Whittaker, C. Hao, W. Fu and J. Whittaker, High-affinity insulin binding: insulin interacts with two receptor ligand binding sites Biochemistry 47 (2008) 12900-12909.

[41] C. Hao, L. Whittaker and J. Whittaker, Characterization of a second ligand binding site of the insulin receptor Biochemical and Biophysical Research Communications 347 (2006) 334-339.

[42] Z.-H. Zhong, A. Pramanik, K. Ekberg, O.T. Jansson, H. Jörnvall, J. Wahren and R. Rigler, Insulin binding monitored by fluorescence correlation spectroscopy Diabetologia 44 (2001) 1184-1188.

[43] K.H. Surinya, B.E. Forbes, F. Occhiodoro, G.W. Booker, G.L. Francis, K. Siddle, J.C. Wallace and L.J. Cosgrove, An investigation of the ligand binding properties and negative cooperativity of soluble insulin-like growth factor receptors Journal of Biological Chemistry 283 (2008) 5355-5363

[44] A. Chakravarty, J. Hinrichsen, L. Whittaker and J. Whittaker, Rescue of ligand binding of a mutant IGF-I receptor by complementation Biochemical and Biophysical Research Communications 331 (2005) 74-77.

[45] A. Belfiore, F. Frasca, G. Pandini, L. Sciacca and R. Vigneri, Insulin receptor isoforms and insulin receptor/insulin-like growth factor receptor hybrids in physiology and disease Endocr Rev 30 (2009) 586-623.

[46] S. Benyoucef, K.H. Surinya, D. Hadaschik and K. Siddle, Characterization of insulin/IGF hybrid receptors: contributions of the insulin receptor L2 and Fn1 domains and the alternatively spliced exon 11 sequence to ligand binding and receptor activation Biochem J 403 (2007) 603-613.

[47] G. Pandini, F. Frasca, R. Mineo, L. Sciacca, R. Vigneri and A. Belfiore, Insulin/Insulin-like growth factor 1 hybrid receptors have different biological characteristics depending on the insulin receptor isoform involved Journal of Biological Chemistry 277 (2002) 39684-39695.

[48] M. Soos, C. Field and K. Siddle, Purified hybrid insulin/insulin-like growth factor-I receptors bind insulin-like growth factor-I, but not insulin, with high affinity Biochemical Journal 290 (1993) 419-426.

Table 2.1: Surface density of IR, IGF1R and FcεRI on 2H3-RBL cells and binding parameters of the primary antibody used to identify each receptor.

Receptor	Antibody	N[1]	σ (receptors μm^{-2})	Total receptors[2]	K_D (nM)[3]
IR	IRα	34.6±1.2	190±7	60,000±2,000	23±4
IR	IRβ	35.8±4.5	196±25	62,000±8,000	163±56
IGF1R	IGF1Rα	29.3±1.2	161±7	51,000±2,000	2±1
FcεRI	FcεRIα	98.4±19.6	540±108	170,000±34,000	61±23

[1]*N* is the effective number of particles detected in the FCS laser-spot at saturating concentrations of primary receptor-specific antibody.

[2]Value for total receptors per cell assumes the surface area of a 2H3-RBL cell is 314μm^{-2} [32].

[3]Values presented for K_D reflect the binding of primary antibody to specific receptors on live 2H3-RBL cells.

Table 2.2: Equilibrium binding of FITC-insulin to receptors on the surface of live 2H3-RBL cells.

Binding Site	N[1]	σ (receptors μm^{-2})	Total receptors[2]	K_D (nM)[3]
1	9.0±1.1	49±6	15,000±2,000	0.11±0.05
2	22.6±1.4	124±8	39,000±3,000	75±23

[1]N is the upper limit for detected particles for sites 1 and 2.

[2]Value for total receptors per cell assumes the surface area of a 2H3-RBL cell is 314μm^{-2} [32].

[3]Values presented for K_D were obtained using a two-site sequential model of ligand-receptor binding.

Table 2.3: Reduced binding of FITC-insulin to receptors on 2H3-RBL cells after pre-incubation with insulin, FBS or IGF1.

Treatment	N[1]	Diff (N)[2]
None	24.8±5.1	NA
Insulin (10μM)	2.0±1.6	22.8±5.1
FBS (10%)	4.6±1.0	20.2±5.1
IGF1 (0.1nM)	19.8±1.6	5.2±5.1
IGF1 (1nM)	14.1±3.1	10.9±5.1
IGF1 (10nM)	12.9±0.8	12.1±5.1

[1]N is the number of particles detected after labeling with 250nM FITC-insulin.

[2]Estimated as the difference between the number of FITC-insulin bound to untreated cells and to cells with the indicated pre-treatment.

Table 2.4: Competitive binding of insulin and FITC-insulin to receptors on live 2H3-RBL cells.

[FITC-insulin] (nM)	$I_{1/2}$ (nM)[1]	K_I (nM)[2]	N_{max}[3]	N_o[4]
0.1	0.18±0.02	0.09±0.01	5.9±0.1	1.1±0.1
1	5.4±1.6	0.54±0.16	9.1±0.3	1.3±0.3
10	47.4±3.4	0.52±0.04	10.4±0.1	1.0±0.1
50	590±250	1.29±0.55	12.4±0.2	2.1±0.8

[1]$I_{1/2}$ values were obtained by fitting binding data for insulin concentrations between 10^{-4} and 10^{5} nM to equation (7).

[2]Values for K_I were obtained from $I_{1/2}$ using equation (8).

[3]N_{max} is the apparent number of particles detected in the absence of competing insulin.

[4]N_o is the apparent number of particles detected at saturating insulin concentrations.

Table 2.5: Competitive binding of IGF1 and FITC-insulin to receptors on live 2H3-RBL cells.

[FITC-insulin] (nM)	$I_{1/2}$ (nM)[1]	K_I (nM)[2]	N_{max}[3]	N_o[4]
0.1	21.1±8.1	9.4±3.6	5.9±0.1	0.7±0.4
1	143.7±72.4	10.9±5.5	9.6±0.2	0.5±0.1
10	1727.6±N.A.	14.5±N.A.	10.7±0.5	1±N.A.

[1]$I_{1/2}$ values were obtained by fitting binding data for IGF1 concentrations between 10^{-3} and 10^{3} nM to equation (7).

[2]Values for K_I were obtained from $I_{1/2}$ using equation (8).

[3]N_{max} is the apparent number of particles detected in the absence of competing IGF1.

[4]N_o is the apparent number of particles detected at saturating IGF1 concentrations.

Table 2.6: Rate of FITC-insulin and IGF1 dissociation from receptors on 2H3-RBL cells.

Ligand	Concentration (nM)	k_{off} (min^{-1})	$t_{1/2}$ (min)[1]
FITC-insulin	1	0.014±0.001	50±4
FITC-insulin	10	0.017±0.001	41±4
FITC-insulin	100	0.015±0.001	46±4
IGF1	10	0.013±0.004	52±16

[1]Value for $t_{1/2}$ determined using the approximation $t_{1/2} = 0.69/k_{off}$.

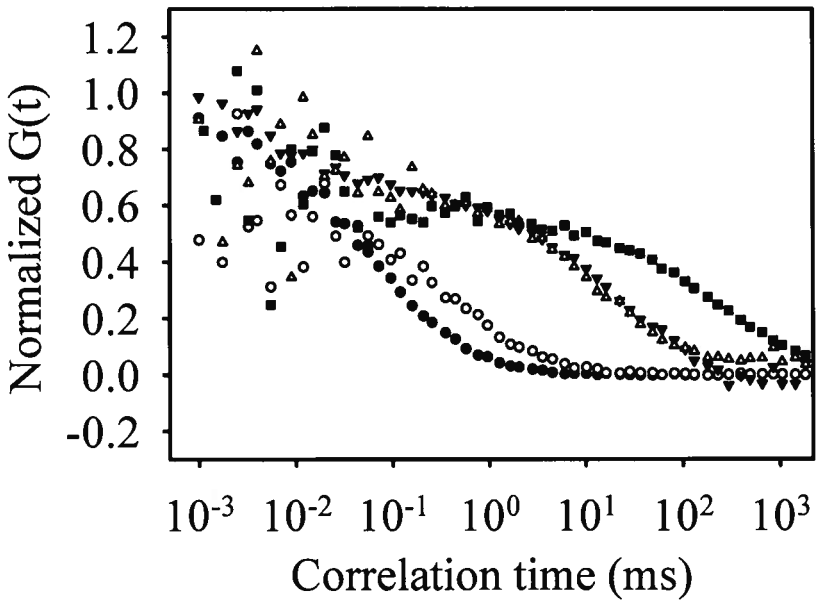
Normalized G(t)
1.2
1.0
0.8
0.6
0.4
0.2
0.0
-0.2
10-3 10-2 10-1 100 101 102 103
Correlation time (ms)

Figure 2.1

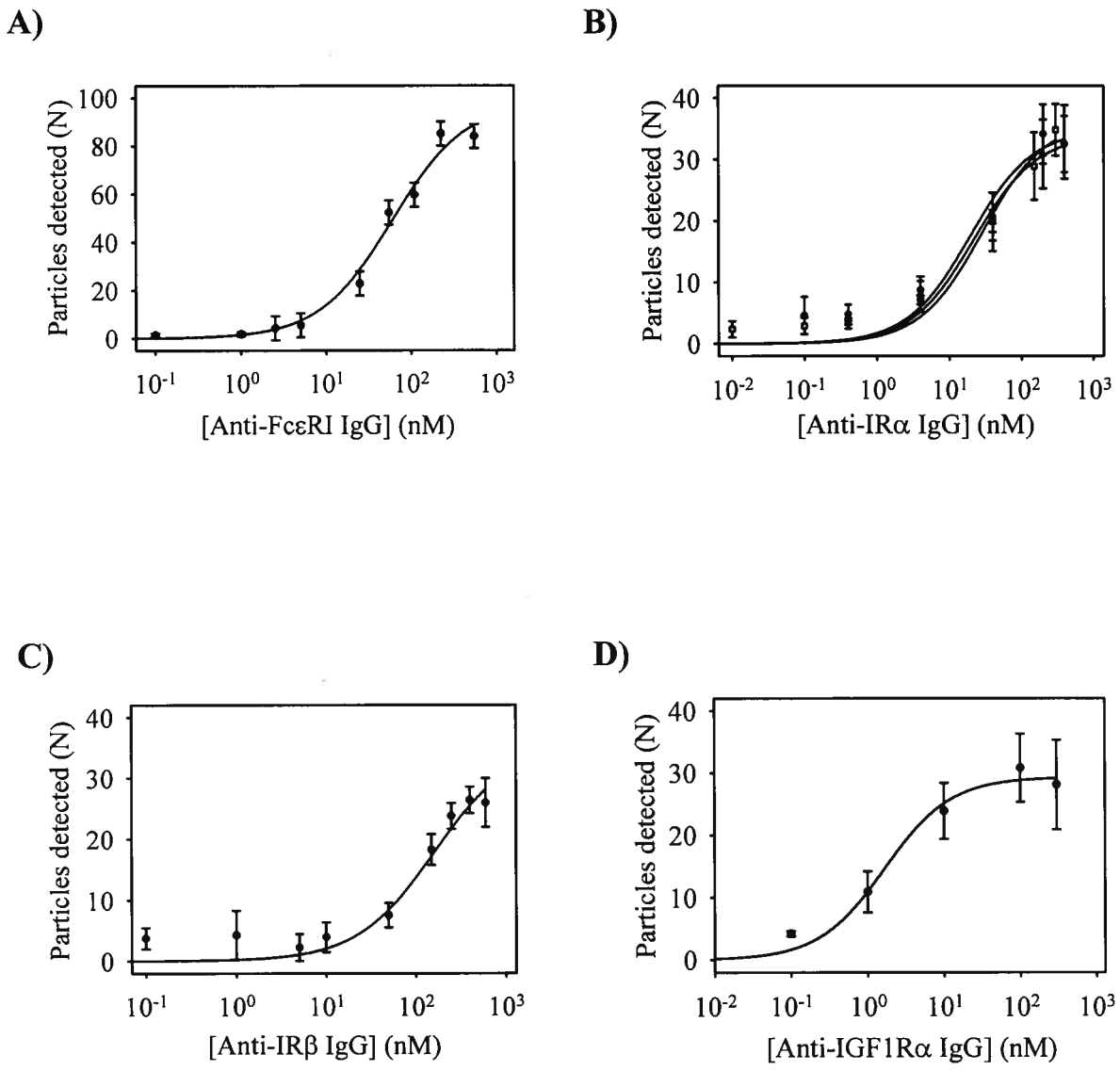
A)
Particles detected (N)
100
80
60
40
20
0
10^{-1} 10^{0} 10^{1} 10^{2} 10^{3}
[Anti-FcεRI IgG] (nM)
B)
Particles detected (N)
40
30
20
10
0
10^{-2} 10^{-1} 10^{0} 10^{1} 10^{2} 10^{3}
[Anti-IRα IgG] (nM)
C)
Particles detected (N)
40
30
20
10
0
10^{-1} 10^{0} 10^{1} 10^{2} 10^{3}
[Anti-IRβ IgG] (nM)
D)
Particles detected (N)
40
30
20
10
0
10^{-2} 10^{-1} 10^{0} 10^{1} 10^{2} 10^{3}
[Anti-IGF1Rα IgG] (nM)

Figure 2.2

A)

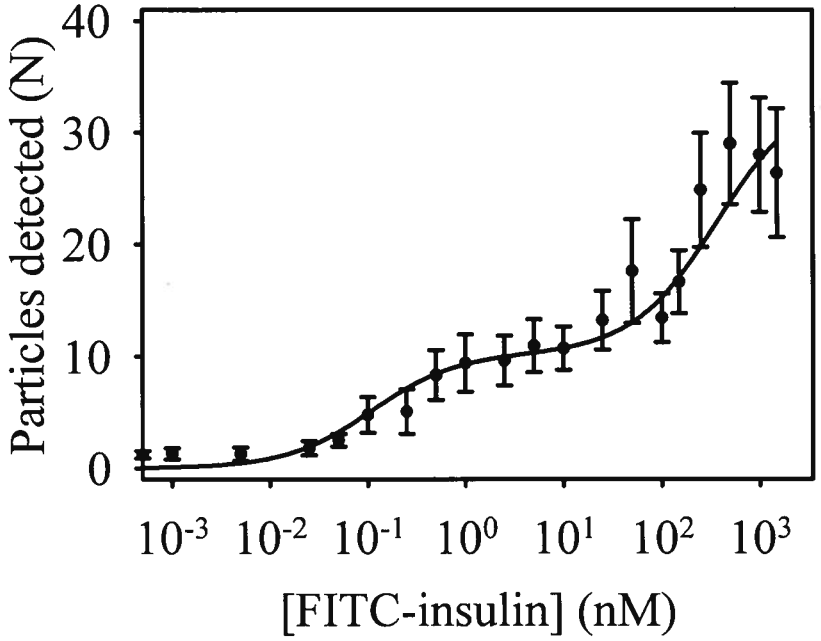
Particles detected (N)
0
10
20
30
40
10-3 10-2 10-1 100 101 102 103
[FITC-insulin] (nM)

B)

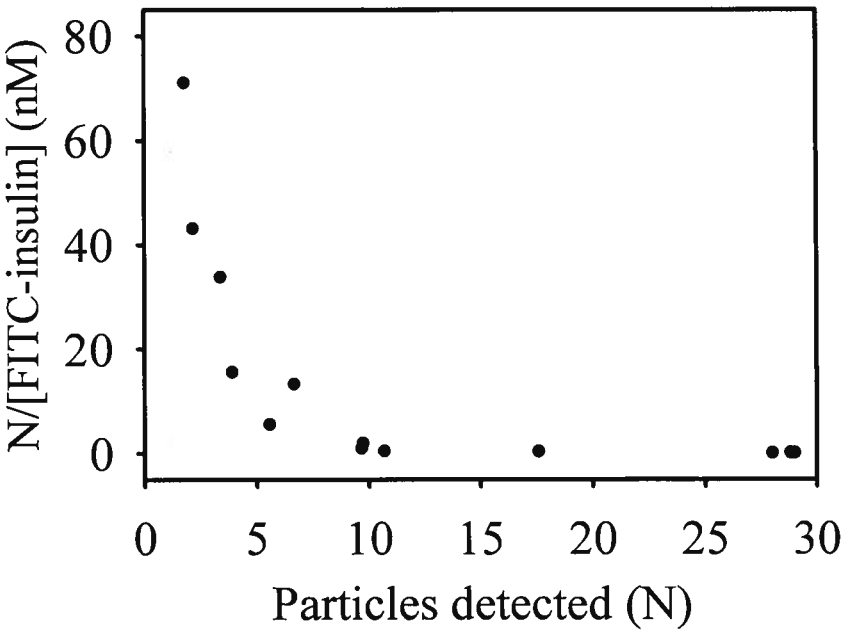
N/[FITC-insulin] (nM)
0
20
40
60
80
0 5 10 15 20 25 30
Particles detected (N)

Figure 2.3

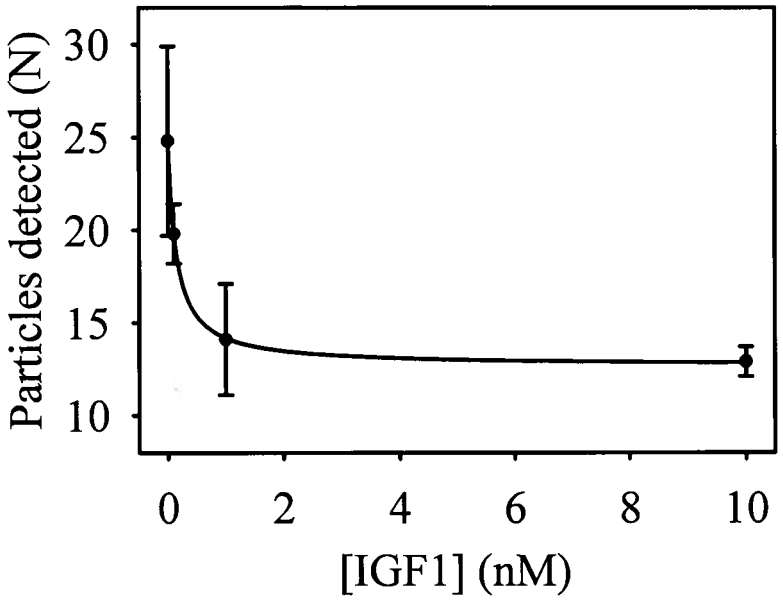

Figure 2.4

A)

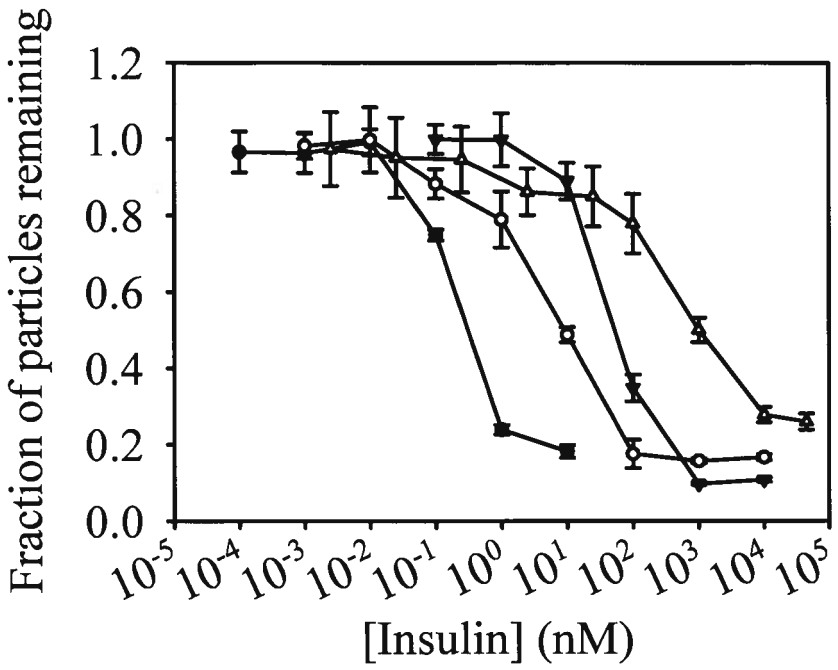
Fraction of particles remaining
1.2
1.0
0.8
0.6
0.4
0.2
0.0
10-5 10-4 10-3 10-2 10-1 100 101 102 103 104 105
[Insulin] (nM)

B)

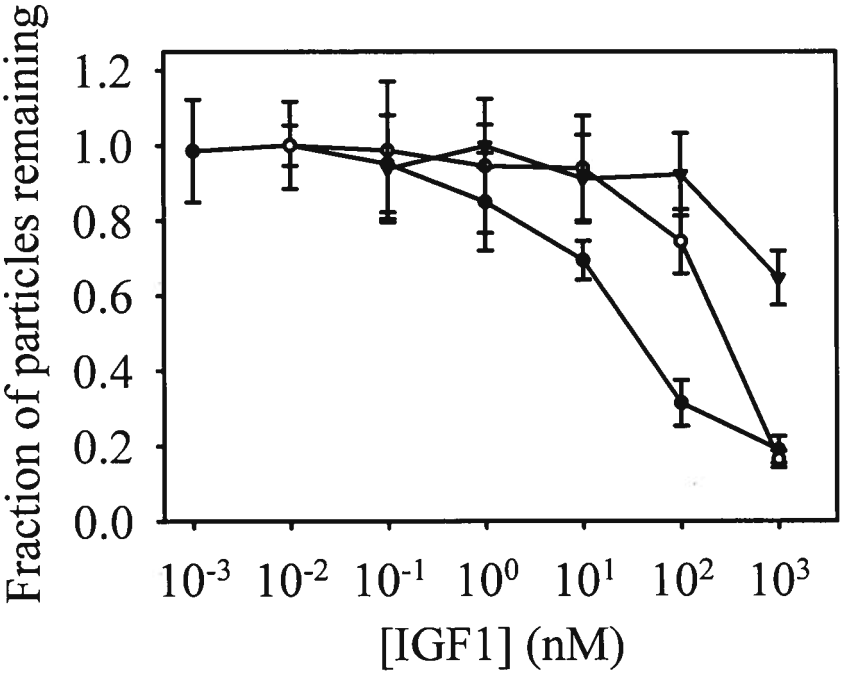
Fraction of particles remaining
1.2
1.0
0.8
0.6
0.4
0.2
0.0
10-3 10-2 10-1 100 101 102 103
[IGF1] (nM)

Figure 2.5

A)

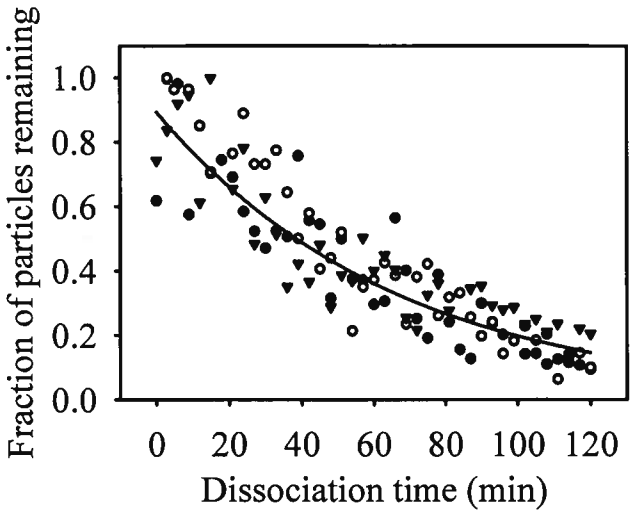

B)

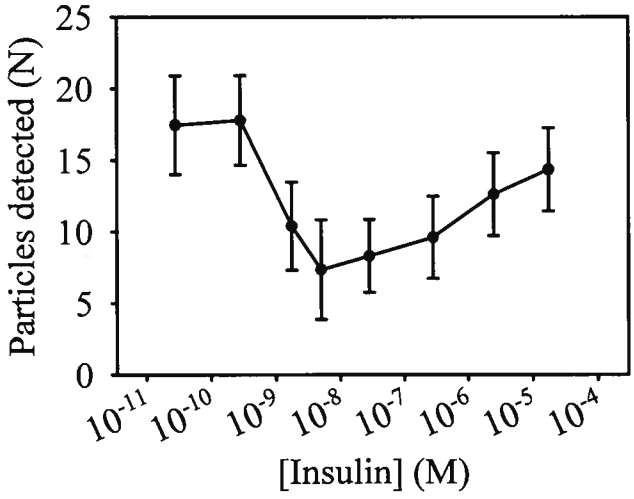

C)

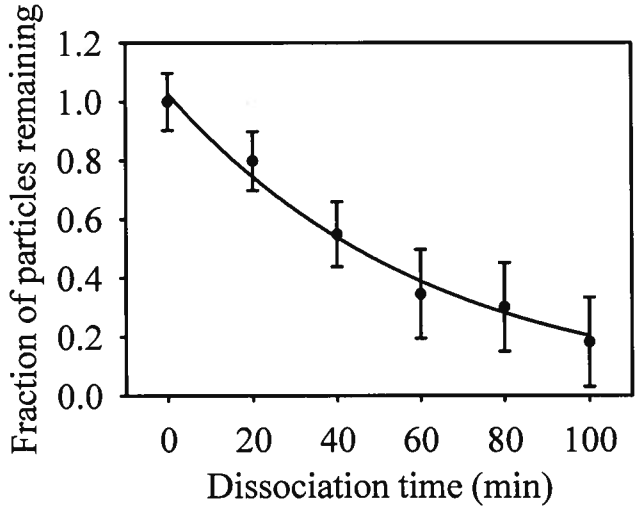

Figure 2.6

Chapter III: Peter W. Winter performed fluorescence correlation spectroscopy shown in Figure 3 and fluorometric assessment of live cell lipid order shown in Figure 4

Insulin Receptors and Downstream Substrates Associate With Membrane Microdomains After Treatment With Insulin or Chromium(III) Picolinate

Abeer Al-Qatati[1,*], Peter W. Winter[2,*], Amber L. Wolf-Ringwall[1], Pabitra B. Chatterjee[3], Alan K. Van Orden[3], Debbie C. Crans[2,3], Deborah A. Roess[1,2] and B. George Barisas[2,3,#],

[1]Department of Biomedical Sciences, [2]Cell and Molecular Biology Program, [3]Department of Chemistry, Colorado State University, Fort Collins, Colorado 80523, *These authors contributed equally to this manuscript, [#]Address all correspondence and requests for reprints to: B. George Barisas, Department of Chemistry, Campus Mail 1872, Colorado State University, Fort Collins, CO 80523. Email: barisas@lamar.colostate.edu

We have examined the association of insulin receptors (IR) and downstream signaling molecules with membrane microdomains in rat basophilic leukemia (RBL-2H3) cells following treatment with insulin or tris(2-pyridinecarbxylato)-chromium(III) ($Cr(pic)_3$). Single-particle tracking demonstrated that individual IR on these cells exhibited reduced lateral diffusion and increased confinement within 100 nm-scale membrane compartments after treatment with either 200 nM insulin or 10 μM $Cr(pic)_3$. These treatments also increased the association of native IR, phosphorylated insulin receptor substrate 1 and phosphorylated AKT with detergent-resistant, cholesterol-containing, membrane microdomains of characteristically high buoyancy. Confocal fluorescence microscopic imaging of Di-4-ANEPPDHQ labeled RBL-2H3 cells also showed that plasma membrane lipid order decreased following treatment with $Cr(pic)_3$ but was not altered by insulin treatment. Fluorescence correlation spectroscopy demonstrated that $Cr(pic)_3$ did not affect IR cell-surface density or compete with insulin for available binding sites. Finally, Fourier transform infrared spectroscopy indicated that $Cr(pic)_3$ likely associates with the lipid interface in reverse micelle model membranes. Taken together, these results suggest that activation of IR signaling by both insulin and $Cr(pic)_3$ involves retention of IR in specialized nanometer-scale membrane microdomains but that the insulin-like effects of $Cr(pic)_3$ are due to changes in membrane lipid order rather than to direct interactions with IR.

Keywords: Insulin, membrane microdomain, chromium, reverse micelle, lipid order, single particle tracking

Introduction

To better understand how chromium-containing compounds mediate insulin receptor (IR) signaling, we compared the effects of insulin and tris(2-pyridinecarbxylato)-chromium(III) $Cr(pic)_3$ on the lateral motions of individual IR diffusing on the surface of live rat basophilic leukemia (RBL-2H3) cells and on the association of IR and downstream targets with chemically-isolated, cholesterol-containing plasma membrane microdomains of characteristically high buoyancy (1). We also examined the effect of $Cr(pic)_3$ on the density of native IR on the surface of live RBL-2H3 cells using fluorescence correlation spectroscopy (FCS) and on live RBL-2H3 cell membrane lipid-order using ratiometric confocal fluorescence imaging of the phase-sensitive lipid probe Di-4-ANEPPDHQ.

Our results demonstrate that cell treatment with either insulin or $Cr(pic)_3$ reduces both individual IR lateral diffusion and the size of IR-containing cell-surface compartments and causes the accumulation of IR, phosphorylated IRS-1 (pIRS-1) and phosphorylated AKT (pAKT) in relatively buoyant, detergent-resistant membrane microdomains. However, while treatment with $Cr(pic)_3$ significantly decreases cell-surface membrane lipid order on intact cells, treatment with insulin does not. Additionally, FCS suggests that $Cr(pic)_3$ does not interact directly with IR or affect IR cell-surface density. Together, these results demonstrate that insulin and $Cr(pic)_3$ increase association of IR and downstream targets with specialized, cell-surface membrane microdomains and suggest that the insulin-like activity of $Cr(pic)_3$ is likely due to decreases in membrane lipid order rather than to direct interactions with IR.

Multiple lines of research indicate that IR and downstream targets interact with cholesterol-containing membrane microdomains during insulin-mediated IR signaling (2-7). Specifically, investigators have demonstrated that cholesterol-containing membrane microdomains facilitate IR signaling by organizing IR and downstream targets of phosphorylated insulin receptor (pIR) such

as TC-10(6), IRS-1 (7), PIP2 (8) and the CAP/Cbl complex(9). Additionally, chromium-containing compounds are known mediators of IR function and chromium supplementation has been shown to improve insulin sensitivity in multiple studies (10-16). Specifically, there is an increase in the translocation of GLUT4 to the plasma membrane in the skeletal muscle of obese, hyperinsulinemic, JCR-LA corpulent rats in response to $Cr(pic)_3$ (17). Moreover, CHO cells expressing IR exhibit increased IR phosphorylation in response to treatment with various chromium(III) compounds (18). A small number of human trials have shown improvements in both insulin sensitivity and oxidative stress tests after treatments with $Cr(pic)_3$ (11, 12, 19-21).

Despite the well-described effects of chromium supplementation on insulin-mediated IR signaling, the mechanism underlying these effects remains unclear. It has been suggested that chromium supplementation increases the number of cell-surface IR (22). However, this is not evident from the results of other studies, including one where chromium supplementation had no effect on IR numbers or the transcription of insulin-like substrate 1 (IRS-1) mRNA in skeletal muscle tissue of male KK/H1J mice (15). Alternatively, it has also been suggested that the activity of chromium-containing compounds either involves a small, chromium-binding oligopeptide known as LMWCr or chromodulin (23, 24) which is postulated to bind both chromium and insulin-IR complexes, increasing the tyrosine-kinase activity of IR (23), or that chromium-containing compounds, including $Cr(pic)_3$, decrease membrane lipid order, rather than having direct effects on IR or IR-binding proteins (14, 25).

Materials and Methods

Materials

Minimum Essential Medium (MEM) with Earle's Balanced Salts was purchased from Thermo Scientific (Logan, Utah). Fetal bovine serum (FBS) was purchased from Gemini BioProducts (Woodland, CA). Insulin from bovine pancreas, anti-phospho(Tyr^{972})-insulin receptor, methyl-β-

cyclodextrin (MβCD), FITC-avidin, and anti-rabbit-biotin were purchased from Sigma-Aldrich (St. Louis, MO). Anti-insulin receptor-β (C-19), anti-insulin receptor-α (N-20), anti-phospho(Ser^{474})-AKT and anti-phospho(Tyr^{632})-IRS-1 were purchased from Santa Cruz Biotechnology (Santa Cruz, CA). Colloidal gold (40 nm) was purchased from Ted Pella, Inc (Redding, CA). The phase-sensitive aminonaphthylethenylpyridinum-based dye Di-4-ANEPPDHQ was purchased from Invitrogen (Carlsbad, CA). Complete mini protease inhibitor cocktail tablets were purchased from Roche (Indianapolis, IN). 35mm, #1.5 glass bottom petri dishes were purchased from Willco Wells (Amsterdam, Netherlands). $Cr(pic)_3$ was synthesized and characterized as previously described(26, 27).

Cell culture

2H3 rat basophilic leukemia (RBL-2H3) cells were maintained in cell medium that included MEM supplemented with Earle's Balanced Salts and 10% FBS, 200 mM L-glutamine, 10,000 U/mL penicillin G, 10 μg/mL streptomycin and 25 μg/mL Fungizone (Gemini BioProducts). In some experiments, cells were incubated in supplemented MEM without FBS overnight to remove a source of insulin and other growth factors.

Single particle tracking of individual insulin receptors

Lateral diffusion of individual IR on live RBL-2H3 cells was measured using slight modifications of established protocols (28). 40 nm nanogold particles were stabilized with the lowest possible concentration of bovine serum albumin (BSA) containing a small amount of anti-IRα antibody. The amount of anti-IRα antibody used in the preparation of the gold complexes was adjusted to the lowest possible concentration that resulted in binding of approximately 5-10 visible gold particles on the apical surface of each cell. Binding of gold-anti-IRα conjugates to cells was preventable by pre-labeling cells with an excess of unconjugated anti-IRα antibody. In some experiments, cells were treated with 200 nM insulin for 30 min after labeling of IR with an IR α-

subunit specific antibody or with 10 μM $Cr(pic)_3$ for 12 h before labeling. Individual nanoparticles were imaged by differential interference contrast with a 1.4 NA, 63x objective in a Zeiss Axiovert 135 microscope. Images were acquired using a Dage IFG-300 camera and were recorded for two minutes (3600 frames) at approximately 30 nm/pixel under the control of Metamorph 6 imaging software (Molecular Devices). The trajectories for individual gold particles were segmented into domains by examining the variance in particle position over various time windows as previously described (29, 30). Diffusion coefficients and the size of compartments accessed by individual IR were also determined using established procedures (29-31).

Isolation of plasma membrane rafts

RBL-2H3 cells were incubated with either 200 nM insulin for 1 hr at 37°C, with 10 μM $Cr(pic)_3$ overnight at 37°C or with both 10 μM $Cr(pic)_3$ overnight and then 200 nM insulin for 1 hr at 37°C. To isolate membrane rafts from RBL-2H3 cells, $5x10^7$ cells were washed two times with phosphate-buffered saline, pH 7.2 (PBS) and lysed for 5-10 minutes on ice in 1 mL of a buffer containing 25 mM MES, 150 mM NaCl, 2mM EDTA, 0.25% Triton-X100, and a protease inhibitor cocktail including aprotinin, leupeptin, EDTA, and phenylmethylsulfonyl fluoride (Roche). A low speed 300x g spin was used to remove cell nuclei and large cell debris. Supernatant from this spin (1 mL), which contained plasma membrane fragments, was then combined with an equal volume of 80% sucrose containing 0.25% Triton-X100 and the protease inhibitors to produce a 40% sucrose solution. A discontinuous sucrose gradient containing equal volumes of 10-80% sucrose was created with the sample in 40% sucrose layered within this gradient. The gradient was loaded into a Beckman SW-41 swinging bucket rotor and spun at 175,000x g for 20 hr at 4°C. After the spin, eighteen 650 μL fractions were carefully collected from the top of the gradient downward. A 50 μL aliquot from each fraction was diluted 1:1 with

95% SDS and 5% β-mercaptoethanol. Proteins of interest from fractions containing >40% sucrose or <40% sucrose were identified by Western blotting as previously described (32), and the relative amount of each protein was determined using a Bio-Rad GS-800 calibrated densitometer. Sucrose concentrations were determined from refractive indices using a Bausch and Lomb refractometer. In some experiments, cells were treated for 1hr at 37°C with 10 mM methyl-β-cyclodextrin (MβCD), a cholesterol sequestering agent (33), in serum-free medium after incubation with either insulin or $Cr(pic)_3$.

Fluorescence correlation spectroscopy measurements of cell-surface insulin receptor density and insulin binding

RBL-2H3 cells were seeded onto sterile dishes and treated with 10 μM insulin for 1 h or 10 μM $Cr(pic)_3$ overnight. Cells were then sequentially washed and labeled with anti-IRα (N-20) rabbit IgG (SantaCruz Bio) for 30-40 min, anti-rabbit-biotin IgG (Sigma) for 20 min, and FITC-avidin for 15 min, washed and then submerged in 1 mL buffer. Alternatively, cells were labeled with FITC-insulin (Invitrogen) and then washed 4 times for 30 secs in 1mL of buffer. Fluorescence correlation spectroscopy (FCS) experiments were performed using a modified Nikon TE1000 inverted microscope equipped with a 100x, 1.25NA oil-immersion objective, an Omnichrome Melles-Griot multi-line air-cooled argon ion laser operating at 514.5 nm, 570/32 nm band pass filters, two PerkinElmer photon counting modules (SPCM-AQR-14) and an ALV-6010 digital hardware correlator (34). The $1/e^2$ radius of the excitation beam at the sample was determined to be 241nm from measurements of aqueous rhodamine-6G diffusion (data not shown). Samples were illuminated briefly (~10sec) before acquisition of data to irreversibly photobleach immobile particles (39). Data were then collected for 20 sec during which time the average fluorescence of the sample remained relatively constant (data not shown). Correlation data were analyzed

according to established procedures using Igor Pro 5.05A to yield the surface density of diffusing FITC-insulin particles in the laser beam (35-38).

Evaluation of RBL-2H3 cell plasma membrane lipid order

RBL-2H3 cells were seeded onto sterile dishes and treated with 200 nM insulin for 1hr or with 0.1, 1.0 or 10 μM $Cr(Pic)_3$ overnight. In some experiments, cells were treated with 10mM MβCD for 1hr to deplete membrane cholesterol (40). After the various treatments, cells were labeled with 1.0 μM Di-4-ANEPPDHQ for 30 minutes, washed and immersed in buffer for imaging. Confocal fluorescence images were acquired using an Olympus IX-71 inverted microscope equipped with a 60x, 1.2NA water-immersion objective and a FV 300 confocal scanning unit. Cell samples were illuminated with a 488 nm laser. Fluorescence emission, split between detector channels 1 and 2 using a 570 nm dichroic mirror, was collected simultaneously in channel 1 up to 530 nm and in channel 2 using a 605 nm band-pass filter. All images were collected at identical instrument and detector settings with the exception of the laser excitation power which was adjusted between experiments due to slight variations in labeling efficiency. Background correction and the background-corrected ratio of fluorescence emission at 605 nm to that at 530 nm (red/green) were calculated using NIH Image J 1.42i.

Evaluation of $Cr(pic)_3$ in reverse-micelle model-membranes using Fourier transformed infrared spectroscopy

Microemulsion samples were prepared from 5 mM $Cr(pic)_3$ in 2.5% D_2O in H_2O (pH 7.2) and 0.2 M AOT in isooctane at ($[H_2O]/[AOT]$) ratios (w_o) of 6, 10 and 18 using established procedures (41). As controls, microemulsions containing 100 mM sodium picolinate (Na(pic)) at pH 7.5 and samples containing 5 mM $Cr(pic)_3$ in H_2O and 0.2 M AOT in isooctane were also prepared by similar methods. All samples examined were nominally transparent. FTIR spectra were recorded on a Nicolet Magna 760 spectrophotometer. Samples were examined in BaF_2 2 mm IR

microcuvettes with Teflon spacers of 0.050 mm thickness. Samples prepared in H_2O were subtracted from samples containing 2.5 % D_2O in H_2O. Emission peak wavelengths are presented in (nm) and represent the average of 128 scans with 1.0 cm^{-1} resolution.

Results

Insulin receptors exhibit restricted lateral diffusion in response to insulin or Cr(pic)$_3$

In SPT experiments individual IR on RBL-2H3 cells labeled with anti-IR antibody-colloidal gold complexes exhibit slower lateral diffusion and are retained in small, nanometer-scale plasma membrane compartments in response to insulin or $Cr(pic)_3$ (Table 3.1, Figure 3.1). The average lateral diffusion coefficient of IR in cells incubated in serum-free medium for at least 12 h is approximately $1x10^{-11}cm^2s^{-1}$ and is slowed following exposure to insulin or $Cr(pic)_3$ to about $5x10^{-12}cm^2s^{-1}$, although these values were not statistically different. However, the size of the compartments accessed by individual IR decreased significantly from 216±23 nm to 113±16 nm and 119±19 nm after insulin and $Cr(pic)_3$ treatments, respectively (Table 3.1 and Figure 3.1). Treatment with both insulin and $Cr(pic)_3$ together also appeared to reduce the size of compartments accessed by IR to 98±16 nm although this did not differ significantly from the effect of insulin or $Cr(pic)_3$ treatments alone.

Insulin receptors associate with detergent-resistant membrane microdomains after exposure to insulin or Cr(pic)$_3$

Treatment of RBL-2H3 cells with 200 nM insulin for 1h, 10 μM $Cr(pic)_3$ for 1h or 12 h or both 200 nM insulin and 10 μM $Cr(pic)_3$ together for 1h resulted in the increased association of IR with relatively-buoyant, detergent-resistant, membrane microdomains (Table 3.2). Following isopycnic sucrose gradient ultracentrifugation of membranes isolated from RBL-2H3 cells incubated overnight in serum-free medium prior to Triton X-100 extraction, 2±1% of total IR

were associated with buoyant, detergent-resistant fractions (<40% sucrose) and 98±1% of total IR were located in the less buoyant bulk membrane (>40% sucrose) (Table 3.2 and Figure 3.2). Treatment of RBL-2H3 cells with 200 nM insulin or 10 μM $Cr(pic)_3$ significantly increased IR in detergent-resistant fractions. Following exposure to 200 nM insulin, 21±10% of IR were associated with detergent-resistant membrane fractions, while 32±8% of IR were localized within these fractions after treatment with 10 μM $Cr(pic)_3$. Simultaneous insulin and $Cr(pic)_3$ treatments increased the amount of IR in detergent resistant fractions to 48±3%. Alternatively, pretreatment of cells for 1 hr with 10 mM MβCD resulted in only small amounts of IR appearing in detergent-resistant fractions despite insulin treatment (data not shown). Interestingly, the distribution of phoshorylated IR (pIR) between detergent-resistant and bulk membrane fractions was similar in untreated cells and in cells treated with either insulin or $Cr(pic)^3$ (Table 3.2 and Figure 3.2).

Phosphorylated IRS-1 and phosphorylated AKT associate with detergent-resistant membrane microdomains after exposure to insulin or $Cr(pic)_3$

Overnight incubation of RBL-2H3 cells in serum-free medium resulted in 95% of pIRS-1 localizing in bulk membrane fractions (Table 3.3). Treatment with 200 nM insulin or 10 μM $Cr(pic)_3$ for 1h increased the proportion of pIRS-1in detergent -resistant fractions from 5±4% to 62±19% and 58±29%, respectively. Alternatively, treatment of cells with MβCD reduced pIRS-1 detergent-resistant fraction localization, with 91±1% of pIRS-1 appearing in the bulk membrane (Table 3.3).

Examination of the effects of insulin and $Cr(pic)_3$ suggest that pAKT distributes within the plasma membrane and localizes to detergent resistant membrane microdomains in connection with the activation of IR signaling (Table 3.3). Treatment of cells with 200 nM insulin for 1 hr resulted in 58±13% of pAKT associating with these fractions while 1 h treatment with 10 μM $Cr(pic)_3$ resulted in association of 60±7% of pAKT with detergent-resistant fractions.

Alternatively, treatment of cells with 10 mM MβCD reduced the amount of pAKT appearing in these fractions to 22±9%.

$Cr(pic)_3$ does not alter insulin receptor surface density or insulin binding capacity

The effects of $Cr(pic)_3$ on IR surface density and insulin binding capacity were investigated using fluorescence correlation spectroscopy. Equilibrium binding of FITC-insulin to RBL-2H3 cells demonstrates that these cells have approximately 100 cell-surface FITC-insulin binding sites μm^{-2} (Figure 3.3). Treatment with $Cr(pic)_3$ did not appear to reduce the number of IR on these cells or compete with insulin for binding to available binding sites. However, FITC-insulin binding was almost completely blocked by pretreatment for 1 h with 10 μM insulin or overnight incubation in medium containing 10% fetal bovine serum, which itself contains insulin and other hormones (Figure 3.3). Thus apparently $Cr(pic)_3$ does not interfere with IR ligand-binding.

$Cr(pic)_3$ decreases cell surface plasma membrane lipid order

We investigated the effects of insulin and $Cr(pic)_3$ on RBL-2H3 cell membrane lipid order using the small-molecule, phase-sensitive, lipid-probe Di-4-ANEPPDHQ, which exhibits both red-shifted fluorescence emission and increased fluorescence lifetime as membrane lipid order decreases (42-45). Ratiometric confocal imaging of Di-4-ANEPPDHQ's two peak emission wavelengths (red/green), indicates the relative plasma membrane lipid-order in RBL-2H3 cells, either treated with 200 nM insulin or incubated in serum-free medium for over 12 h, are similar. This suggests that insulin binding to IR and the accumulation of IR in detergent-resistant membrane microdomains has little if any effect on the lipid order of the plasma membrane (Figure 3.4). However, treatment of cells with increasing amounts of $Cr(pic)_3$ results in significant decreases in RBL-2H3 cell-surface membrane order. Control experiments also indicate that depleting membrane cholesterol content using MβCD also significantly decreases the order of RBL-2H3 cell plasma membranes (Figure 3.4) (46).

$Cr(pic)_3$ localizes to the lipid-water interface in reverse-micelle model membranes

Decreases in overall plasma membrane order in RBL-2H3 cells in response to short-term exposure to $Cr(pic)_3$ suggest a direct interaction between $Cr(pic)_3$ and the lipid bilayer. To address this, we examined the effects of $Cr(pic)_3$ on the hydrogen bond network in the aqueous water pool of AOT/isooctane RM microemulsions (Table 3.4). Use of 2.5 % D_2O in H_2O allows observation of the O-D stretch (47) and the effects of $Cr(pic)_3$ on the H-bond network of the 'water pool' contained within the RM. The size of the water pool affects O-D peak absorption position (48) as shown in Table 3.4. The O-D peak position did not change upon addition of $Cr(pic)_3$ to any of the samples examined. Control experiments conducted with the picolinate ligand alone used a higher concentration of picolinate compared to those using $Cr(pic)_3$, due to differences in molecular size and solubility. However, even these higher concentrations of picolinate did not change the O-D peak position. In comparison, previous experiments demonstrate that changes are observed in the O-D peak position when using 32 mM decavanadate, a molecule known to reside in the water pool of this type of RM microemulsion system (49). These results suggest that $Cr(pic)_3$ localizes at, or possibly penetrates, the interfacial region of RM microemulsions and are consistent with studies examining the effects of chromium-containing compounds on lipid packing in other membrane model systems including, Langmuir monolayers (Audra Sostarecz, personal communication).

Discussion

Treatment of RBL-2H3 cells with insulin or $Cr(pic)_3$ reduces the average size of cell-surface compartments accessed by IR and increases accumulation of IR, pIRS-1 and pAKT within detergent-resistant membrane microdomains. Although the dynamic association of IR or downstream targets including IRS-1 and AKT with cholesterol-containing membrane microdomains has been demonstrated previously (7, 50), to our knowledge this work is the first to

demonstrate association of IR, pIRS-1 and pAKT with nanometer-scale membrane microdomains in response to treatment with $Cr(pic)_3$.

Previous studies have demonstrated that $Cr(pic)_3$ supplementation improves glucose levels in insulin-resistant KK/HIJ diabetic mice (15) where it increases pIR numbers without having any apparent effect on PTP1B activity (17). Because of this, it has been proposed that effects of $Cr(pic)_3$ result from increased expression of IR and downstream substrates (22). However, in our studies, short term exposure of live cells to $Cr(pic)_3$ for 1 hr or overnight, had no effect on the surface density of FITC-insulin binding sites. This is similar to results obtained by several other investigators (15, 17) and, although effects of $Cr(pic)_3$ on unphosphorylated IRS-1 and AKT were not examined here, a recent study also demonstrates that total IRS-1 and AKT levels are not altered by chromium treatment (17). This suggests that the increased levels of pIRS-1 and pAKT observed in our work resulted from increased activity of pIR in response to insulin or $Cr(pic)_3$ treatments.

The mechanism involved in $Cr(pic)_3$ activation of IR appears to be markedly different from that of insulin. Unlike insulin, which interacts directly with IR, our results indicate $Cr(pic)_3$ decreases lipid order in a concentration-dependent fashion, as has been reported previously (14, 25). Because cholesterol-containing membrane fragments presumably remain intact on $Cr(pic)_3$-treated cells, the mechanism regulating $Cr(pic)_3$ mediated decreases in membrane lipid order is also distinctly different from that of MβCD. Our results suggest that $Cr(pic)_3$ alters the partitioning of IR and downstream substrates in cholesterol-containing membrane microdomains and the bulk plasma membrane. We propose that the general decrease in lipid order of the bulk membrane affects the preferential association of membrane proteins, such as IR, with specialized, cholesterol-containing membrane microdomains, leading to increased receptor signaling.

The relationship between membrane lipid order and activation of IR signaling has previously been proposed for other compounds with insulin-like properties. For instance, IR signaling efficacy has been shown to increase with decreased plasma membrane order in isolated rat adipocytes, presumably due to increased activation of IR (51), and several groups have suggested that the effects of the anti-diabetic drug *N*,*N*-dimethylimidodicarbonimidic diamide (Metformin) may be related to changes in both cell-surface lipid order and membrane physiology (52-54). Reducing plasma membrane order in response to Metformin appears to increase the rate of GLUT4 vesicle translocation to the cell-surface (55), perhaps by concentrating IR within specialized, cholesterol-containing membrane microdomains.

Our results also underscore the importance of membrane microdomains as signaling platforms for IR function. Increased association of IR with these microdomains may also increase the association of IR with downstream molecules involved in cell signaling. Disruption of these specialized microdomains by depletion of membrane cholesterol and subsequent effects on cellular signaling have been demonstrated for a variety of small molecules (56) and transmembrane receptors (57, 58), including the IR where cholesterol depletion using MβCD has been shown to reduce both GLUT4-dependant glucose uptake and IRS-1 phosphorylation (50). In addition to IR, interactions with specialized membrane microdomains have also been shown to modulate the signaling of other cell-surface receptors. This includes apoptosis of T-cell leukemia and multiple myeloma cells by raft localized Fas/CD95 receptors in response to Resveratrol (59), T-cell antigen signaling (60) and signaling by MHC class II molecules (61).

Here, we have shown that the activation of IR by insulin in RBL-2H3 cells is accompanied by the association of IR, pIRS-1 and pAKT with nanometer-scale membrane microdomains exhibiting high buoyancy and increased lipid packing compared to the bulk membrane. Although these microdomains serve as signaling platforms for IR in both insulin and $Cr(pic)_3$ treated cells, the

mechanisms involved in accumulation of IR in these microdomains differ. We have also shown that $Cr(pic)_3$ treatment decreases lipid order in the bulk plasma membrane, but have found no evidence of direct interaction between $Cr(pic)_3$ and IR. Taken together, these observations suggest that changes in IR compartmentalization and preferred local environment can modulate IR activation regardless of whether IR are occupied by ligand.

Acknowledgements

This work was supported by the NSF (CHE0628260, MCB1024668) and the American Heart Association (AHA0650081Z). We would like to thank Prof. Audra Sostarecz, Monmouth College, for her helpful discussions concerning chromium-containing compounds and Langmuir monolayers.

Figure legends

Figure 1: Single particle tracking of individual insulin receptors on live RBL-2H3 cells. A) Diffusion coefficients of individual IR conjugated gold particles plotted versus the average size of compartments occupied. B) The size distribution of compartments accessed by individual IR. Each reported value is the mean and SEM of measurements on 20 individual particles.

Figure 2: Localization of insulin receptors in various density sucrose fractions after isopycnic centrifugation of RBL-2H3 cell membrane fragments . Before exposure to insulin or $Cr(pic)_3$, IR appeared in high density sucrose fractions. Treatment with 200 nM insulin or 10 μM $Cr(pic)_3$ causes redistribution of IR into lower density fractions. Each reported value is the mean and SEM for at least 3 individual experiments. To improve clarity not all conditions examined are shown

Figure 3: Insulin receptor surface density on live RBL-2H3 cells as measured by fluorescence correlation spectroscopy. Pre-treatment with 10 μM $Cr(pic)_3$ did not reduce the number of IR binding sites while pre-treatment with 10 μM insulin or incubation in medium supplemented with 10% FBS, reduced binding of FITC-insulin. Each reported value is the mean and SD of measurements from at least 14 individual cells. To improve clarity not all conditions examined are shown.

Figure 4: **Fluorometric assessment of live RBL-2H3 cell plasma membrane lipid order**. Membrane bound Di-4-ANEPPDHQ fluorescence emission at 605nm (red) to that at 530 nm (green) increases as lipid order decreases. Compared to RBL-2H3 cells starved of 10% FBS overnight, there was a significant increase in the ratio of Di-4ANEPPDHQ fluorescence in cells following treatment with 10 μM $Cr(pic)_3$, indicating a decrease in membrane lipid order. An even greater increase in the ratio of Di-4-ANNEPDHQ fluorescence was observed after treatment with 10 mM MβCD to deplete membrane cholesterol. Alternatively, loading cells with excess cholesterol decreased the ratio of Di-4-ANEPPDHQ fluorescence. Treatment with insulin or 10% FBS had no effect on the ratio of Di-4-ANEPPDHQ fluorescence. Each reported value is the mean and SD of measurements from at least 15 cells. Values marked with a,b,c,d significantly different ($p<0.02$) from *, using an unpaired Students t-test with two-tailed distribution.

References

1. Lingwood, D., and K. Simons. 2010. Lipid rafts as a membrane-organizing principle. Science 327:46-50.

2. Ishikawa, Y., K. Otsu, and J. Oshikawa. 2005. Caveolin; different roles for insulin signal? Cellular Signalling 17:1175-1182.

3. Nystrom, F., H. Chen, L.-N. Cong, Y. Li, and M. Quon. 1999. Caveolin-1 interacts with the insulin receptor and can differentially modulate insulin signaling in transfected Cos-7 cells and rat adipose cells. Mol Endocrinol 13:2013-2024.

4. Kim, K.-B., B.-W. Kim, H.-J. Choo, Y.-C. Kwon, B.-Y. Ahn, J.-S. Choi, J.-S. Lee, and Y.-G. Ko. 2009. Proteome analysis of adipocyte lipid rafts reveals that gC1qR plays essential roles in adipogenesis and insulin signal transduction. Proteomics 9:2373-2382.

5. Czech, M. 2000. PIP2 and PIP3: Complex roles at the cell surface. Cell 100:603-606.

6. Maffucci, T., A. Brancaccio, E. Piccolo, R. C. Stein, and M. Falasca. 2003. Insulin induces phosphatidylinositol-3-phosphate formation through TC10 activation. 22:4178-4189.

7. Müller, G., C. Jung, S. Wied, S. Welte, and W. Frick. 2001. Insulin-mimetic signaling by the sulfonylurea glimepiride and phosphoinositolglycans involves distinct mechanisms for redistribution of lipid raft components. Biochemistry. 40:14603-14620.

8. Yamaguchi, H., M. Shiraishi, K. Fukami, A. Tanabe, Y. Ikeda-Matsuo, Y. Naito, and Y. Sasaki. 2009. MARCKS regulates lamellipodia formation induced by IGF-I via association with PIP2 and *F*-actin at membrane microdomains. J. Cell. Physiol. 220:748-755.

9. Baumann, C. A., V. Ribon, M. Kanzaki, D. C. Thurmond, S. Mora, S. Shigematsu, P. E. Bickel, J. E. Pessin, and A. R. Saltiel. 2000. CAP defines a second signalling pathway required for insulin-stimulated glucose transport. Nature 407:202-207.

10. Anderson, R. A. 1998. Chromium, Glucose Intolerance and Diabetes. J Am Coll Nutr 17:548-555.

11. Anderson, R., M. Polansky, N. Bryden, and J. Canary. 1991. Supplemental-chromium effects on glucose, insulin, glucagon, and urinary chromium losses in subjects consuming controlled low-chromium diets. Am J Clin Nutr 54:909-916.

12. Martin, J., Z. Q. Wang, X. H. Zhang, D. Wachtel, J. Volaufova, D. E. Matthews, and W. T. Cefalu. August 2006 Chromium picolinate supplementation attenuates body weight gain and increases insulin sensitivity in subjects with type 2 diabetes. Diabetes Care 29 1826-1832

13. Yang, X., K. Palanichamy, A. C. Ontko, M. N. A. Rao, C. X. Fang, J. Ren, and N. Sreejayan. 2005. A newly synthetic chromium complex - chromium(phenylalanine)3

improves insulin responsiveness and reduces whole body glucose tolerance. FEBS Letters 579:1458-1464.

14. Chen, G., P. Liu, G. R. Pattar, L. Tackett, P. Bhonagiri, A. B. Strawbridge, and J. S. Elmendorf. 2006. Chromium activates glucose transporter 4 trafficking and enhances insulin-stimulated glucose transport in 3T3-L1 adipocytes via a cholesterol-dependent mechanism. Mol Endocrinol 20:857-870.

15. Chen, W.-Y., C.-J. Chen, C.-H. Liu, and F. C. Mao. 2009. Chromium supplementation enhances insulin signalling in skeletal muscle of obese KK/HlJ diabetic mice. Diabetes, Obesity and Metabolism 11:293-303.

16. Pattar, G. R., L. Tackett, P. Liu, and J. S. Elmendorf. 2006. Chromium picolinate positively influences the glucose transporter system via affecting cholesterol homeostasis in adipocytes cultured under hyperglycemic diabetic conditions. Mutation Research/Genetic Toxicology and Environmental Mutagenesis1st Workshop on Chromium and Human Health 610:93-100.

17. Wang, Z. Q., X. H. Zhang, J. C. Russell, M. Hulver, and W. T. Cefalu. 2006. Chromium picolinate enhances skeletal muscle cellular insulin signaling in vivo in obese, insulin-resistant JCR:LA-cp rats. J. Nutr. 136:415-420.

18. Wang, H., A. Kruszewski, and D. L. Brautigan. 2005. cellular chromium enhances activation of insulin receptor kinase. Biochemistry 44:8167-8175.

19. Ravina, A., L. Slezak, N. Mirsky, N. A. Bryden, and R. A. Anderson. 1999. Reversal of corticosteroid-induced diabetes mellitis with supplemental chromium. Diabetic Medicine 16:164-167.

20. Anderson, R. A., N. Cheng, N. A. Bryden, M. M. Polansky, J. Chi, and J. Feng. 1997 Elevated intakes of supplemental chromium improve glucose and insulin variables in individuals with type 2 diabetes. Diabetes 46 1786-1791

21. Cheng, H.-H., M.-H. Lai, W.-C. Hou, and C.-L. Huang. 2004. Antioxidant effects of chromium supplementation with type 2 diabetes mellitus and euglycemic subjects. Journal of Agricultural and Food Chemistry 52:1385-1389.

22. Anderson, R. A., M. M. Polansky, N. A. Bryden, S. J. Bhathena, and J. J. Canary. 1987. Effects of supplemental chromium on patients with symptoms of reactive hypoglycemia. Metabolism 36:351-355.

23. Davis, C. M., and J. B. Vincent. 1997. Chromium oligopeptide activates insulin receptor tyrosine kinase activity Biochemistry 36:4382-4385.

24. Peterson, R. L., K. J. Banker, T. Y. Garcia, and C. F. Works. 2008. Isolation of a novel chromium(III) binding protein from bovine liver tissue after chromium(VI) exposure. Journal of Inorganic Biochemistry 102:833-841.

25. Evans, G. W., and T. D. Bowman. 1992. Chromium picolinate increases membrane fluidity and rate of insulin internalization. Journal of Inorganic Biochemistry 46:243-250.

26. Evans, G. W., and D. J. Pouchnik. 1993. Composition and biological activity of chromium-pyridine carboxylate complexes. Journal of Inorganic Biochemistry 49:177-187.

27. Niemann, A., U. Bossek, G. Haselhorst, K. Wieghardt, and B. Nuber. 1996. Synthesis and characterization of six-coordinate nitrido complexes of vanadium(V), chromium(V), and manganese(V). Isolation of a dinuclear, mixed-valent nitrido chromium(III)/chromium(V) species. Inorganic Chemistry 35:906-915.

28. Dietrich, C., B. Yang, T. Fujiwara, A. Kusumi, and K. Jacobson. 2002. Relationship of lipid rafts to transient confinement zones detected by single particle tracking. Biophys J 82:274-284.

29. Murase, K., T. Fujiwara, Y. Umemura, K. Suzuki, R. Iino, H. Yamashita, M. Saito, H. Murakoshi, K. Ritchie, and A. Kusumi. 2004. Ultrafine membrane compartments for molecular diffusion as revealed by single molecule techniques. Biophys J 86:4075-4093.

30. Daumas, F., N. Destainville, C. Millot, A. Lopez, D. Dean, and L. Salomé. 2003. Confined diffusion without fences of a G protein coupled receptor as revealed by single particle tracking. Biophysical Journal 84:356-366.

31. Saxton, M. J. 1997. Single-particle tracking: the distribution of diffusion coefficients. Biophys J 72:1744-1753.

32. Roess, D. A., and S. M. L. Smith. 2003. Self-association and raft localization of functional luteinizing hormone receptors. Biol Reprod 69:1765-1770.

33. Christian, A. E., M. P. Haynes, M. C. Phillips, and G. H. Rothblat. 1997. Use of cyclodextrins for manipulating cellular cholesterol content. J Lipid Res 38:2264-2272.

34. Fogarty, K., J. McPhee, E. Scott, and A. Van Orden. 2009. Probing the ionic atmosphere of single-stranded DNA using continuous flow capillary electrophoresis and fluorescence correlation spectroscopy. Anal. Chem. 81::465-472.

35. Ruan, Q., Y. Chen, E. Gratton, M. Glaser, and W. W. Mantulin. 2002. Cellular characterization of adenylate kinase and its isoform:two-photon excitation fluorescence imaging and fluorescence correlation spectroscopy. Biophysical Journal 83:3177-3187.

36. Ries, J., and P. Schwille. 2008. New concepts for fluorescence correlation spectroscopy on membranes. Physical Chemistry 10:3487-3497.

37. Schwille, P., U. Haupts, S. Maiti, and W. W. Webb. 1999. Molecular dynamics in living cells observed by fluorescence correlation spectroscopy with one- and two-photon excitation. Biophysical Journal 77:2251–2265.

38. Chen, Y., A. C. Munteanu, Y.-F. Huang, J. Phillips, Z. Zhu, M. Mavros, and W. Tan. 2009. Mapping receptor density on live cells by using fluorescence correlation spectroscopy. Chemistry - A European Journal 15:5327-5336.

39. Chiantia, S., J. Ries, and P. Schwille. 2009. Fluorescence correlation spectroscopy in membrane structure elucidation. Biochimica et Biophysica Acta 1788:225-233.

40. Singh, P., Y. D. Paila, and A. Chattopadhyay. 2007. Differential effects of cholesterol and 7-dehydrocholesterol on the ligand binding activity of the hippocampal serotonin1A receptor: Implications in SLOS. Biochemical and Biophysical Research Communications 358:495-499.

41. Stahla, M. L., B. Baruah, D. M. James, M. D. Johnson, N. E. Levinger, and D. C. Crans. 2008. 1H NMR studies of aerosol-OT reverse micelles with alkali and magnesium counterions: preparation and analysis of MAOTs. Langmuir 24:6027-6035.

42. Jin, L., A. Millard, J. Wuskell, H. Clark, and K. Loew. 2005. Cholesterol-enriched lipid domains can be visualized by di-4-ANEPPDHQ with linear and nonlinear optics. Biophysical Journal 90:2563-2575.

43. Jin, L., A. C. Millard, J. P. Wuskell, X. Dong, D. Wu, H. A. Clark, and L. M. Loew. 2006. Characterization and application of a new optical probe for membrane lipid domains. Biophysical Journal 90:2563-2575.

44. Wang, Y., G. Jing, S. Perry, F. Bartoli, and S. Tatic-Lucic. 2009. Spectral characterization of the voltage-sensitive dye di-4-ANEPPDHQ applied to probing live primary and immortalized neurons. Optics Express 17:984-990.

45. Demchenko, A. P., Y. Mély, G. Duportail, and A. S. Klymchenko. 2009. Monitoring biophysical properties of lipid membranes by environment-sensitive fluorescent probes. Biophysical Journal 96:3461-3470.

46. Owen, D. M., P. M. P. Lanigan, C. Dunsby, I. Munro, D. Grant, M. A. A. Neil, P. M. W. French, and A. I. Magee. 2006. Fluorescence lifetime imaging provides enhanced contrast when imaging the phase-sensitive dye di-4-ANEPPDHQ in model membranes and live cells. Biophysical Journal 90:80-82.

47. Crans, D. C., B. Baruah, A. Ross, and N. E. Levinger. 2009. Impact of confinement and interfaces on coordination chemistry: Using oxovanadate reactions and proton transfer reactions as probes in reverse micelles. Coordination Chemistry Reviews Coordination Chemistry in Micelles 253:2178-2185.

48. Maitra, A. 1984. Determination of size parameters of water-Aerosol OT-oil reverse micelles from their nuclear magnetic resonance data. The Journal of Physical Chemistry 88:5122-5125.

49. Baruah, B., L. A. Swafford, D. C. Crans, and N. E. Levinger. 2008. Do probe molecules influence water in confinement? The Journal of Physical Chemistry B 112:10158-10164.

50. Karlsson, M., H. Thorn, A. Danielsson, K. G. Stenkula, A. Öst, J. Gustavsson, F. H. Nystrom, and P. Strålfors. 2004. Colocalization of insulin receptor and insulin receptor substrate-1 to caveolae in primary human adipocytes. European Journal of Biochemistry 271:2471-2479.

51. Pilch, P. F., P. A. Thompson, and M. P. Czech. 1980. Coordinate modulation of D-glucose transport activity and bilayer fluidity in plasma membranes derived from control and insulin-treated adipocytes. Proc Natl Acad Sci U S A 77:915–918.

52. Muller, S., S. Denet, H. Candiloros, R. Barrois, N. Wiernsperger, M. Donner, and P. Drouin. 1997. Action of metformin on erythrocyte membrane fluidity in vitro and in vivo. European Journal of Pharmacology 337:103-110.

53. Freisleben, H.-J., S. Ruckert, N. Wiernsperger, and G. Zimmer. 1992. The effects of glucose, insulin and metformin on the order parameters of isolated red cell membranes: An electron paramagnetic resonance spectroscopic study. Biochemical Pharmacology 43:1185-1194.

54. Matthaei, S., A. Hamann, H. H. Klein, H. Benecke, G. Kreymann, J. S. Flier, and H. Greten. 1991 Association of Metformin's effect to increase insulin-stimulated glucose transport with potentiation of insulin-induced translocation of glucose transporters from intracellular pool to plasma membrane in rat adipocytes. Diabetes 40 850-857

55. Hundal, H., T. Ramlal, R. Reyes, L. Leiter, and A. Klip. 1992. Cellular mechanism of metformin action involves glucose transporter translocation from an intracellular pool to the plasma membrane in L6 muscle cells. Endocrinology 131:1165-1173.

56. Pike, L. J., and J. M. Miller. 1998 Cholesterol depletion delocalizes phosphatidylinositol bisphosphate and inhibits hormone-stimulated phosphatidylinositol turnover. Journal of Biological Chemistry 273 22298-22304

57. Huby, R. D., R. J. Dearman, and I. Kimber. 1999. Intracellular phosphotyrosine induction by major histocompatibility complex class II requires co-aggregation with membrane rafts. J Biol Chem 274:22591-22596.

58. Sheets, E., D. Holowka, and B. Baird. 1999. Membrane organization in immunoglobulin E receptor signaling. Current Opinion in Chemical Biology 3:95-99.

59. Reis-Sobreiro, M., C. Gajate, and F. Mollinedo. 2009. Involvement of mitochondria and recruitment of Fas/CD95 signaling in lipid rafts in resveratrol-mediated antimyeloma and antileukemia actions. 28:3221-3234.

60. Janes, P., S. Ley, and A. Magee. 1999. Aggregation of lipid rafts accompanies signaling via the T cell antigen receptor. J Cell Biol 147:447-461.

61. Huby, R. D. J., R. J. Dearman, and I. Kimber. 1999 Intracellular phosphotyrosine induction by major histocompatibility complex class II requires co-aggregation with membrane rafts. Journal of Biological Chemistry 274: 22591-22596

Table 3.1: SPT measurements of gold-labeled IR on live RBL-2H3 cells before and after treatment with insulin or $Cr(pic)_3$[1].

Treatment	Diffusion Coefficient ($10^{-11}cm^2s^{-1}$)	Compartment Size (nm)[2]
Untreated	1.17±0.26	233±15
200 nM insulin (1hr)	0.44±0.43	111±11[a]
$Cr(pic)_3$ (overnight)	0.66±0.13	125±12[a]
$Cr(pic)_3$ (1hr)	0.41±0.12	89±9[a]
$Cr(pic)_3$, insulin (1hr)	0.39±0.08	96±7[a]

[1]Each reported value is the mean and SEM of measurements on 20 individual particles.
[2]Student's t-test ($p < 0.05$) indicates values with superscript a are significantly different compared to respective value measured on untreated cells.

Table 3.2: Percentages of total IR distributed in low-density and high density membrane fractions from RBL-2H3 cells following treatment with insulin, with $Cr(pic)_3$ or with both insulin and $Cr(pic)_3$.[1]

Fractions (sucrose %)	Untreated	Insulin	$Cr(pic)_3$[2]	Insulin, $Cr(pic)_3$[3]
Low density (<40%)	2±1	21±10 [a]	32±8[a]	48±3[b]
High density (>40%)	98±1	79±10 [a]	68±8[a]	52±1[b]

[1]Reported values are each the mean and SEM for at least 3 individual experiments.
[2]Values with the superscript a differ significantly from the value for untreated cells according to a paired t-test ($p<0.05$).
[3]Values with superscript b differ significantly from the value for untreated cells according to a paired t-test ($p<0.001$)

Table 3.3: Localization of pIR, pIRS-1 and pAKT in detergent resistant and bulk membrane fractions following treatment with with insulin, with $Cr(pic)_3$ or with both insulin and $Cr(pic)_3$.[1]

.

	Fractions (sucrose %)	Untreated	Insulin[2]	$Cr(pic)_3$	$Cr(pic)_3$, Insulin	MβCD[3]	MβCD/Insulin
pIR							
	Low density (<40%)	45±3	66±11	33±17	67±11	12±14[b]	45±13
	High density (>40%)	55±3	35±11	67±17	33±11	88±14	56±13
pIRS-1							
	Low density (<40%)	5±4	62±19[a]	58±29	N.A.	9±1	N.A.
	High density (>40%)	95±4	39±19[a]	43±29	N.A.	91±1	N.A.
pAKT							
	Low density (<40%)	25±12	58±13	60±7	N.A.	22±9	N.A.
	High density (>40%)	75±12	42±13	40±7	N.A.	78±9	N.A.

[1]Each reported value is the mean and SEM for at least 3 individual experiments.
[2]Values with the superscript a differ significantly from the value for untreated cells according to a paired t-test ($p<0.05$).
[3]Values with the superscript b differ significantly from the value for untreated cells according to a paired t-test ($p<0.001$).

Table 3.4: Absorbance peak wavelengths for the O-D stretch in reverse micelles and reverse micelles containing $Cr(pic)_3$ or picolinate ligand using background subtracted FTIR spectroscopy

w_o[1]	No probe (nm)	5mM $Cr(pic)_3$ (nm)[2]	100mM picolinate (nm)[2]
6	2552±1	2552±1 [0.03]	2553±1 [0.55]
10	2543±1	2543±1 [0.09]	2544±1 [1.1]
18	2528±1	2528±1 [0.43]	2528±1 [2.9]

[1] $w_o=[H_2O]/[AOT]$

[2] Square brackets indicate the average number of $Cr(pic)_3$ or picolinate molecules, respectively, present in each reverse micelle.

A)

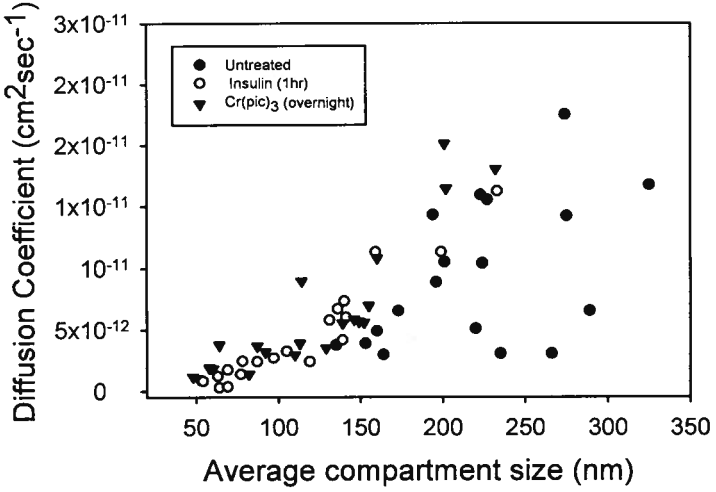
Diffusion Coefficient (cm^2sec^{-1})
3x10-11
2x10-11
2x10-11
1x10-11
10-11
5x10-12
0
Untreated
Insulin (1hr)
Cr(pic)3 (overnight)
50
100
150
200
250
300
350
Average compartment size (nm)

B)

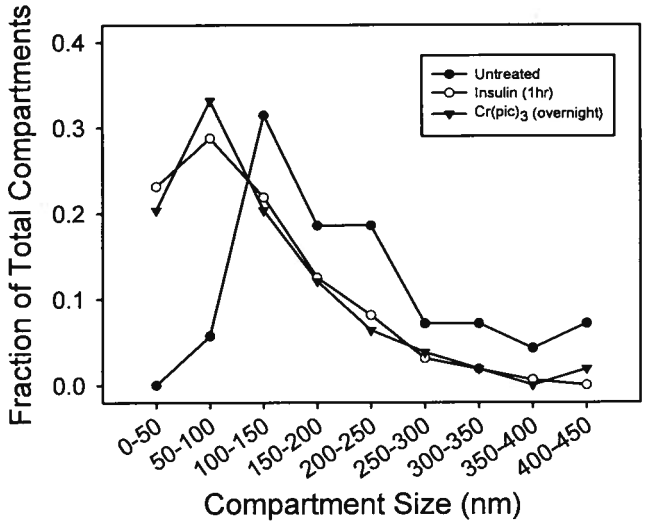
Fraction of Total Compartments
0.4
0.3
0.2
0.1
0.0
Untreated
Insulin (1hr)
Cr(pic)3 (overnight)
0-50
50-100
100-150
150-200
200-250
250-300
300-350
350-400
400-450
Compartment Size (nm)

Figure 3.1

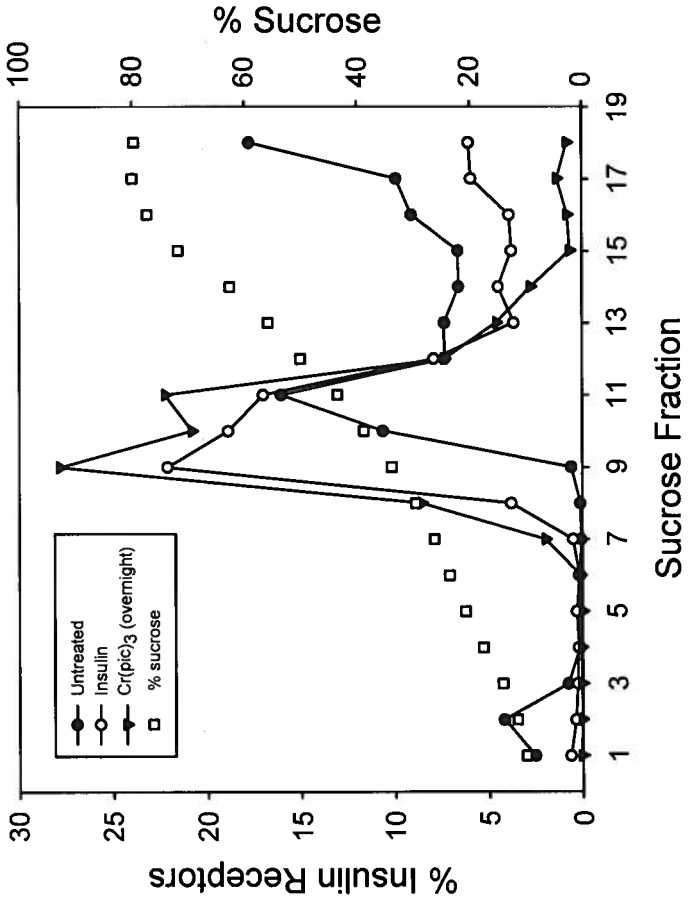
% Sucrose
100
80
60
40
20
0
% Insulin Receptors
30
25
20
15
10
5
0
1
3
5
7
9
11
13
15
17
19
Sucrose Fraction
Untreated
Insulin
Cr(pic)3 (overnight)
% sucrose

Figure 3.2

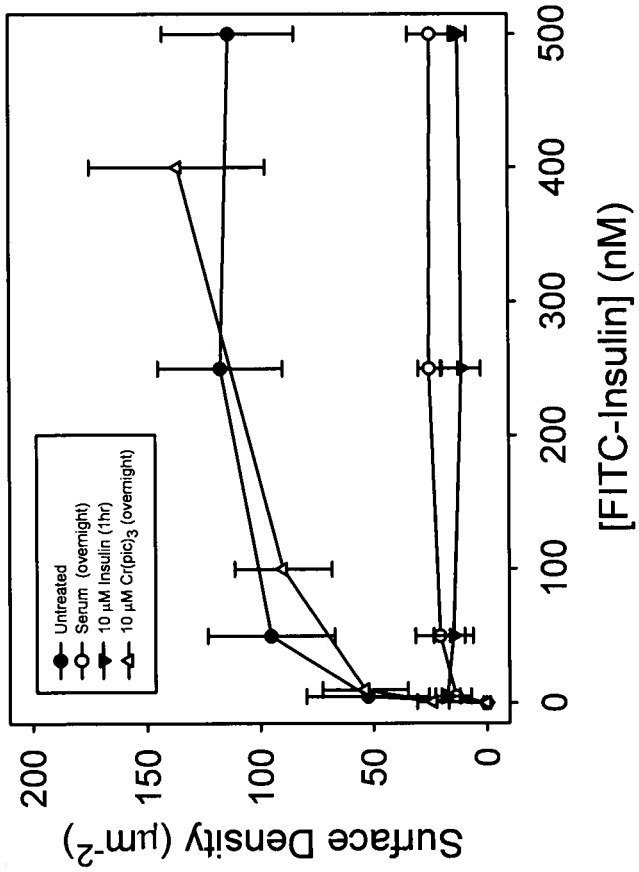
Surface Density (μm-2)
200
150
100
50
0
0
100
200
300
400
500
[FITC-Insulin] (nM)
Untreated
Serum (overnight)
10 μM Insulin (1hr)
10 μM Cr(pic)3 (overnight)

Figure 3.3

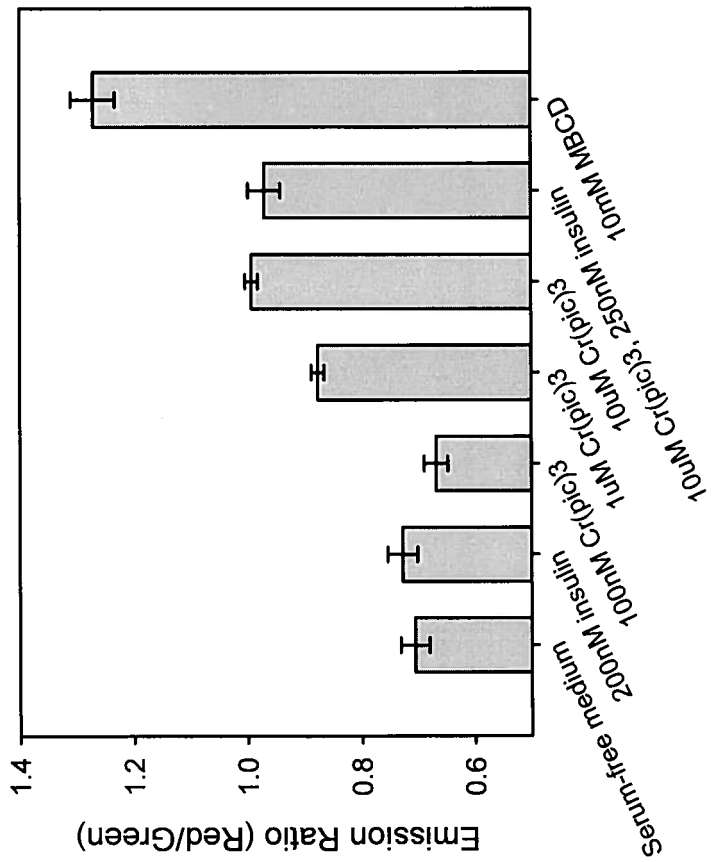
Emission Ratio (Red/Green)
1.4
1.2
1.0
0.8
0.6
Serum-free medium
200nM insulin
100nM Cr(pic)3
1uM Cr(pic)3
10uM Cr(pic)3
10nM Cr(pic)3, 250nM insulin
10um MBCD

Figure 3.4

Chapter IV: Peter W. Winter performed all experiments described herein.

Actin-Dependent Clustering of Insulin Receptors in Membrane Microdomains

Peter W. Winter[a], Alan K. Van Orden[b], Deborah A. Roess[a,c] and B. George Barisas[a,b]

[a]Cell and Molecular Biology Program, [b]Department of Chemistry, [c]Department of Biomedical Sciences Colorado State University, Fort Collins, Colorado 80523

Address all correspondence and requests for reprints to: Dr. B. George Barisas, Department of Chemistry Campus Mail 1872, Colorado State University, Fort Collins, CO 80523. Phone: (970) 491-6641; Fax: (970) 491-1801; Email: barisas@lamar.colostate.edu

Highlights

- Binding of ligand to insulin receptors on live cells is multivalent.
- Treatment with insulin restricts lateral motions of *individual* insulin receptors on live cells.
- Clustering of ligand-occupied insulin receptors *is* reduced by disrupting actin filaments.
- Clustering of ligand-occupied insulin receptors *is not* reduced by depleting membrane cholesterol.

Recent evidence suggests that, after binding of ligand, insulin receptors (IR) interact with specialized, cholesterol-containing, membrane microdomains and components of the actin cytoskeleton. Using single particle tracking techniques, we examined how binding of ligand, depletion of membrane cholesterol and disruption of actin filaments affect the lateral motions of individual quantum dot-labeled native IR on live rat basophilic leukemia 2H3 cells. We also examined the effects of similar treatments on IR clustering and multivalent binding of ligand on these cells using both photon counting histogram analysis and polarization homo-fluorescence resonance energy transfer imaging. Our analysis indicates that binding of ligand to IR on these cells is multivalent, involving at least two ligand molecules as labeling concentrations approach 1 μM. Binding of ligand also reduces lateral diffusion of individual IR and the size of IR-containing membrane compartments. However, while both IR lateral diffusion and the size of IR-containing compartments increase after disrupting actin filaments or depleting membrane cholesterol, clustering of ligand-occupied IR is reduced only by disrupting actin filaments or fixing cells prior to exposure to ligand and not by depleting membrane cholesterol. Thus, it appears that, although restriction of IR lateral motions on these cells is sensitive to both actin-filament dynamics and membrane cholesterol content, clustering of ligand-occupied IR primarily involves an actin-dependent mechanism.

Keywords: Insulin receptor, photon counting histogram analysis, single particle tracking, polarization homo-transfer FRET, membrane microdomain

1. Introduction

The insulin receptor (IR) is a well-characterized hetero-tetrameric transmembrane receptor, consisting of two extracellular α-subunits, containing multiple ligand-binding sites, and two largely intracellular β-subunits with both *auto*- and *trans*-tyrosine kinase activity [1-6].

Binding of ligand to IR α-subunits induces the phosphorylation of each β-subunit by the other, increasing the activity of both β-subunits and *in vitro* IR is known to exhibit complex allosteric ligand-binding properties [2-4].

Previous work by our group demonstrates that insulin treatment increases association of native IR and downstream substrates with detergent-resistant membrane microdomains on 2H3 rat basophilic leukemia (RBL-2H3) cells [7]. Similar results obtained by other investigators also indicate that, in adipocytes, IR preferentially associate with cholesterol-containing membrane microdomains [8-13] and that, in muscle cells, insulin treatment induces substantial reorganization of sub-surface actin filaments [14]. It has also been suggested that, in some cell types, components of the actin cytoskeleton anchor IR in specialized, cholesterol-containing, membrane microdomains such as caveolae [15]. However, the nature of these interactions and how they affect both lateral motions of IR and IR self-association, *i.e.* clustering, is not yet adequately characterized at the single-molecule level.

RBL-2H3 cells are well-characterized with respect to activation of the Type I IgE receptor (FcεRI) by antigen crosslinking and, similar to results observed for IR on other cell lines, activation of FcεRI on these cells results in increased association of FcεRI with specialized, cholesterol-containing, membrane microdomains [25-27]. Additionally, both restriction of individual FcεRI lateral motions and clustering of crosslinked FcεRI on these cells has also been shown to involve interactions with sub-surface actin-filaments [25].

In the present work, we utilize single particle tracking (SPT) [16-19] to monitor the lateral motions of individual quantum dot-labeled IR diffusing on the surface of viable RBL-2H3 cells. We also utilize both photon counting histogram analysis (PCH) [20, 21] and polarization homo-fluorescence resonance energy transfer (homoFRET) imaging [22-24] to investigate multivalent binding of ligand and clustering of ligand-occupied IR on these cells. We define a

cluster as a group of receptors that diffuse together or are within homoFRET distance. However, this does not necessarily imply increased physical crosslinking of such receptors.

Our results indicate that at least two separate FITC-insulin molecules can bind to individual IR on the surface of live RBL-2H3 cells as labeling concentrations approach 1 μM, leading to increased restriction of individual IR lateral diffusion and a reduction in the size of IR-containing membrane compartments. We also demonstrate that clustering of ligand-occupied IR on these cells is reduced by disrupting actin-filaments and by fixing cells with paraformaldehyde prior to labeling. Finally, we show that, while depletion of cholesterol from cell membranes does not affect IR clustering, it does increase cell-surface IR lateral and rotational diffusion. Taken together, our results suggest that, although clustering of ligand-occupied IR appears to depend primarily on actin-filament dynamics, at least a portion of these receptors occupy nanometer-scale, cholesterol-containing, membrane microdomains.

2. Materials and Methods

2.1 *Materials*

RBL-2H3 cells were purchased from ATCC (Manassas, VA). Insulin, methyl-β-cyclodextran (MβCD), paraformaldehyde, cytochalasin D and bovine serum albumin (BSA) were purchased from Sigma-Aldrich Inc. (St. Louis, MO). Anti-insulin receptor-β-biotin (C-19) IgG was purchased from Santa Cruz Biotech (Santa Cruz, CA). FITC-insulin and Qdot605 streptavidin-conjugated quantum dots, were purchased from Invitrogen (Carlsbad, CA). Rhodamine 6G (R6G) was purchased from Allied Chemical (Vadodara, Gujarat, India). Modified essential medium (MEM) was purchased from Cellgro (Manassas, VA). Fetal bovine serum (FBS) and fungizone were purchased from Gemini (Sacramento, CA). Sodium fluorescein was purchased from Merck (Whitehouse Station, NJ).

2.2 Sample preparation

For SPT, PCH and homoFRET experiments RBL-2H3 cells were seeded onto sterile #1.5 glass bottom culture dishes, grown to approximately 50% confluence and, unless otherwise indicated, incubated in medium without FBS for a minimum of 12 hr before use to remove a source of exogenous insulin and other hormones. In some experiments cells were treated with either 40 μg/mL cytochalasin D or 10 mM MβCD, or both cyotchalasin D or MβCD for 1 hr at 37 C before labeling.

2.3 PCH of FITC-insulin labeled insulin receptors

In FITC-insulin equilibrium binding experiments, cells were incubated in 0.01 nM - 1 μM FITC-insulin for 30 min, followed by 4 washes. In competition binding experiments between FITC-insulin and insulin, cells were simultaneously incubated in buffer solutions containing 50 nM FITC-insulin and increasing amounts of insulin for 30 min then washed 4 times. To measure FITC-insulin dissociation, cells were labeled with 10 nM FITC-insulin for 30 min, washed 4 times and then examined at the times indicated. To investigate the effects of aqueous insulin on FITC-insulin dissociation, cells were labeled with 250 nM FITC-insulin for 30 min, washed 3 times for 30 sec in 1 mL of buffer and then incubated in 0.025 nM - 25 μM insulin for 30 min and washed 3 times.

PCH experiments were performed using a modified Nikon TE1000 inverted microscope equipped with a 100x, 1.25 NA, oil-immersion objective, an Omnichrome Melles-Griot multi-line air-cooled argon ion laser, two PerkinElmer single photon counting modules (SPCM-AQR-14), an ALV-6010 digital hardware correlator and a Becker and Hickl GmbH PMS-400 multichannel correlator as previously described [28]. Based on FCS measurements of aqueous R6G diffusion, the $1/e^2$ radius of the laser excitation beam at the sample in our system was determined to be 241 nm (data not shown). In live cell studies, the laser was focused on the apical cell membrane to maximize detector count rates and minimize diffusional correlation times as described by Ries

and Schwille [29]. Samples were illuminated for approximately 10 sec before collection of data to allow for the irreversible photobleaching of immobile particles [30]. Data were then collected for 30 sec during which time the average fluorescence from the sample was relatively uniform as indicated by the avalanche photodiode signal readouts (data not shown). For PCH, detected photons were accumulated into successive 1 μs counting channels and then rebinned into 9 μs channels to improve signal-to-noise. Accumulated photon counts were then simultaneously subjected to autocorrelation, pseudo-crosscorrelation and PCH. Weighted least-squares fitting was used to obtain estimates of the average number of particles in the interrogation volume (*N)*, the detected photon counts per molecule per sampling time (ε) and the out-of-focus emission ratio (*F*) as previously described [21, 31, 32]. Each PCH value presented, except those in Supplement 2, represents the result of measurements on 8-10 individual RBL-2H3 cells. Each PCH values presented in Supplement 2 represents a single measurement from an individual cell.

2.4 Single particle tracking of individual insulin receptors

Fluorescent quantum dots were used to track the lateral motions of individual IR on the surface of live RBL-2H3 cells. Briefly, viable RBL-2H3 cells were labeled using a slight modification of a protocol that minimizes receptor crosslinking [16]. Cells were first labeled with anti-IR-β-biotin IgG at 0.1 μg/mL for 30-40 min, washed 3 times for 1 min in 1 mL of buffer, labeled with 100 pM Qdot605 streptavidin-conjugated quantum dots for 10 min and then washed 6 times for 1 min in 1 mL of buffer before imaging. Wide-field fluorescence images were then collected from the apical surface of live cells using a Zeiss Axiovert 200M microscope equipped with a 63x 1.2 NA apochromatic water-immersion objective and custom filter sets (Chroma Technology; Bellow Falls, VT). Images were collected every 33 ms for up to 3 minutes at a total magnification of 315x with an Andor Ixon EM+ camera resulting in a final pixel size of approximately 50 nm. This was achieved using a Zeiss 2.5x Optovar and a C-mount 2x magnifying lens placed in front of the camera. Image acquisition and determination of individual

particle locations were performed with MetaMorph 7.1.6 (Molecular Devices; Sunnyvale, CA). Macroscopic lateral diffusion rates and compartment diagonals were determined using custom analysis programs. Blinking of individual IR-bound quantum dot particles, while apparent, did not prevent tracking over long periods of time. The trajectories of individual particles were segmented into compartments by calculation of statistical variance in particle position over time [17, 19, 27] producing variance plots that exhibited peaks at inter-compartment boundaries. These results were analyzed to yield the compartment size and residence time for each particle. Effective macroscopic diffusion was calculated as the square of the compartment diagonal divided by four times the residence time in the compartment as previously described [33]. SPT values shown each reflects measurements of 30-100 total particles on 10-20 individual RBL-2H3 cells.

2.5 HomoFRET imaging of FITC-insulin labeled insulin receptors

We used homoFRET methods similar to those previously described [34] to examine multivalent ligand binding and clustering of ligand-occupied IR. Data were acquired on individual, FITC-insulin labeled RBL-2H3 cells using an Olympus IX-71 microscope equipped with a FV300 confocal scanning unit, a 60x, 1.2NA apochromatic water-immersion objective, and a polarizing beam splitter to allow simultaneous collection of parallel and perpendicular fluorescence. FITC-insulin was excited with the 488 nm line of an argon ion laser and appropriate barrier and dichroic filters were selected for fluorescence emission. Individual cells emitting ring-like fluorescence from FITC-insulin labeling at the plasma membrane were selected for imaging. Sequences of 30 cell images where then obtained as probe molecules were photobleached to approximately 10% of their initial average intensity. Image analysis was performed using custom data analysis programs. Total intensity (s) and fluorescence anisotropy (r) were calculated as $s=I_{\parallel} + 2I_{\perp}$ and $r=(I_{\parallel} - I_{\perp})/s$, where $I_{\parallel}$ and $I_{\perp}$ are fluorescence emission polarized parallel and perpendicular, respectively, to the polarization of excitation light [22, 35].

FRET efficiencies (E) were estimated from average initial and final r values using the following formula: $E=(1 - r_{initial}/r_{final}) \times 100\%$ [36]. The variance in change in r (Δr) values between individual cells was less than the variance of corresponding initial and final r values. This is due to irreproducibility in optical positioning that contributes to uncertainty in both $r_{initial}$ and r_{final}, but not Δr. HomoFRET values shown each represent the result of measurements on 25-30 individual RBL-2H3 cells.

2.6 Presentation of Results

All values presented except those in Table 3 are the mean ± SD. Values presented in Table 3 are the mean ± SEM.

3. Results

3.1 PCH of aqueous fluorophores

(Insert Figure 4.1)

PCH provides a probability distribution for the number of detected photons observed during a specified counting interval and depends on the average photodetection rate for each fluorescing species in the system[20, 21, 32]. For each fluorescing species present, PCH is able to determine both molecular brightness (ε) and the effective number of particles residing in the interrogation volume (*N*) [37-40]. We utilized PCH to compare the ε of aqueous fluorescein and FITC-insulin (Figure 4.1). Our results demonstrate that the ε of both fluorescein and FITC-insulin were similar at 0.13±0.01 kHz and that, in solution, the ε of FITC-insulin was constant over a 100-fold (1-100 nM) concentration range (data not shown).

3.2 PCH of FITC-insulin bound to insulin receptors on live-cells

(Insert Table 4.1)

(Insert Table 4.2)

We next utilized PCH to examine the ε of IR-bound FITC-insulin molecules on viable RBL-2H3 cells. The increased ε of FITC-insulin molecules when bound to IR diffusing on the surface of these cells relative to when diffusing in solution suggests that either IR separately bind at least two ligand molecules as labeling concentrations approach 1 μM or that binding of ligand induces substantial clustering of cell-surface IR. Equilibrium binding of 10 pM - 1 μM FITC-insulin shows that as *N* increased, the ε of detected particles also increased from 0.14±0.01 kHz to 0.31±0.07 kHz (Figure 4.1, Table 4.1 and Supplement 4.1). Treatment of cells with cytochalasin D or MβCD before labeling with 1 μM FITC-insulin slightly lowered the ε of detected particles to 0.27±0.06 kHz and 0.29±0.04 kHz, respectively, suggesting that the increase in ε of FITC-insulin when bound to IR may, in addition to, multivalent binding of ligand also reflect clustering of a portion of cell-surface IR via an actin-mediated or cholesterol-dependent mechanism. PCH monitoring the dissociation of FITC-insulin from cells over a 2 hr period indicates that the ε of detected particles on cells labeled with 10 nM FITC-insulin decreased from approximately 0.18 kHz to 0.14 kHz as *N* decreased (Supplement 4.2) and the ε of detected particles also decreased from 0.26±0.05 kHz to 0.19±0.06 kHz in cells that were labeled with 250 nM FITC-insulin for 30 min and then incubated in either 50 pM or 50 μM insulin, respectively, for 30 min before observation. Finally, competition binding of 50 nM FITC-insulin and 25 pM - 25 μM insulin to live cells indicates that the ε of cell-bound FITC-insulin decreased from 0.25±0.04 kHz to 0.17±0.02 kHz as *N* decreased (Table 4.2). Combined, these results indicate that, changes in *N* are mirrored by changes in ε which is consistent with both multivalent binding of FITC-insulin to IR and ligand-induced clustering of IR.

3.3 Lateral diffusion of individual cell-surface insulin receptors

(Insert Figure 4.2)

(Insert Table 4.3)

PCH results indicate that treatment with 50 nM or greater concentrations of insulin results in the occupancy of at least 75% of insulin binding sites on viable RBL-2H3 cells (Table 4.1 and Supplement 4.1). With this in mind, we examined the lateral motions of IR on the surface of live RBL-2H3 cells before and after treatment with both 50 nM and 250 nM insulin (Figure 4.2 and Table 4.3). When anti-IRβ-biotin IgG and streptavidin-conjugated quantum dots were used to track the movement of individual IR on serum-starved cells the average macroscopic lateral diffusion coefficient was approximately $1x10^{-10}cm^2s^{-1}$, after treatment with insulin this was reduced to approximately $3x10^{-11}cm^2s^{-1}$ (Figure 4.2 and Table 4.3). The average size of compartments accessed by IR was also reduced from approximately 475 nm in serum-starved cells to approximately 250 nm after insulin treatment (Figure 4.2 and Table 4.3). Treatment of cells with either 40 μg/mL cytochalasin D, or 10 mM MβCD for 1 hr increased IR lateral diffusion to approximately $2x10^{-9}cm^2s^{-1}$ and $1x10^{-9}cm^2s^{-1}$, respectively (Table 4.3) and the size of IR-containing membrane compartments to approximately 1 μm and 600 nm, respectively. The increases in IR lateral diffusion and compartment size were almost two-fold greater after disrupting actin filaments than after depleting membrane cholesterol content, suggesting that restriction of individual cell-surface IR lateral motions is regulated differentially by cholesterol-containing membrane structures and actin filament-delineated membrane compartments.

3.4 HomoFRET imaging of FITC-insulin-occupied cell-surface insulin receptors

(Insert Figure 4.3)

(Insert Table 4.4)

We next examined both multivalent binding of ligand and ligand-induced clustering of IR using homoFRET imaging. Similar to PCH, homoFRET is useful for monitoring the colocalization of biological molecules on the macromolecular scale (~10nm) [22-24], and can yield information on multivalent ligand binding and receptor clustering [34]. HomoFRET between neighboring, fluorescent molecules is easily observed by monitoring changes in the

anisotropy of fluorescence emission as probe molecules are progressively photobleached [24, 34]. Analysis of FITC-insulin labeled IR on live, otherwise untreated, RBL-2H3 cells indicates that the initial r of receptor bound FITC-insulin is 0.13±0.02 and increases 0.06±0.01 as probe molecules are bleached to approximately 10% of their original intensity (Figure 4.3, Table 4.4, Supplement 4.3). Using the method originally developed by Yao and Major [36] we calculate that the E of FITC-insulin molecules bound to these cells is 32%. Extraction of membrane cholesterol from cells using MβCD decreased the initial r of FITC-insulin labeled IR to 0.10±0.02 and decreased the total change in r as probe molecules were bleached to 0.05±0.01. However, the E of FITC-insulin labeled IR on these cells was nearly identical to the E of cells that were untreated before labeling with FITC-insulin (Table 4.4, Supplement 4.3). Disruption of actin filaments using cytochalasin D decreased the total change in r as probe molecules were bleached to 0.04±0.01 and decreased the E of FITC-insulin labeled IR to 21%, but did not reduce initial r of FITC-insulin labeled IR (Table 4.4, Supplement 4.3). Simultaneous treatment of cells with MβCD and cytochalasin D reduced both the final r of labeled receptors to 0.15±0.02 and reduced the observed efficiency of homoFRET to 20%. Finally, homoFRET analysis of cells fixed in 4% paraformaldehyde for 40 min at 37 C before FITC-insulin labeling of IR shows that the while the initial and final r of IR bound FITC-insulin slightly increased, the total change in r during bleaching of probe molecules decreased to 0.04±0.01 resulting in an E of 25% (Table 4.4, Supplement 4.3). Fixing cells with paraformaldehyde before labeling presumably reduces ligand-induced changes in cell-surface IR distribution that would otherwise result from exposure to FITC-insulin [41]. This suggests that, in addition to homoFRET resulting from multivalent binding of ligand, at least a portion of the homoFRET between IR-bound FITC-insulin molecules on live, otherwise untreated, cells is due to ligand-induced clustering of IR not seen in cells fixed with paraformaldehyde or treated with cytochalasin D before labeling.

4. Discussion

How hierarchical organization of the plasma membrane affects both lateral motions and spatial distribution of transmembrane protein receptors is of considerable interest [11, 13-15, 42, 43]. Therefore, we examined how the interaction of a transmembrane receptor such as IR with cholesterol-containing membrane structures and actin filament-delineated membrane compartments affected both clustering and lateral motions of IR using a variety of fluorescence-based biophysical techniques.

A growing body of evidence suggests that several types of membrane structures and microdomains serve as platforms for IR signaling [11-13, 44-48] and that components of the actin cytoskeleton anchor IR in microdomains such as caveolae [15]. However, the effects of both membrane cholesterol depletion and disruption of actin-filament dynamics on clustering of ligand-occupied IR and the restriction of individual IR lateral motions have not been adequately described at the single molecule level.

PCH of FITC-insulin binding to native IR on live RBL-2H3 cells suggests that IR ligand-binding is multivalent and likely involves at least two FITC-insulin molecules as labeling concentrations approach 1 μM. Multivalent binding is evident when comparing the ε of FITC-insulin, when in solution, and when bound to IR on the surface of RBL-2H3 cells. Results of competition binding between FITC-insulin and unlabeled insulin, as well as FITC-insulin dissociation also suggest multivalent ligand-binding. It is also possible that the shift in ε observed as FITC-insulin molecules bind to live RBL-2H3 cells is the result of ligand-induced physical crosslinking of multiple IR, however there is significant evidence, both *in vitro* and in live cells, indicating this does not occur [1-4].

Single particle tracking studies of IR lateral diffusion on live cells showed that, before insulin treatment, individual IR exhibit pseudo-random lateral diffusion within relatively large membrane microdomains. After exposure to insulin, individual IR largely become confined

within 100nm-400nm scale microdomains and exhibit significantly reduced lateral diffusion. Although SPT studies cannot conclusively determine the mechanisms behind this ligand-induced restriction of IR lateral motion, they suggest that both actin-filament dynamics and membrane cholesterol content regulate IR lateral motions on RBL-2H3 cells. These results also seem to support previous investigations which indicate that the plasma membrane contains hierarchically-organized lipid and protein-delineated compartments [17, 42, 49, 50].

Results of homoFRET imaging of FITC-insulin labeled IR on live cells, and on cells fixed with paraformaldehyde before labeling, demonstrate that ligand binding induces a measurable degree of IR clustering. These results also indicate that FITC-insulin binding to IR is either multivalent or that a portion of IR on these cells are clustered *before* exposure to ligand. Additionally, the reduction in homoFRET efficiency relative to untreated cells when samples were treated with cytochalasin D, but not when treated with MβCD before labeling, suggests that ligand-induced clustering of IR on RBL-2H3 cells involves an actin-dependent mechanism and is not directly tied to membrane cholesterol content. This is interesting in light of prior evidence indicating that binding of ligand causes preferential association of IR with a variety of cholesterol-containing membrane microdomains [8-10] and of literature describing increased clustering of cell-surface EGFR after depleting membrane cholesterol [37]. Although it should be noted that while not affecting clustering of ligand-occupied IR, depleting membrane cholesterol did reduce the apparent initial anisotropy of FITC-insulin labeled IR.

Taken together, our results indicate that native IR on live RBL-2H3 cells bind at least two FITC-insulin molecules at labeling concentrations approaching 1 μM and that binding of ligand to these cells results in significant restriction of individual IR lateral motions. Our results also indicate that clustering of ligand-occupied IR on these cells involves an actin-dependent mechanism and does not depend on retention of IR within cholesterol-containing membrane microdomains.

5. Acknowledgements

We would like to thank Dr. Jaemyong Jung for writing PCH data acquisition and analysis software. We would also like to thank Dr. Jeffrey T. McPhee and Jonathan Gerding for assistance with acquisition of PCH data. This work was supported by the NSF (CHE0628260, MCB1024668) and the American Heart Association (AHA0650081Z).

Figure Legends

Figure 1: Representative PCH of fluorescein derived fluorescent probes in solution and on viable RBL-2H3 cells. A) 20 nM fluorescein (solution); ε 0.13, *N* 18.1, *F* 0.7, reduced χ^2 2.3, B) 10 nM FITC-insulin (solution); ε 0.11, *N* 12.7, *F* 0.7, reduced χ^2 0.15, C) 10 pM FITC-insulin (live-cells); ε 0.13, *N* 3.2, *F* 0.7, reduced χ^2 1.1, D) 1 μM FITC-insulin (live-cells); ε 0.3, *N* 26.7, *F* 0.7, reduced χ^2 1.2.

Figure 2: A) Representative trajectories of quantum dot-labeled IR from a serum-starved RBL-2H3 cell and a cell treated with 250 nM insulin. B) Average lateral diffusion vs. average compartment diagonal for individual quantum dot labeled IR on serum starved cells or cells treated with 250 nM insulin.

Figure 3: Representative graph illustrating the change in anisotropy (○) and total fluorescence intensity (●) of IR-bound FITC-insulin molecules during the acquisition of 30 sequential images on a RBL-2H3 cell that was untreated before labeling with FITC-insulin.

References

[1] L. Chang, S.-H. Chiang and A.R. Saltiel, Insulin signaling and the regulation of glucose transport Mol. Med. 10 (2004) 65-71.

[2] P. De Meyts and J. Whittaker, Structural biology of insulin and IGF1 receptors: implications for drug design Nature Reviews, Drug Discovery 1 (2002).

[3] L. Gauguin, B. Klaproth, W. Sajid, A.S. Andersen, K.A. McNeil, B.E. Forbes and P. De Meyts, Structural basis for the lower affinity of the insulin-like growth factors for the insulin receptor Journal of Biological Chemistry 283 (2008) 2604-2613

[4] V.V. Kiselyov, S. Versteyhe, L. Gauguin and P. De Meyts, Harmonic oscillator model of the insulin and IGF1 receptors/' allosteric binding and activation 5 (2009).

[5] R.T. Watson, M. Kanzaki and J.E. Pessin, Regulated membrane trafficking of the insulin-responsive glucose transporter 4 in adipocytes Endocr Rev 25 (2004) 177-204.

[6] A. Saltiel and J. Pessin, Insulin signaling in microdomains of the plasma membrane Traffic 4 (2003) 711-716.

[7] D.A. Roess, S.M.L. Smith, P. Winter, J. Zhou, P. Dou, B. Baruah, A.M. Trujillo, N.E. Levinger, X. Yang, B.G. Barisas and D.C. Crans, Effects of vanadium-containing compounds on membrane lipids and on microdomains used in receptor-mediated signaling Chemistry & Biodiversity 5 (2008) 1558-1570.

[8] S. Parpal, M. Karlsson, H. Thorn and P. Stralfors, Cholesterol depletion disrupts caveolae and insulin receptor signaling for metabolic control via insulin receptor substrate-1, but not for mitogen-activated protein kinase control Journal of Biological Chemistry 276 (2001) 9670-9678.

[9] J. Gustavsson, S. Parpal, M. Karlsson, C. Ramsing, H. Thorn, M. Borg, M. Lindrot, K.H. Peterson, K.E. Magnusson and P. Stralfors, Localization of the insulin receptor in caveolae of adipocyte plasma membrane The FASEB Journal 13 (1999) 1961-1971

[10] A. Kimura, S. Mora, S. Shigematsu, J.E. Pessin and A.R. Saltiel, The insulin receptor catalyzes the tyrosine phosphorylation of caveolin-1 Journal of Biological Chemistry 277 (2002) 30153-30158

[11] J. Inokuchi, Membrane microdomains and insulin resistance FEBS Letters 584 (2010) 1864-1871.

[12] S. Vainio, S. Heino, J.-E. Mansson, P. Fredman, E. Kuismanen, O. Vaarala and E. Ikonen, Dynamic association of human insulin receptor with lipid rafts in cells lacking caveolae EMBO Reports 31 (2002) 95-100.

[13] J. Sánchez-Wandelmer, A. Dávalos, E. Herrera, M. Giera, S. Cano, G. de la Peña, M.A. Lasunción and R. Busto, Inhibition of cholesterol biosynthesis disrupts lipid raft/caveolae and affects insulin receptor activation in 3T3-L1 preadipocytes Biochimica et Biophysica Acta (BBA) - Biomembranes 1788 (2009) 1731-1739.

[14] T.T. Chiu, N. Patel, A.E. Shaw, J.R. Bamburg and A. Klip, Arp2/3- and cofilin-coordinated actin dynamics Is required for insulin-mediated GLUT4 translocation to the surface of muscle cells Mol. Biol. Cell (2010) E10-04-0316.

[15] M. Foti, G.v. Porcheron, M. Fournier, C. Maeder and J.-L. Carpentier, The neck of caveolae is a distinct plasma membrane subdomain that concentrates insulin receptors in 3T3-L1 adipocytes Proceedings of the National Academy of Sciences 104 (2007) 1242-1247

[16] D.S. Lidke, P. Nagy, R. Heintzmann, D. Arndt-Jovin, J. Post, H. Grecco, E. Jares-Erijman and T. Jovin, Quantum dot ligands provide new insights into erbB/HER receptor-mediated signal transduction Nature Biotechnology 22 (2004) 198-203.

[17] K. Murase, T. Fujiwara, Y. Umemura, K. Suzuki, R. Iino, H. Yamashita, M. Saito, H. Murakoshi, K. Ritchie and A. Kusumi, Ultrafine membrane compartments for molecular diffusion as revealed by single molecule techniques Biophys J 86 (2004) 4075-4093.

[18] Y. Sako and A. Kusumi, Compartmentalized structure of the plasma membrane for receptor movements as revealed by a nanometer-level motion analysis Journal of Cell Biology. 125 (1994) 1251-1264.

[19] F. Daumas, N. Destainville, C. Millot, A. Lopez, D. Dean and L. Salomé, Confined diffusion without fences of a G protein coupled receptor as revealed by single particle tracking Biophysical Journal 84 (2003) 356-366.

[20] Y. Chen, J. Muller, P. So and E. Gratton, The photon counting histogram in fluorescence fluctuation spectroscopy Biophysical Journal 77 (1999) 553-567.

[21] T. Perroud, B. Huang, M.I. Wallace and R. Zare, Photon counting histogram for one-photon excitation Chem Phys Chem 4 (2003) 1121-1123.

[22] D. Lidke, P. Nagy, B. Barisas, R. Heintzmann, J. Post, K. Lidke, A. Clayton, D. Arndt-Jovin and T. Jovin, Imaging molecular interactions in cells by dynamic and static fluorescence anisotropy (rFLIM and emFRET) Biochemical Society Transactions 31 (2003) 1020-1027.

[23] E. Jares-Erijman and T. Jovin, FRET imaging Nature Biotechnology 21 (2003) 1387-1395.

[24] L.W. Runnels and S.F. Scarlata, Theory and application of fluorescence homotransfer to melittin oligomerization Biophysical Journal 69 (1995) 1569-1583.

[25] N. Andrews, K. Lidke, J. Pfeiffer, A. Burns, B. Wilson, J. Oliver and D. Lidke, Actin restricts FceRI diffusion and facilitates antigen-induced receptor immobilization Nature Cell Biology 10 (2008) 955-963.

[26] N.L. Andrews, J.R. Pfeiffer, A.M. Martinez, D.M. Haaland, R.W. Davis, T. Kawakami, J.M. Oliver, B.S. Wilson and D.S. Lidke, Small, mobile FcεRI receptor aggregates are signaling competent Immunity 31 (2009) 469-479.

[27] B.G. Barisas, S. Smith, J. Liu, J. Song, G. Hagen, I. Pecht and D. Roess, Compartmentalization of the Type I Fc epsilon receptor and MAFA on 2H3 cell membranes Biophysical Chemistry 126 (2006) 209-217.

[28] K. Fogarty, J. McPhee, E. Scott and A. Van Orden, Probing the ionic atmosphere of single-stranded DNA using continuous flow capillary electrophoresis and fluorescence correlation spectroscopy Anal. Chem. 81: (2009) 465-472.

[29] J. Ries and P. Schwille, New concepts for fluorescence correlation spectroscopy on membranes Physical Chemistry 10 (2008) 3487-3497.

[30] S. Chiantia, J. Ries and P. Schwille, Fluorescence correlation spectroscopy in membrane structure elucidation Biochimica et Biophysica Acta 1788 (2009) 225-233.

[31] J. Jung and V.O. A, A three-state mechanism for DNA hairpin folding characterized by multiparameter fluorescence fluctuation spectroscopy J. Am.Chem. Soc. 128 (2006) 1240-1249.

[32] J. Jung, R. Ihly, E. Scott, M. Yu and A. Van Orden, Probing the complete folding trajectory of a DNA hairpin using dual beam fluorescence correlation spectroscopy J. Phys. Chem. 112 (2008) 127-133.

[33] M.J. Saxton, Single-particle tracking: the distribution of diffusion coefficients Biophys J 72 (1997) 1744-1753.

[34] A.N. Bader, S. Hoetzl, E.G. Hofman, J. Voortman, P.M.P. van Bergen en Henegouwen, G. van Meer and H.C. Gerritsen, Homo-FRET imaging as a tool to quantify protein and lipid clustering ChemPhysChem (2010) n/a.

[35] R. Varma and S. Mayor, GPI-anchored proteins are organized in submicron domains at the cell surface Nature 394 (1998) 798-801.

[36] M. Rao and S. Mayor, Use of Forster's resonance energy transfer microscopy to study lipid rafts Biochim Biophys Acta 1746 (2005) 221-233.

[37] S. Saffarian, U. Li, E. Elson and L. Pike, Oligomerization of the EGF receptor investigated by life cell fluorescence intensity distribution analysis Biophysical Journal 93 (2007) 1021-1031.

[38] Y. Chen, L.-N. Wei and J.D. MÃ¼ller, Probing protein oligomerization in living cells with fluorescence fluctuation spectroscopy Proceedings of the National Academy of Sciences of the United States of America 100 (2003) 15492-15497

[39] Y. Chen, L.-N. Wei and J.D. Müller, Unraveling protein-protein interactions in living cells with fluorescence fluctuation brightness analysis Biophysical Journal 88 (2005) 4366-4377.

[40] A.G. Godin, S. Costantino, L.-E. Lorenzo, J.L. Swift, M. Sergeev, A. Ribeiro-da-Silva, Y. De Koninck and P.W. Wiseman, Revealing protein oligomerization and densities in

situ using spatial intensity distribution analysis Proceedings of the National Academy of Sciences 108 (2011) 7010-7015

[41] K.A.K. Tanaka, K.G.N. Suzuki, Y.M. Shirai, S.T. Shibutani, M.S.H. Miyahara, H. Tsuboi, M. Yahara, A. Yoshimura, S. Mayor, T.K. Fujiwara and A. Kusumi, Membrane molecules mobile even after chemical fixation 7 (2010) 865-866.

[42] A. Kusumi, Y.M. Shirai, I. Koyama-Honda, K.G.N. Suzuki and T.K. Fujiwara, Hierarchical organization of the plasma membrane: Investigations by single-molecule tracking vs. fluorescence correlation spectroscopy FEBS Letters Frontiers in Membrane Biochemistry 584 (2010) 1814-1823.

[43] L.J. Pike, Rafts defined: a report on the Keystone symposium on lipid rafts and cell functionJ. Lipid Res. 47 (2006) 1597-1598.

[44] E. Sheets, D. Holowka and B. Baird, Membrane organization in immunoglobulin E receptor signaling Current Opinion in Chemical Biology 3 (1999) 95-99.

[45] R.D. Huby, R.J. Dearman and I. Kimber, Intracellular phosphotyrosine induction by major histocompatibility complex class II requires co-aggregation with membrane rafts J Biol Chem 274 (1999) 22591-6.

[46] P. Oh and J.E. Schnitzer, Segregation of heterotrimeric G proteins in cell surface microdomains Molecular Biology of the Cell 12 (2001) 685-698.

[47] C.L. Manahan, M. Patnana, K.J. Blumer and M.E. Linder, Dual lipid modification motifs in Ga and Gg subunits are required for full activity of the pheromone response pathway in *Saccharomyces cerevisiae* Mol Biol Cell 11 (2000) 957-68.

[48] A. Viola, R.L. Contento and B. Molon. in Immunological Synapse (Saito, T. and Batista, F.D., eds.), Vol. 340, pp. 109-122, Springer Berlin Heidelberg 2010.

[49] C. Dietrich, B. Yang, T. Fujiwara, A. Kusumi and K. Jacobson, Relationship of lipid rafts to transient confinement zones detected by single particle tracking Biophys J 82 (2002) 274-84.

[50] K. Ritchie, R. Iino, T. Fujiwara, K. Murase and A. Kusumi, The fence and picket structure of the plasma membrane of live cells as revealed by single molecule techniques (review) Molecular Membrane Biology 20 (2003) 13-18.

Table 4.1: PCH of equilibrium binding of FITC-insulin to individual RBL-2H3 cells.

FITC-insulin (nM)	***N***	**ε (kHz)[1]**
0.01	3.4±1.0	0.14±0.01
0.1	4.8±1.7	0.15±0.01
1.0	7.9±3.2	0.17±0.02
10	8.9±3.2	0.20±0.04
25	15.3±3.1	0.24±0.03
250	19.8±3.2	0.23±0.02
1000	23.5±4.4	0.31±0.07

[1]Estimates of ε were obtained using a detector bin time of 9 μs and *F* values from 0.3-0.9.

Table 4.2: PCH of competition binding between 50 nM FITC-insulin and insulin on RBL-2H3 cells.

Insulin (nM)	***N***	**ε (kHz)**[1]
0.025	12.6±3.1	0.25±0.04
0.25	10.1±4.0	0.24±0.03
2.5	8.3±3.6	0.24±0.04
25	8.4±4.3	0.22±0.02
250	4.0±1.3	0.21±0.02
2500	3.9±1.3	0.20±0.02
25000	2.4±0.5	0.17±0.02

[1]Estimates of ε were obtained using a detector bin time of 9 μs and *F* values from 0.3-0.9.

Table 4.3: SPT measurements of quantum dot-labeled IR on live RBL-2H3 cells before and after treatment with insulin, cytochalasin D or MβCD.

Treatment	**Macroscopic Diffusion ($10^{-10}cm^2s^{-1}$)**	**Compartment Diagonal (nm)**
Untreated	1.05±0.40	472±9
50 nM Insulin	0.34±0.07[1]	239±22[1]
250 nM Insulin	0.27±0.02[1]	266±11[1]
40 μg/mL Cytochalasin D	17.1±2.5[1]	984±94[1]
10 mM MβCD	11.2±1.4[1]	599±46[2]

[1]Student's t-test ($p < 0.01$) indicates values are significantly different compared to respective values measured on untreated cells.
[2]Student's t-test ($p < 0.1$) indicates values are significantly different compared to respective value measured on untreated cells.

Table 4.4: HomoFRET measurements of IR labeled with 1μM FITC-insulin on RBL-2H3 cells.

Treatment	**Initial r**	**Final r**	**Δr**	**E (%)**
Untreated	0.13±0.02	0.19±0.02	0.06±0.01	32
4% Paraformaldehyde	0.15±0.02[1]	0.20±0.02	0.04±0.01[1]	25
40μg/mL Cytochalasin D	0.15±0.02[1]	0.19±0.02	0.04±0.01[1]	21
10mg/mL MβCD	0.10±0.02[1]	0.15±0.02[1]	0.05±0.01[1]	33
MβCD and Cytochalasin D	0.12±0.01	0.15±0.02[1]	0.03±0.01[1]	20

[1]Student's t-test ($p < 0.01$) indicates values are significantly different compared to respective values measured on cells with untreated prior to labeling with 1 μM FITC-insulin.

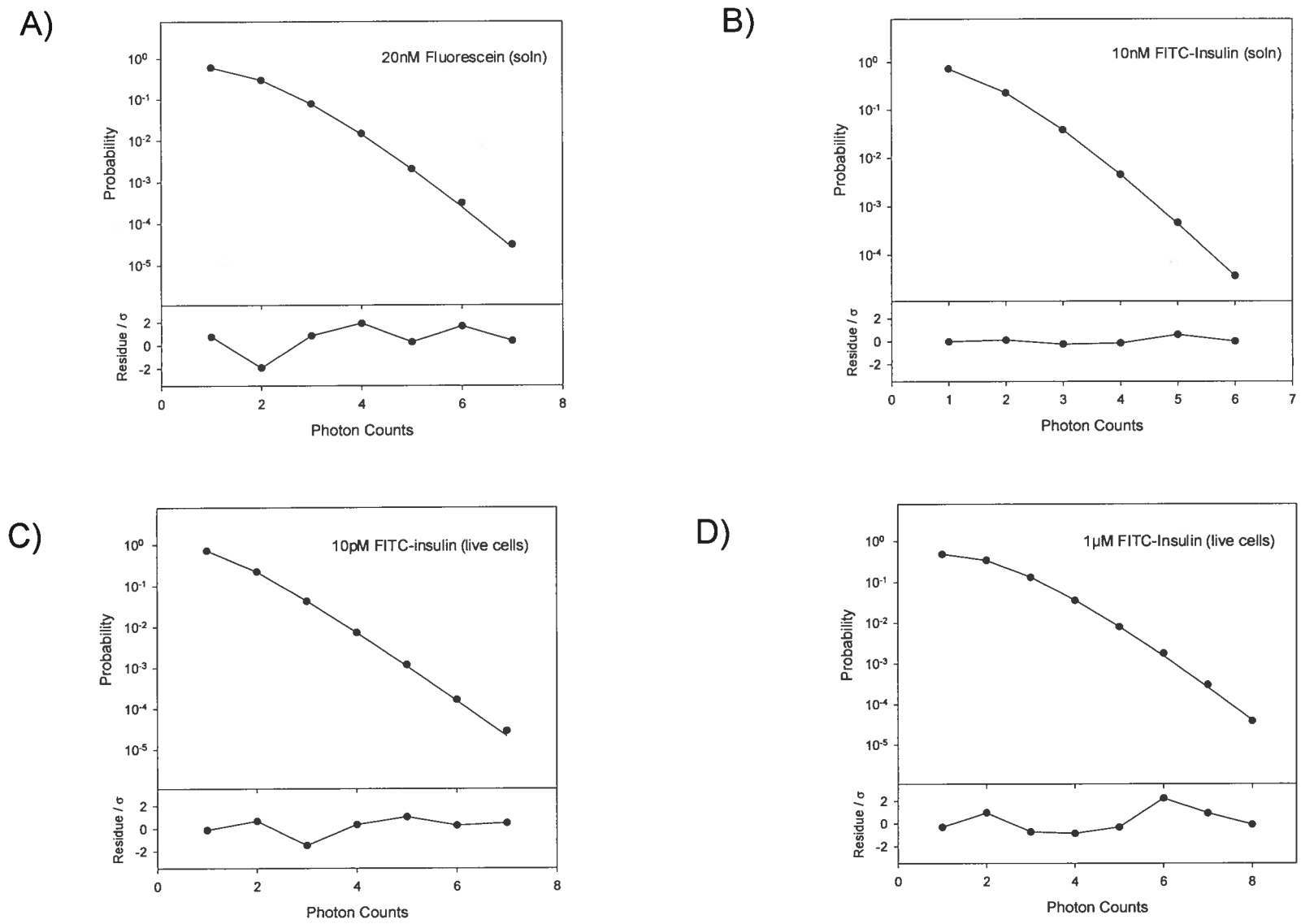
A)
20nM Fluorescein (soln)
Probability
Residue / σ
Photon Counts
B)
10nM FITC-Insulin (soln)
Probability
Residue / σ
Photon Counts
C)
10pM FITC-insulin (live cells)
Probability
Residue / σ
Photon Counts
D)
1μM FITC-Insulin (live cells)
Probability
Residue / σ
Photon Counts

Figure 4.1

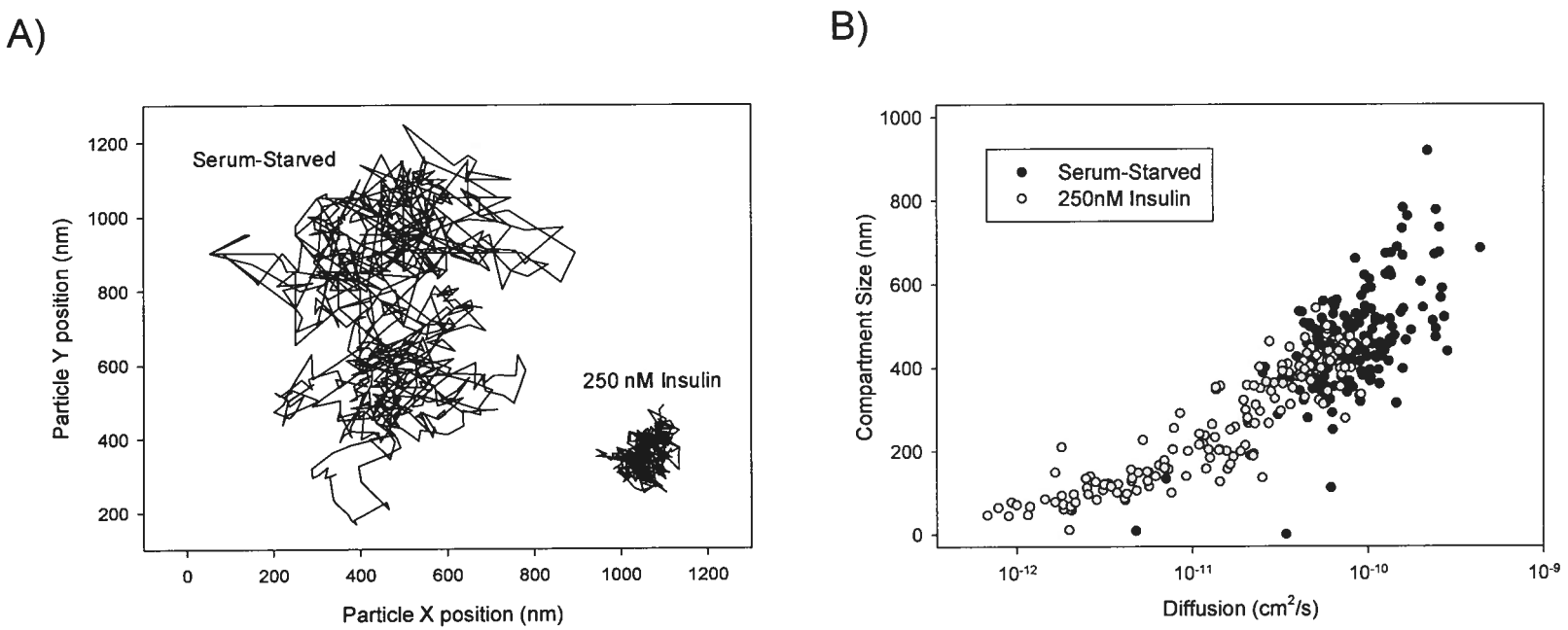
A)
Serum-Starved
250 nM Insulin
Particle Y position (nm)
Particle X position (nm)
1200
1000
800
600
400
200
0
200
400
600
800
1000
1200
B)
Serum-Starved
250nM Insulin
Compartment Size (nm)
Diffusion (cm²/s)
1000
800
600
400
200
0
10-12
10-11
10-10
10-9

Figure 4.2

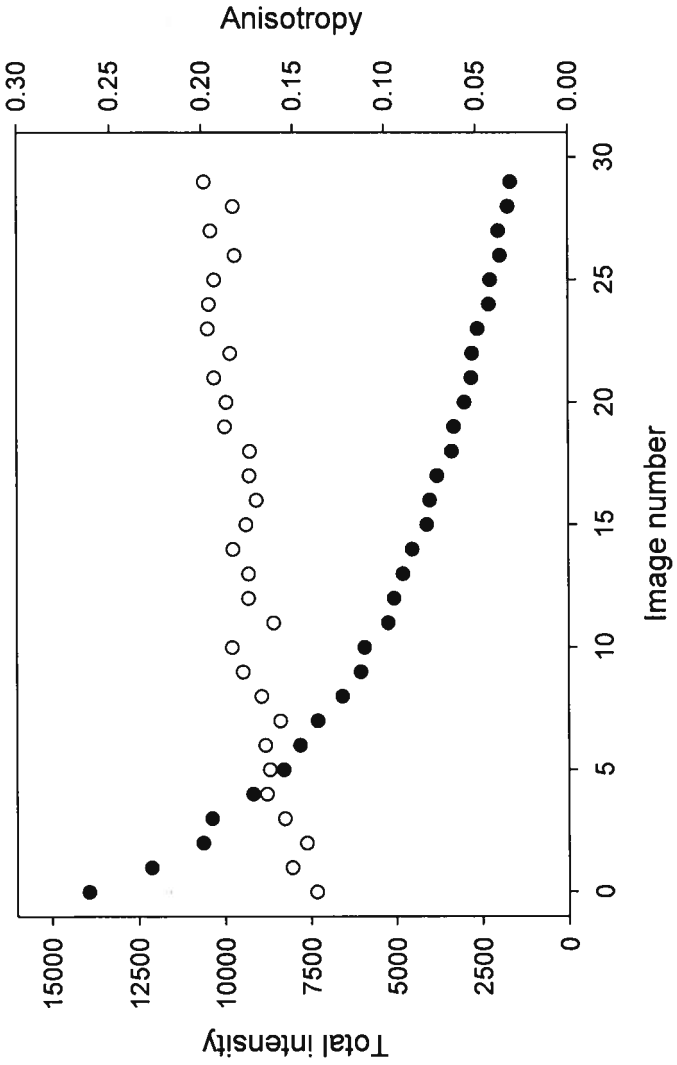
Anisotropy
0.30
0.25
0.20
0.15
0.10
0.05
0.00
15000
12500
10000
7500
5000
2500
0
Total intensity
0
5
10
15
20
25
30
Image number

Figure 4.3

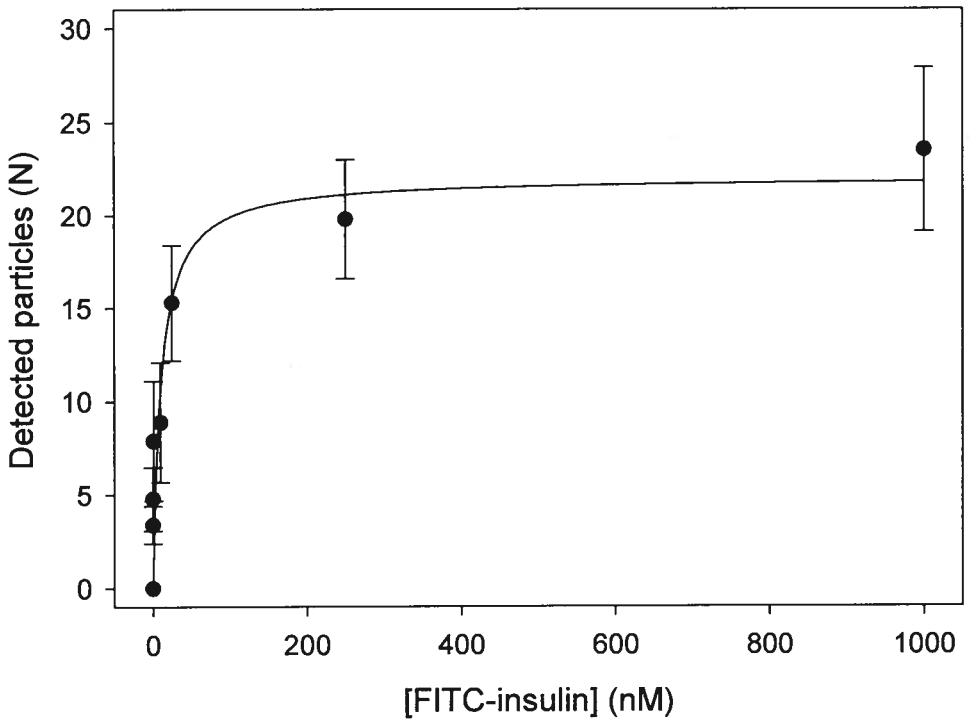

Supplement 4.1: The average number of particles detected during PCH of RBL-2H3 cells labeled with increasing concentrations of FITC-insulin was fit to a single-site ligand-binding model.

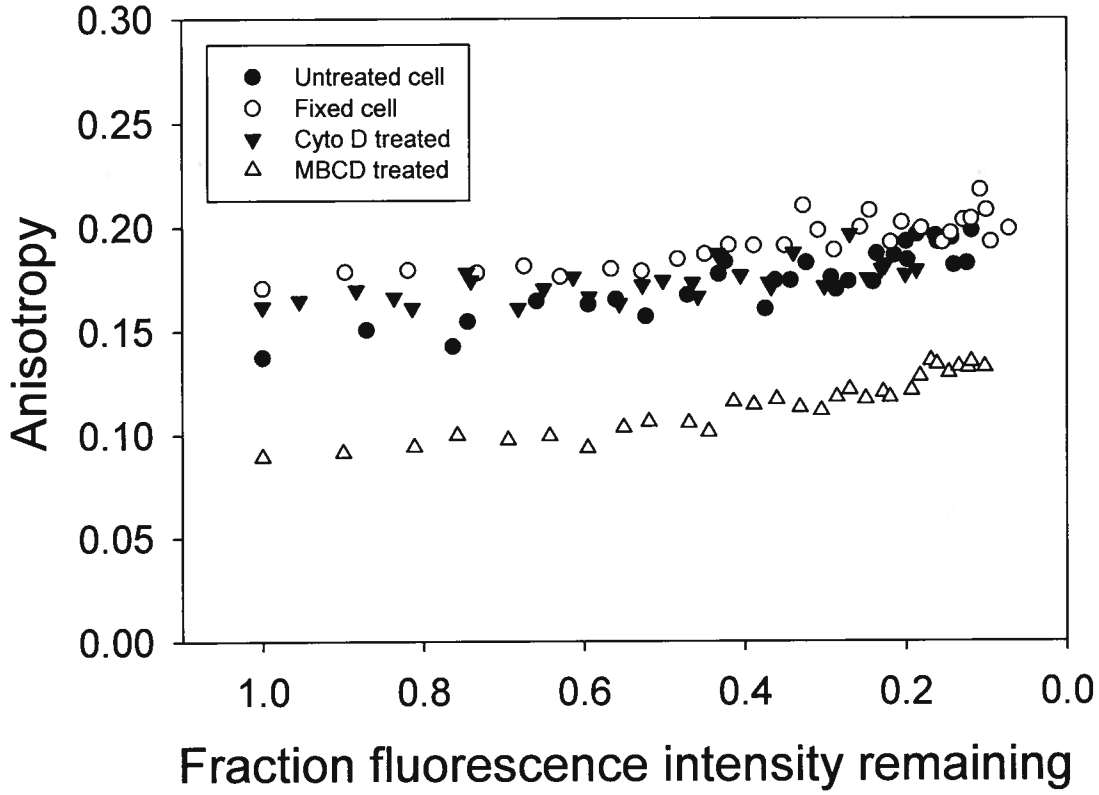

Supplement 4.2: The increase in anisotropy as a function of the fraction of total fluorescence intensity remaining.

Chapter V: Peter W. Winter performed single particle tracking shown in Figure 1, fluorescence correlation spectroscopy shown in Figure 3 and fluorometric assessment of live cell lipid order shown in Figure 4.

Probing the Anti-Diabetic Activity of Vanadium Compounds: Effects of Bis(maltolato)oxovanadium(IV) on the Lateral Diffusion of Insulin Receptors in Membrane Microdomains

Peter W. Winter[1,*], Abeer Al-Qatati[2,*], Amber L. Wolf-Ringwall[2], Samantha Schoeberl[2], Alan K. Van Orden[3], Debbie C. Crans[1,3], B. George Barisas[1,3] and Deborah A. Roess[1,2,#],

[1]Cell and Molecular Biology Program, [2]Department of Biomedical Sciences, [3]Department of Chemistry, Colorado State University, Fort Collins, Colorado 80523; *These authors contributed equally to this work; [#]Address all correspondence and requests for reprints to; Prof. Deborah A. Roess, Department of Biomedical Sciences, Campus Mail 1872, Colorado State University, Fort Collins, CO 80523. Email: daroess@lamar.colostate.edu.

We compare the effects of insulin and bis(maltolato)oxovanadium(IV) (BMOV) on the lateral motions of individual insulin receptors (IR) and the association of IR, phosphorylated IR (pIR) and phosphorylated insulin receptor substrate-1 (pIRS-1) with chemically-isolated plasma membrane microdomains on rat basophilic leukemia (RBL-2H3) cells. Single particle tracking experiments indicate that individual quantum dot-labeled IR on live, untreated RBL-2H3 cells exhibit relatively unrestricted lateral diffusion of approximately$1x10^{-10}$ cm^2s^{-1} and are confined in approximately 475 nm size cell-surface membrane compartments. After treatment with either 250 nM insulin or 10 μM BMOV, IR lateral diffusion and the size of IR-containing membrane compartments is significantly reduced. These treatments also increase the association of IR and pIRS-1 with low-density, detergent-resistant membrane fragments isolated using isopycnic sucrose-gradient centrifugation. Additionally, confocal fluorescence microscopic imaging of live RBL-2H3 cells labeled with the phase-sensitive aminonaphthylethenylpyridinium-based dye, Di-4-ANEPPDHQ, indicate that treatment with BMOV, but not insulin, decreases cell-surface plasma membrane lipid order and fluorescence correlation spectroscopy measurements suggest that BMOV treatment does not affect IR surface-density or insulin binding affinity. Finally, ^1H NMR spectroscopy of cetyl trimethylammonium bromide (CTAB) micelle model membranes shows that an oxidized form of BMOV readily localizes to the lipid-water interface and appears to interact directly with CTAB head-groups. Combined, these results suggest that activation of IR signaling by both insulin and BMOV involves increased association of IR with specialized, nanoscale membrane microdomains but that the insulin-like activity of

BMOV is due to changes in cell-surface membrane lipid order rather than to direct interactions with IR.

Keywords: Insulin receptor, membrane microdomain, vanadium, single particle tracking, lipid-order

1. Introduction

A number of vanadium-containing compounds have been shown to exert insulin-enhancing effects [10], including improvements in both insulin sensitivity and glucose homeostasis in animal models of type I [11, 12] and type II [13, 14] diabetes mellitus, as well as, in certain diabetic human subjects [15]. Several studies have also shown that, *in vitro,* vanadium compounds can act as potent inhibitors of protein tyrosine phosphatases, including protein tyrosine phosphatase 1B (PTP1B) [16, 17]. However, the diverse effects of vanadium-containing compounds *in vivo,* along with evidence of their direct interactions with model membranes [18] and effects on both lipid packing and membrane composition [19, 20], suggest that these compounds may also interact directly with biological membranes.

Several lines of evidence suggest the importance of specialized membrane microdomains in insulin-mediated insulin receptor (IR) signaling [1, 2]. These include interactions of IR downstream substrates and regulatory molecules with both resident lipid raft proteins such as caveolin [1, 2] and cholesterol-containing membrane structures

[3-8]. It appears that these specialized membrane microdomains facilitate insulin signaling by spatially organizing IR and IR signaling molecules and that disruption of these structures significantly reduces downstream IR signaling efficacy. Although, it is still not clear exactly how these membrane microdomains function in IR signaling as there is some evidence that prolonged localization of IR in cholesterol-containing membrane microdomains can lead to insulin resistance in neuronal cells [9].

Here, we have compared the effects of insulin and bis(maltolato)oxovanadium(IV) (BMOV) on lateral motions of *individual* native IR on live rat basophilic leukemia (RBL-2H3) cells and on the association of IR, phosphorylated IR (pIR), phosphorylated insulin receptor substrate-1 (pIRS-1) with chemically-isolated, detergent-resistant plasma membrane microdomains. Using the phase-sensitive aminonaphthylethenylpyridinium-based dye, Di-4-ANEPPDHQ, we also compared the effects of insulin and BMOV on live RBL-2H3 cell surface membrane lipid order and using fluorescence correlation spectroscopy we examined the effects of BMOV on IR surface-density and insulin binding affinity. Finally, using ^{1}H NMR spectroscopy we investigated whether an oxidized form of BMOV interacted directly with amphipathic lipids in a simple micelle model membrane system and propose two potential orientations of BMOV within biological membranes.

2. Materials and Methods

2.1 Materials

Minimum Essential Medium (MEM) with Earle's Balanced Salts was purchased from Thermo Scientific (Logan, Utah). Fetal bovine serum (FBS) and fungizone were purchased from Gemini BioProducts (Woodland, CA). Insulin from bovine pancreas, anti-phospho-insulin receptor (Tyr^{972}) IgG, methyl-β-cyclodextrin (MβCD), FITC-avidin, and anti-rabbit-biotin IgG were purchased from Sigma-Aldrich (St. Louis, MO). Anti-insulin receptor-β (C-19) IgG, anti-insulin receptor-β-biotin (C-19) IgG, anti-insulin receptor-α (N-20) IgG and anti-phospho-IRS-1 (Tyr^{632}) IgG were purchased from Santa Cruz Biotechnology (Santa Cruz, CA). BMOV and oxidized BMOV were synthesized and characterized as previously described [21, 22]. Di-4-ANEPPDHQ, and Qdot605-streptavidin-conjugated quantum dots were purchased from Invitrogen (Carlsbad, CA). Complete mini protease inhibitor cocktail tablets were purchased from Roche (Indianapolis, IN). 35mm, #1.5 glass bottom petri dishes were purchased from Willco Wells (Amsterdam, Netherlands)

2.2 Cell Lines

RBL-2H3 cells were maintained in medium that included MEM supplemented with Earle's Balanced Salts, 10% FBS, 200 mM L-glutamine, 10,000 U/mL penicillin G, 10 μg/ml streptomycin and 25 μg/ml fungizone. In some experiments, cells were incubated in supplemented MEM without FBS for at least 12-16 hr to remove an endogenous source of insulin.

2.3 Single particle tracking

RBL-2H3 cells were seeded onto sterile Willco Wells #1.5 glass bottom culture dishes and grown to 50% confluence. All labeling was performed in Tyrodes buffer containing 0.1% BSA. In experiments using quantum dots to track individual IR, cells were labeled first with anti-IR-β-biotin antibody at 0.2 μg/mL for 30-40 min, washed 3 times for 1 min in 1mL of buffer and labeled with 100 pM quantum dot probe Qdot605-streptavidin conjugate for 10 min and then washed at least 6 times for 1 min in 1mL to remove unbound probe. This is modified from accepted protocols for minimizing the effects of probe-induced receptor-crosslinking [23]. Wide-field fluorescence images were then collected from the apical surface of live cells using a Zeiss Axiovert 200M microscope equipped with a 63x 1.2 NA apochromatic water-immersion objective and custom filters. Images were collected every 33 ms for up to 3 min at a total magnification of 315x with an Andor Ixon EM+ camera resulting in a final pixel size of 49.6 nm. This was achieved using a Zeiss 2.5x Optovar and a C-mount 2x magnifying lens placed in front of the camera. Image acquisition and determination of individual particle locations were performed with MetaMorph 7.1.6 (Molecular Devices). Macroscopic diffusion rates and compartment diagonals were determined using custom analysis programs. Blinking of individual IR-bound quantum dot particles, while apparent, did not prevent tracking over long periods of time. The trajectories of individual particles were segmented into domains by calculation of statistical variance in particle position over time [24, 25] producing variance plots that exhibited peaks at inter-domain boundaries. These results were analyzed to yield the domain size and residence time for each particle. Effective macroscopic diffusion was calculated as the square of

the domain diagonal divided by four times the residence time in the domain as previously described [26]. SPT values shown each reflect measurements of 30-100 total particles on 10-20 individual RBL-2H3 cells.

2.4 Isolation of plasma membrane fragments

RBL-2H3 cells were incubated with 200 nM insulin for 1 hr at 37°C, with 10μM BMOV overnight at 37°C or with both 10μM BMOV overnight and 200 nM insulin for 1 hr at 37°C. To isolate membrane rafts from RBL-2H3 cells, $5x10^7$ cells were washed two times with phosphate-buffered saline, pH 7.4 (PBS) and lysed for 5-10 min on ice in 1 mL of a buffer containing 25 mM MES, 150 mM NaCl, 2mM EDTA, 0.25% Triton-X100, and a protease inhibitor cocktail including aprotinin, leupeptin, EDTA, and PMSF. A low speed 300x g spin was used to remove cell nuclei and large cell debris. Supernatant from this spin which contained plasma membrane fragments, was then combined with an equal volume of 80% sucrose containing 0.25% Triton-X100 and protease inhibitors to produce a 40% sucrose solution. A discontinuous sucrose gradient from 10-80% was created with the sample in 40% sucrose layered within this gradient. The gradient was loaded into a Beckman SW-41 swinging bucket rotor and spun at 175,000x g for 20 hr at 4°C. After the spin, eighteen fractions were carefully collected from the top of the gradient downward. A 50 μL aliquot from each fraction was diluted 1:1 with 95% SDS and 5% β-mercaptoethanol. After separation of proteins from each fraction using SDS-PAGE and transfer of proteins to nitrocellulose, IR was identified using anti-IR-β antibody as previously described [27]. Fractions 1-9 contained low density membrane fragments and were designated as membrane rafts based on sucrose

concentrations of less than 40%, and the presence of the raft-specific marker flotillin (data not shown). In experiments evaluating membrane distributions of pIR and pIRS-1, 50 μL aliquots from fractions 7-12 were diluted 1:1 with 95% SDS and 5% β-mercaptoethanol and, after separation of proteins from each fraction using SDS-PAGE and transfer of proteins to nitrocellulose, pIR was identified using anti-pIR antibody and pIRS-1 was identified using anti-pIRS-1 antibody. Protein of interest in each fraction was determined using a Bio-Rad GS-800 calibrated densitometer. Sucrose concentrations were determined using a Bausch and Lomb refractometer. In some experiments, cells were treated for 1 hr at 37°C with 10 mM MβCD, to deplete membrane cholesterol content after incubation with either insulin or BMOV. Differences between treated cells and untreated were evaluated using Student's paired t-test ($p<0.05$).

2.5 Fluorescence correlation spectroscopy

RBL-2H3 cells were seeded onto sterile dishes as described above. Prior to some FCS experiments, cells were treated with 10 μM excess insulin for 1 hr or 10 μM BMOV overnight. Cells were then sequentially washed and labeled with anti-IRα (N-20) rabbit IgG (SantaCruz Bio) for 30-40 min, anti-rabbit-biotin IgG (Sigma) for 20 min, and FITC-avidin for 15 min, washed and then submerged in 1 mL buffer. Alternatively, cells were labeled with FITC-insulin (Invitrogen) and then washed 4 times for 30 secs in 1mL of buffer. FCS experiments were performed on a modified Nikon TE1000 inverted microscope equipped with a 100x, 1.25NA, oil-immersion objective, an expanded Omnichrome/ Melles-Groit multi-line air-cooled argon ion laser operating at 514.5 nm, two 570/32 nm bandpass filters, two Perkin Elmer single photon counting modules

(SPCM-AQR-14) and an ALV-6010 digital hardware correlator as previously described [28]. The $1/e^2$ radius of the excitation beam at the sample was confirmed to be 241 nm using aqueous rhodamine-6G (data not shown). In live cell, studies the laser excitation beam was vertically positioned on the apical cell membrane by adjusting the objective z-position to maximize detector count rates and minimize diffusional correlation times (τ_D) as described by Ries and Schwille [29]. Samples were illuminated for approximately 10 sec before collection of data to allow for the irreversible photobleaching of immobile particles [30]. Data was then collected for two consecutive 10 sec intervals during which time the average fluorescence from the sample was relatively uniform as indicated by the photodiode signal readouts (data not shown). Analysis of correlation data, including determination of τ_D and the normalized initial $G(\tau)$ were accomplished according to established procedures using Igor Pro 5.05A [31-33].

2.6 Measurement of plasma membrane lipid order

RBL-2H3 cells were seeded onto sterile dishes as described above and treated with 50 nM or 250 nM insulin for 1hr or with 10μM BMOV overnight. In some experiments, cells were treated with 10mM MβCD for 1hr or loaded with cholesterol or 7-dehydrocholesterol as previously described [34]. Cells were then labeled with 1μM Di-4-ANEPPDHQ for 30 minutes, washed and immersed in buffer for imaging. Confocal fluorescence images were acquired using an Olympus IX-71 inverted microscope equipped with a 60x, 1.2NA water-immersion objective and a Fluoview 300 confocal scanning unit. Cell samples were illuminated with a 488 nm laser. Fluorescence emission, split between detector channels 1 and 2 using a 560 nm dichroic mirror, was

collected simultaneously in channel 1 using a 530 nm long-pass filter and in channel 2 using a 610 nm long-pass filter. All images were collected at identical instrument and detector settings with the exception of the laser excitation power which was adjusted between experiments due to slight variations in labeling efficiency. Background correction and fluorescence intensity ratio calculation were performed using NIH Image J 1.42i.

2.7 ^{1}H NMR spectroscopy of CTAB micelles

Micelle samples were prepared from 50 mM CTAB in D_2O and 2 mM oxidized BMOV, also in D_2O. A Varian Inova 400 NMR spectrometer was utilized to obtain ^{1}H NMR spectroscopy measurements of the CTAB micelles and deuterated aqueous samples. CTAB micelle samples were referenced with internal DSS standard and aqueous stock samples were referenced with external DSS/D_2O.

3. Results

3.1 Individual insulin receptors exhibit restricted lateral diffusion following treatment with insulin or BMOV

(Insert Figure 5.1)

Changes in the lateral motions of cell-surface molecules such as IR are associated with ligand-mediated receptor signaling. We compared the effects of insulin and BMOV on the lateral motions of individual IR on the surface of live RBL-2H3 cells (Figure 5.1A

and 5.1B). When anti-IRβ conjugated fluorescent quantum dots were used to track the movement of individual IR on cells treated with either 50 nM or 250 nM insulin, the average diffusion coefficient was reduced from approximately $1x10^{-10}cm^2s^{-1}$ to approximately $3x10^{-11}cm^2s^{-1}$. Treatment with 10 μM BMOV for 2 or 12 hr also reduced the lateral diffusion coefficients of individual IR to approximately $6x10^{-11}cm^2s^{-1}$. Additionally the average size of the compartments accessed by IR was reduced from approximately 500 nm to less than 300 nm with insulin treatment and to approximately 400 nm after exposure to 10 μM BMOV (Figure 5.1B).

3.2 Insulin receptors and phosphorylated IRS-1 associate with low-density membrane microdomains following treatment with insulin or BMOV

(Insert Figure 5.2)

(Insert Table 5.1)

(Insert Table 5.2)

Incubation of RBL-2H3 cells overnight in serum-free media containing 10 μM BMOV, treatment for 1 hr with 200 nM insulin or treatment with both insulin and BMOV resulted in redistribution of IR from high density membrane fractions characteristic of the bulk membrane to low density detergent-resistant membrane fractions (Figure 5.2). Isopycnic gradient centrifugation of plasma membrane fractions from RBL-2H3 cells incubated in serum free medium showed that less than 3% of IR were associated with low-density fractions of less than 40% sucrose and that over 97% of IR were localized in high-density fractions of greater than 40% sucrose characteristic of the bulk plasma

membrane (Table 5.1). Treatment with 200 nM insulin for 1 hr increased the relative number of IR in lower density sucrose fractions to over 21% (Figure 2) and treatment of cells with 10 μM BMOV overnight increased the amount of IR in lower density sucrose fractions to approximately 26% (Table 5.1). Similarly, when RBL-2H3 cells were treated with 10 μM BMOV for at least 12hr and then with 200 nM insulin for 1 hr, nearly 28% of IR were found in low density membrane fractions.

The overall distribution of pIR in detergent-resistant fractions was not significantly affected by 1hr treatment with 250 nM insulin or incubation overnight with 10 μM BMOV. In fact, the distribution of pIR in low and high density membrane fractions was only significantly altered by treatment with 10 mM MβCD (Table 5.2).

In contrast to pIR, both insulin and BMOV treatments significantly increased the association of pIRS-1 with membrane fractions. pIRS-1 detected in low density fractions increased from 5% in untreated cells to over 61% after 250 nM insulin treatment and to 86% after treatment with 10 μM BMOV (Table 5.2). Incubation of cells for 1 hour in 10 mM MβCD reduced pIRS-1 in detergent-resistant low density membrane fractions to levels that did not differ significantly from untreated cells.

3.3 Insulin receptor surface density and insulin binding affinity following treatment with BMOV

(Insert Figure 5.3)

At least one previous study has reported that vanadium-containing peroxovanadates can interact directly with IR and affect insulin binding affinity *in vitro*

[35]. We used FCS to investigate the effects of BMOV on IR cell-surface density and insulin binding affinity. Treatment of RBL-2H3 cells with 10 μM insulin or 10 μM BMOV did not affect the apparent surface density of IR on RBL-2H3 cells within the interrogation volume using an anti-IRα primary IgG (Figure 5.3A). In addition, the observed binding affinity of FITC-insulin for IR was generally consistent with that reported by Zhong *et al.* [36] who used FCS to investigate the binding of TRITC-insulin to receptors on human renal tubular cells. Treatment with 10 μM BMOV also did not appear to affect the number of sites available for insulin binding or the affinity of insulin for available IR binding sites (Figure 5.3B). These data suggest that the insulin-like effects of BMOV do not result from direct interactions with IR or insulin and are similar to previous studies investigating IR interactions with other vanadium-containing compounds [37].

3.4 Live cell plasma membrane lipid order following treatment with insulin or BMOV

(Insert Figure 5.4)

The use of Di-4-ANEPPDHQ for both the measurement of membrane order and the identification of cholesterol enriched domains has only recently been reported [38, 39]. However, in that time, Di-4-ANEPPDHQ has been shown to be a powerful tool for probing membrane lipid order in live cells [40, 41]. We utilized Di-4-ANEPPDHQ to investigate the relative extent of lipid order in the plasma membrane of RBL-2H3 cells treated with insulin or BMOV. Although quite soluble in water, Di-4ANEPPDHQ also readily associates with biological membranes and has a peak emission wavelength that depends on the relative order of surrounding molecules. The ratio, (610 nm/530 nm), of

fluorescence emission from Di-4-ANEPPDHQ in cells maintained in serum-starved medium and in cell treated with insulin was approximately 0.7 and suggests that insulin binding does not alter membrane lipid order (Figure 5.4). However, the ratio of fluorescence emission increased to 0.95 in 10 μM BMOV-treated cells indicating an apparent decrease in lipid order and incubation of cells for 1 hr with 10 mM MβCD to deplete membrane cholesterol content, increased the ratio of fluorescence emission to approximately also 1.3 indicating a decrease in membrane lipid order. Alternatively, loading cells with excess cholesterol caused a small increase in lipid order compared to cells grown in serum-containing medium (Figure 5.4).

3.5 Interaction of oxidized BMOV with CTAB micelles

(Insert Figure 5.5)

To determine if the effects of BMOV on live cell plasma membrane lipid order where due to direct interactions between BMOV and amphipathic molecules of the lipid biliayer, we examined the interactions of BMOV with CTAB in a simple micelle model membrane system. We compared the ^{1}H NMR spectra of oxidized BMOV in bulk D_2O to the spectra of oxidized BMOV in CTAB micelles. BMOV is believed to be readily oxidized in solution [42, 43] and is suitable for NMR spectral examination. The 0.1-0.2 ppm upfield shifts of both H_a and H_b of oxidized BMOV in CTAB micelles compared to in D_2O indicate penetration into the micelle interface (Figure 5.5A). This interpretation is consistent with previous interpretations of ^{1}H NMR spectra of solute system interactions [44, 45]. Figure 5.5B illustrates two potential orientations of the oxidized BMOV within the micelle both of which would likely result in a significant reordering of

the surrounding lipids and are consistent with the interactions observed here and observed previously for a variety of insulin-like vanadium-compounds and lipid molecules in Langmuir monolayers (A. Sostarecz, personal communication), micelles [46, 47] and reverse micelles [48].

4. Discussion

A growing body of evidence suggests that membrane rafts can serve as signaling platforms for cell-surface receptors [49-51] including IR. Our results demonstrate that IR redistribute from the bulk membrane into nanoscale plasma membrane microdomains with characteristics similar to lipid rafts [52] in response to either insulin or BMOV treatment. The translocation of IR to rafts has previously been described by Vainio *et al* [53] who studied Triton X-100 insolubility of IR in hepatoma cells and found that, after insulin treatment, IR was localized within detergent-resistant membrane fragments. Additionally, in some cell types, insulin-treated IR can preferentially segregate into caveolae, a subset of detergent-resistant lipid rafts containing high levels of caveolins [54] and other investigators have shown that phosphorylation of IR and downstream targets such as IRS-1 involves interactions with lipid raft-like membrane microdomains [55] and that disruption of these structures is associated with insulin resistance [56].

While insulin-mediated activation of IR is relatively well-characterized, the mechanism for the insulin-like activity of BMOV is less clear. Vanadium-containing compounds are known *in vitro* inhibitors of protein tyrosine phosphatases [17] and it is possible that the activation of IR and IRS-1 seen in our investigations resulted from

decreased dephosphorylation of IR by PTP1B. In fact, vanadate has been shown to stimulate tyrosine phosphorylation of IR in rat adipocytes [57], sodium orthovanadate reversed the decreased tyrosine phosphorylation of IR in STZ diabetic rats [58] and BMOV specifically increased tyrosine phosphorylation of IR [59]. However, the inhibition of protein phosphatases by BMOV does not explain either, the effects of BMOV on distribution of cell-surface IR, or the apparent effects of BMOV on cell-surface plasma membrane order. The question that arises from our results is whether the raft localization of IR and inhibition of tyrosine phosphatase activity may both be required for the insulin-like effects of BMOV.

The importance of cholesterol-containing rafts in receptor-mediated signaling is evident from the effects of membrane cholesterol depletion [60, 61]. For example in insulin-mediated signaling, insulin-stimulated glucose uptake, down-stream tyrosine phosphorylation of both IRS-1and protein kinase B, and insulin-dependent binding of IRS-1 to IR were all inhibited when 3T3-L1 adipocytes were treated with MβCD to extract membrane cholesterol [62]. Similarly, our results indicate that disruption of cholesterol-dependent, membrane microdomains reduced the appearance of pIR and pIRS-1 in high-buoyancy membrane compartments. This behavior would arise if insulin-mediated IR and IRS-1 activation is most efficient within lipid rafts where higher concentrations of associated signaling molecules exist. BMOV, despite its known activity as a PTP1B inhibitor, was not able to counteract the effects of MβCD treatment. The disruption of lipid rafts may not, however, completely eliminate IR-mediated signal transduction. As reported by Vainio et al [53], there seems to be some IR and IRS-1 that remain within the bulk membrane, albeit at reduced concentrations.

Unlike insulin, it is clear that BMOV is able to interact with amphipathic lipids in model membrane systems and significantly decreases plasma membrane lipid order in live cells. However, the effects of BMOV on membrane order reported here, differ from previously reported effects of other vanadium-containing compounds with insulin-like activity including $NaVO_3$, vanadyl acetylacetonate, and vanadium dipciolinate which, in isolated erythrocyte membranes, increased membrane order [63]. Although, our results are consistent with those of Siddiqui et al [20] who observed decreased membrane lipid order after treating alloxan monohydrate-induced diabetic rats with Trigonella and sodium orthovanadate. Our results also support those of Owen et al [64] who used Di-4-ANEPPDHQ to investigate the effects of temperature and membrane cholesterol content on lipid order in live HEK-293 cells. It appears that, by decreasing lipid order without disrupting raft domains, BMOV may alter the preferred environment of cell-surface IR, resulting in increased retention of IR in specialized, nanoscale membrane structures and the likelihood that IR and downstream substrates, including IRS-1, are activated.

Together, our data suggest the involvement of specialized, nanoscale membrane microdomains in insulin-mediated IR signaling and suggest that the spatial coordination of key signaling proteins, such as IRS-1 within these microdomains provides an efficient mechanism for promoting IR signal transduction. Although association of IR with the nanoscale membrane structures observed here appears to be affected by both BMOV and insulin, the mechanisms employed by these molecules to initiate IR-mediated signaling differ. While both insulin and BMOV reduce IR lateral diffusion and result in increased association of IR and pIRS-1 with specialized, detergent-resistant membrane structures, BMOV alone reduces plasma membrane lipid order. This suggests the insulin-like

effects of BMOV are most likely not due to direct interactions with IR or changes in IR surface density. Rather, BMOV may be able to interact directly with cell-surface plasma membranes, driving changes in lipid order that lead to increased compartmentalization and activation of IR and IRS-1.

5. Acknowledgements

We would like to thank Dr. Audra Sostarecz, Monmouth College, for her time discussing interactions between vanadium-containing compounds and Langmuir monolayers. This project was supported by the National Science Foundation (grant number CHE0628260); the National Institutes of Health (grant number RR023156); and the American Heart Association (grant number AHA0650081Z).

6. Figure Legends

Figure 1: Single particle tracking of individual insulin receptors. A. Diffusion coefficients from single particle tracking of IR using quantum dots. Both insulin and BMOV treatments reduced IR lateral diffusion significantly when compared to untreated serum starved cells. Shown are the average values and SEM from at least 20 individual particle measurements. B. Values for compartment size from single particle tracking of insulin receptors using quantum dots. Individual values for compartment sizes were calculated from particle tracks of insulin receptors before and after treating cells with 250 nM insulin or 100 μM BMOV, both treatments caused a reduction in the size of compartments accessed by insulin receptors compared to untreated cells. Each point shown is the average value and SEM from at least 20 individual particle measurements. Values identified by superscripts a, b, or c, were significantly different ($p<0.01$) using an unpaired Student's t-test with two-tailed distribution.

Figure 2: Insulin receptor membrane raft localization. Western-blot analysis of plasma membrane fractions from RBL-2H3 cells shows that before exposure to insulin, IR appeared in high density sucrose fractions and that treatment with 200 nM insulin and/or 10 μM BMOV caused IR redistribution into lower density fractions. Shown are the mean and SEM for at least 3 individual experiments.

Figure 3: Effects of BMOV on insulin receptor cell-surface density and insulin binding affinity: A. Fluorescence correlation spectroscopy measurements of the binding of anti-IRα IgG to live RBL-2H3 cells before or after 1 hr insulin or 12 hr 100 μM BMOV treatment showed no apparent change in IR surface density within the 241 nm xy-radius interrogation volume. Shown is the mean and S.D. of measurements from at least 10 individual cells. B. Insulin-FITC equilibrium binding was examined after 12 hr treatment with 100 μM BMOV which did not affect the availability of IR binding sites or the apparent affinity of insulin-FITC for IR. Exposure of cells to insulin or insulin-containing FBS significantly reduced availability of IR binding sites for insulin-FITC. Each point shown is the mean and S.D. of measurements from at least 12 individual cells.

Figure 4: Fluorescence emission of Di-4-ANEPPDHQ labeled RBL-2H3 cell membranes. Di-4-ANEPPDHQ fluorescence emission was collected simultaneously at 530 nm and 610 nm. Treatment of FBS starved RBL-2H3 cells with insulin appeared to have no effect on Di-4-ANEPPDHQ emission, whereas a significant increase in the emission ratio, indicating a change in membrane order, was seen following exposure of cells to 100 μM BMOV. Incubation of cells with MβCD increased the ratio of fluorescence emission to approx. 1.3 while loading cells with excess cholesterol or 7-dehydrocholesterol decreased the emission ratio to approx. 0.6. Each point shown is the mean and SD of measurements from at least 15 cells. Values with superscripts a, b, c, d were significantly different ($p<0.01$) using an unpaired Students t-test with two-tailed distribution.

Figure 5: BMOV interaction with CTAB micelles. A. 1H NMR spectra showing the interaction of an oxidized form of BMOV with a CTAB micelle model membrane system. The upfield shifts of two protons of the oxidized BMOV indicate penetration into

the micelle interface. B. Two proposed orientations of oxidized BMOV within the CTAB micelle interface are shown.

7. References

[1] Y. Ishikawa, K. Otsu and J. Oshikawa, Caveolin; different roles for insulin signal? Cellular Signalling 17 (2005) 1175-1182.

[2] F. Nystrom, H. Chen, L.-N. Cong, Y. Li and M. Quon, Caveolin-1 interacts with the insulin receptor and can differentially modulate insulin signaling in transfected Cos-7 cells and rat adipose cells Mol Endocrinol 13 (1999) 2013-2024.

[3] S. Parpal, M. Karlsson, H. Thorn and P. Stralfors, Cholesterol depletion disrupts caveolae and insulin receptor signaling for metabolic control via insulin receptor substrate-1, but not for mitogen-activated protein kinase control Journal of Biological Chemistry 276 (2001) 9670-9678.

[4] J. Gustavsson, S. Parpal, M. Karlsson, C. Ramsing, H. Thorn, M. Borg, M. Lindroth, K.H. Peterson, K.-E. Magnusson and P. Stralfors, Localization of the insulin receptor in caveolae of adipocyte plasma membrane The FASEB Journal 13 (1999) 1961-1971

[5] M. Karlsson, H. Thorn, S. Parpal, P. Stralfors and J. Gustavsson, Insulin induces translocation of glucose transporter GLUT4 to plasma membrane caveolae in adipocytes FASEB 10 (2001) 01-0646.

[6] M. Czech, PIP2 and PIP3: Complex roles at the cell surface Cell 100 (2000) 603-606.

[7] T. Maffucci, A. Brancaccio, E. Piccolo, R.C. Stein and M. Falasca, Insulin induces phosphatidylinositol-3-phosphate formation through TC10 activation 22 (2003) 4178-4189.

[8] G. Müller, C. Jung, S. Wied, S. Welte and W. Frick, Insulin-mimetic signaling by the sulfonylurea glimepiride and phosphoinositolglycans involves distinct mechanisms for redistribution of lipid raft components Biochemistry. 40 (2001) 14603-20.

[9] C. Taghibiglou, C. Bradley, T. Gaertner, Y. Li, Y. Wang and Y. Wang, Mechanisms involved in cholesterol-induced neuronal insulin resistance Neuropharmacology 57 (2009) 268-276.

[10] D.C. Crans, J.J. Smee, E. Gaidamauskas and L. Yang, The chemistry and biochemistry of vanadium and the biological activities exerted by vanadium compounds Chemical Reviews 104 (2004) 849-902.

[11] G.R. Willsky, L.-H. Chi, Y. Liang, D.P. Gaile, Z. Hu and D.C. Crans, Diabetes-altered gene expression in rat skeletal muscle corrected by oral administration of vanadyl sulfate Physiol. Genomics 26 (2006) 192-201.

[12] S. Karmaker, T.K. Saha and H. Sakurai, Antidiabetic activity of the orally effective vanadyl-poly (γ-glutamic acid) complex in streptozotocin(STZ)-induced Type 1 diabetic mice Journal of Biomaterials Applications 22 (2008) 449-464.

[13] S. Karmaker, T.K. Saha, Y. Yoshikawa and H. Sakurai, Amelioration of hyperglycemia and metabolic syndromes in type 2 diabetic KKA mice by poly(γ-glutamic acid)oxovanadium(IV) complex Chem Med Chem 2 (2007) 1607-1612.

[14] Y. Adachi, Y. Yoshikawa, J. Yoshida, Y. Kodera, A. Katoh, J. Takada and H. Sakurai, Improvement of diabetes, obesity and hypertension in type 2 diabetic KKA^{y} mice by bis(allixinato)oxovanadium(IV) complex Biochem Biophys Res Comm 345 (2006) 945-950.

[15] K.H. Thompson, J. Lichter, C. LeBel, M.C. Scaife, J.H. McNeill and C. Orvig, Vanadium treatment of type 2 diabetes: A view to the future Journal of Inorganic Biochemistry 103 (2009) 554-558.

[16] J. Li, G. Elberg, D.C. Crans and Y. Shechter, Evidence for the distinct vanadyl(+4)-dependent activating system for manifesting insulin-like effects Biochemistry. 35 (1996) 8314-8.

[17] M. Li, W. Ding, B. Baruah, D.C. Crans and R. Wang, Inhibition of protein tyrosine phosphatase 1B and alkaline phosphatase by bis(maltolato)oxovanadium (IV) Journal of Inorganic Biochemistry 102 (2008) 1846-1853.

[18] D.A. Roess, S.M.L. Smith, P. Winter, J. Zhou, P. Dou, B. Baruah, A.M. Trujillo, N.E. Levinger, X. Yang, B.G. Barisas and D.C. Crans, Effects of vanadium-containing compounds on membrane lipids and on microdomains used in receptor-mediated signaling Chemistry & Biodiversity 5 (2008) 1558-1570.

[19] E. Amler, J. Teisinger, J. Svobodová and F. Vyskocil, Vanadyl ions increase the order parameter of plasma membranes without changing the rotational relaxation time Biochimica et Biophysica Acta (BBA) - Biomembranes 863 (1986) 18-22.

[20] M. Siddiqui, A. Taha, K. Moorthy, M. Hussain, S. Basir and N. Baquer, Amelioration of altered antioxidant status and membrane linked functions by vanadium and Trigonella in alloxan diabetic rat brains. J Bioscience 30 (2005) 483-90.

[21] J.H. McNeill, V.G. Yuen, H.R. Hoveyda and C. Orvig, Bis(maltolato)oxovanadium(IV) is a potent insulin mimic Journal of Medical Chemistry 35 (1992) 1489-1491.

[22] C. Orvig, J.H. McNeill and J. Vasilevskis. Vanadium compounds as insulin mimics in (Sigel, H. and Sigel, A., eds.) Metal Ions in Biological Systems, Marcel Dekker, Inc., New York 1995, pp. 575-594.

[23] D.S. Lidke, P. Nagy, R. Heintzmann, D. Arndt-Jovin, J. Post, H. Grecco, E. Jares-Erijman and T. Jovin, Quantum dot ligands provide new insights into erbB/HER receptor-mediated signal transduction Nature Biotechnology 22 (2004) 198-203.

[24] K. Murase, T. Fujiwara, Y. Umemura, K. Suzuki, R. Iino, H. Yamashita, M. Saito, H. Murakoshi, K. Ritchie and A. Kusumi, Ultrafine membrane compartments for molecular diffusion as revealed by single molecule techniques Biophys J 86 (2004) 4075-4093.

[25] F. Daumas, N. Destainville, C. Millot, A. Lopez, D. Dean and L. Salomé, Confined diffusion without fences of a G protein coupled receptor as revealed by single particle tracking Biophysical Journal 84 (2003) 356-366.

[26] M.J. Saxton, Single-particle tracking: the distribution of diffusion coefficients Biophys J 72 (1997) 1744-1753.

[27] D.A. Roess and S.M.L. Smith, Self-association and raft localization of functional luteinizing hormone receptors Biol Reprod 69 (2003) 1765-1770.

[28] K. Fogarty, J. McPhee, E. Scott and A. Van Orden, Probing the ionic atmosphere of single-stranded DNA using continuous flow capillary electrophoresis and fluorescence correlation spectroscopy Anal. Chem. 81: (2009) 465-472.

[29] J. Ries and P. Schwille, New concepts for fluorescence correlation spectroscopy on membranes Physical Chemistry 10 (2008) 3487-3497.

[30] S. Chiantia, J. Ries and P. Schwille, Fluorescence correlation spectroscopy in membrane structure elucidation Biochimica et Biophysica Acta 1788 (2009) 225-233.

[31] Q. Ruan, Y. Chen, E. Gratton, M. Glaser and W.W. Mantulin, Cellular characterization of adenylate kinase and its isoform:two-photon excitation fluorescence imaging and fluorescence correlation spectroscopy Biophysical Journal 83 (2002) 3177-3187.

[32] P. Schwille, U. Haupts, S. Maiti and W.W. Webb, Molecular dynamics in living cells observed by fluorescence correlation spectroscopy with one- and two-photon excitation Biophysical Journal 77 (1999) 2251–2265.

[33] Y. Chen, A.C. Munteanu, Y.-F. Huang, J. Phillips, Z. Zhu, M. Mavros and W. Tan, Mapping receptor density on live cells by using fluorescence correlation spectroscopy Chemistry - A European Journal 15 (2009) 5327-5336.

[34] P. Singh, Y.D. Paila and A. Chattopadhyay, Differential effects of cholesterol and 7-dehydrocholesterol on the ligand binding activity of the hippocampal serotonin1A receptor: Implications in SLOS Biochemical and Biophysical Research Communications 358 (2007) 495-499.

[35] D.W.J. Kwong, W.N. Leung, M. Xu, S.Q. Zhu and C.H.K. Cheng, Modulatory effects of peroxovanadates on insulin receptor binding Journal of Inorganic Biochemistry 64 (1996) 163-180.

[36] Z.-H. Zhong, A. Pramanik, K. Ekberg, O.T. Jansson, H. Jörnvall, J. Wahren and R. Rigler, Insulin binding monitored by fluorescence correlation spectroscopy Diabetologia 44 (2001) 1184-1188.

[37] M. Cam, R. Brownsey and J. McNeill, Mechanisms of vanadium action: insulin-mimetic or insulin-enhancing agent? Canadian Journal of Physiology and Pharmacology 78 (2000) 829-847.

[38] L. Jin, A. Millard, J. Wuskell, H. Clark and K. Loew, Cholesterol-enriched lipid domains can be visualized by di-4-ANEPPDHQ with linear and nonlinear optics Biophysical Journal 90 (2005) 2563-2575.

[39] L. Jin, A.C. Millard, J.P. Wuskell, X. Dong, D. Wu, H.A. Clark and L.M. Loew, Characterization and application of a new optical probe for membrane lipid domains Biophysical Journal 90 (2006) 2563-2575.

[40] Y. Wang, G. Jing, S. Perry, F. Bartoli and S. Tatic-Lucic, Spectral characterization of the voltage-sensitive dye di-4-ANEPPDHQ applied to probing live primary and immortalized neurons Optics Express 17 (2009) 984-990.

[41] A.P. Demchenko, Y. Mély, G. Duportail and A.S. Klymchenko, Monitoring biophysical properties of lipid membranes by environment-sensitive fluorescent probes Biophysical Journal 96 (2009) 3461-3470.

[42] Y. Sun, B.R. James, S.J. Rettig and C. Orvig, Oxidation kinetics of the potent insulin mimetic agent bis(maltolato)oxovanadium(IV) (BMOV) in water and in methanol Inorganic Chemistry 35 (1996) 1667-1673.

[43] G.R. Hanson, Y. Sun and C. Orvig, Characterization of the potent insulin mimetic agent bis(maltolato)oxovanadium(IV) (BMOV) in solution by EPR spectroscopy Inorganic Chemistry 35 (1996) 6507-6512.

[44] M. Vermathen, P. Stiles, S.J. Bachofer and U. Simonis, Investigations of monofluoro-substituted benzoates at the tetradecyltrimethylammonium micellar interface Langmuir 18 (2002) 1030-1042.

[45] P.J. Kreke, L.J. Magid and J.C. Gee, ^{1}H and ^{13}C NMR studies of mixed counterion, cetyltrimethylammonium bromide/cetyltrimethylammonium dichlorobenzoate, surfactant solutions: the intercalation of aromatic counterions Langmuir 12 (1996) 699-705.

[46] J. Stover, C.D. Rithner, R.A. Inafuku, D.C. Crans and N.E. Levinger, Interaction of dipicolinatodioxocanadium(V) with polyatomic cations and surfaces in reverse micelles Langmuir 21 (2005) 6250-6258.

[47] E. Gaidamauskas, D.P. Cleaver, P.B. Chatterjee and D.C. Crans, Effect of micellar and reverse micellar interface on solute location: 2,6-pyridinedicarboxylate in CTAB micelles and CTAB and AOT reverse micelles Langmuir 26 (2010) 13153-13161.

[48] B. Baruah, J.M. Roden, M. Sedgwick, N.M. Correa, D.C. Crans and N.E. Levinger, When is water not water? Exploring water confined in large reverse micelles using a highly charged inorganic molecular probe Journal of the American Chemical Society 128 (2006) 12758-12765.

[49] P. Oh and J.E. Schnitzer, Segregation of heterotrimeric G proteins in cell surface microdomains Molecular Biology of the Cell 12 (2001) 685-698.

[50] C.L. Manahan, M. Patnana, K.J. Blumer and M.E. Linder, Dual lipid modification motifs in Gα and Gγ subunits are required for full activity of the pheromone response pathway in *Saccharomyces cerevisiae* Mol Biol Cell 11 (2000) 957-68.

[51] A. Viola, R.L. Contento and B. Molon. in Immunological Synapse (Saito, T. and Batista, F.D., eds.), Vol. 340, pp. 109-122, Springer Berlin Heidelberg 2010.

[52] D. Lingwood and K. Simons, Lipid rafts as a membrane-organizing principle Science 327 (2010) 46-50.

[53] S. Vainio, S. Heino, J.-E. Mansson, P. Fredman, E. Kuismanen, O. Vaarala and E. Ikonen, Dynamic association of human insulin receptor with lipid rafts in cells lacking caveolae EMBO Reports 31 (2002) 95-100.

[54] J. Sánchez-Wandelmer, A. Dávalos, E. Herrera, M. Giera, S. Cano, G. de la Peña, M.A. Lasunción and R. Busto, Inhibition of cholesterol biosynthesis disrupts lipid raft/caveolae and affects insulin receptor activation in 3T3-L1 preadipocytes Biochimica et Biophysica Acta (BBA) - Biomembranes 1788 (2009) 1731-1739.

[55] K.-B. Kim, B.-W. Kim, H.-J. Choo, Y.-C. Kwon, B.-Y. Ahn, J.-S. Choi, J.-S. Lee and Y.-G. Ko, Proteome analysis of adipocyte lipid rafts reveals that gC1qR plays essential roles in adipogenesis and insulin signal transduction Proteomics 9 (2009) 2373-2382.

[56] J. Inokuchi, Membrane microdomains and insulin resistance FEBS Letters 584 (2010) 1864-1871.

[57] S. Tamura, T.A. Brown, J.H. Whipple, Y. Fujita-Yamaguchi, R.E. Dubler, K. Cheng and J. Larner, A novel mechanism for the insulin-like effect of vanadate on glycogen synthase in rat adipocytes Journal of Biological Chemistry. 259 (1984) 6650-8.

[58] S. Pugazhenthi and R.L. Khandelwal, Does the insulin-mimetic action of vanadate involve insulin receptor kinase? Molecular and Cellular Biochemistry 127 (1993) 211-218.

[59] K.G. Peters, M.G. Davis, B.W. Howard, M. Pokross, V. Rastogi, C. Diven, K.D. Greis, E. Eby-Wilkens, M. Maier, A. Evdokimov, S. Soper and F. Genbauffe, Mechanism of insulin sensitization by BMOV (bis maltolato oxo vanadium); unliganded vanadium (VO_4) as the active component Journal of Inorganic Biochemistry 96 (2003) 321-330.

[60] E. Sheets, D. Holowka and B. Baird, Membrane organization in immunoglobulin E receptor signaling Current Opinion in Chemical Biology 3 (1999) 95-99.

[61] R.D. Huby, R.J. Dearman and I. Kimber, Intracellular phosphotyrosine induction by major histocompatibility complex class II requires co-aggregation with membrane rafts J Biol Chem 274 (1999) 22591-6.

[62] M. Karlsson, H. Thorn, A. Danielsson, K.G. Stenkula, A. Öst, J. Gustavsson, F.H. Nystrom and P. Strålfors, Colocalization of insulin receptor and insulin receptor substrate-1 to caveolae in primary human adipocytes European Journal of Biochemistry 271 (2004) 2471-2479.

[63] X. Yang, K. Wang, J. Lu and D.C. Crans, Membrane transport of vanadium compounds and the interaction with the erythrocyte membrane Coordination Chemistry Reviews 237 (2003) 103-111.

[64] D.M. Owen, P.M.P. Lanigan, C. Dunsby, I. Munro, D. Grant, M.A.A. Neil, P.M.W. French and A.I. Magee, Fluorescence lifetime imaging provides enhanced contrast when imaging the phase-sensitive dye di-4-ANEPPDHQ in model membranes and live cells Biophysical Journal 90 (2006) 80-82.

Table 5.1: Percent of total IR distributed in low density, detergent-resistant and high density, bulk membrane fractions following treatment of RBL-2H3 cells with insulin for 1hr, or with BMOV overnight or both insulin and BMOV.

Fractions (sucrose %)	Untreated	Insulin	BMOV[1]	Insulin, BMOV [1]
Low density (<40%)	2±1	21±10 [a]	26±3[a]	28±6[b]
High density (>40%)	98±1	79±10 [a]	74±8[a]	72±1[b]

[1]Values with the superscript a are different from the value for untreated cells using a paired t-test ($p<0.05$). Values with superscript b are different from the value for untreated cells using a paired t-test ($p<0.005$)

Table 5.2: Localization of pIR, pIRS-1 and pAKT in detergent resistant and bulk membrane fractions following treatment with insulin for 1hr, or with BMOV overnight or both insulin and BMOV.

.

	Fractions (sucrose %)	Untreated	Insulin[1]	BMOV	BMOV, Insulin	MβCD[1]	MβCD/Insulin
pIR							
	Low density (<40%)	45±3	66±11	36±8	28±7	12±14[b]	45±13
	High density (>40%)	55±3	35±11	64±8	72±7	88±14	56±13
pIRS-1							
	Low density (<40%)	5±4	62±19[a]	86±5	N.A.	9±1	N.A.
	High density (>40%)	95±4	39±19[a]	14±5	N.A.	91±1	N.A.

[1]Values with the superscript a are different from the value for untreated cells using a paired t-test ($p<0.05$). Values with the superscript b are different from the value for untreated cells using a paired t-test ($p<0.005$).

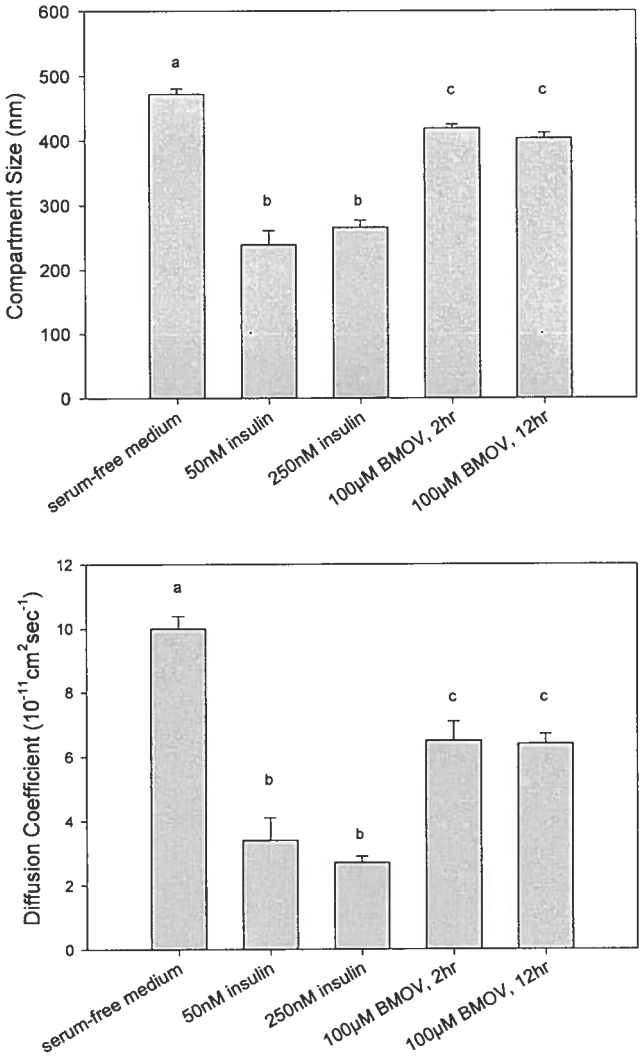
Compartment Size (nm)
600
500
400
300
200
100
0
a
b
b
c
c
serum-free medium
50nM insulin
250nM insulin
100μM BMOV, 2hr
100μM BMOV, 12hr
Diffusion Coefficient (10^{-11}cm^{2}sec^{-1})
12
10
8
6
4
2
0
a
b
b
c
c
serum-free medium
50nM insulin
250nM insulin
100μM BMOV, 2hr
100μM BMOV, 12hr

Figure 5.1

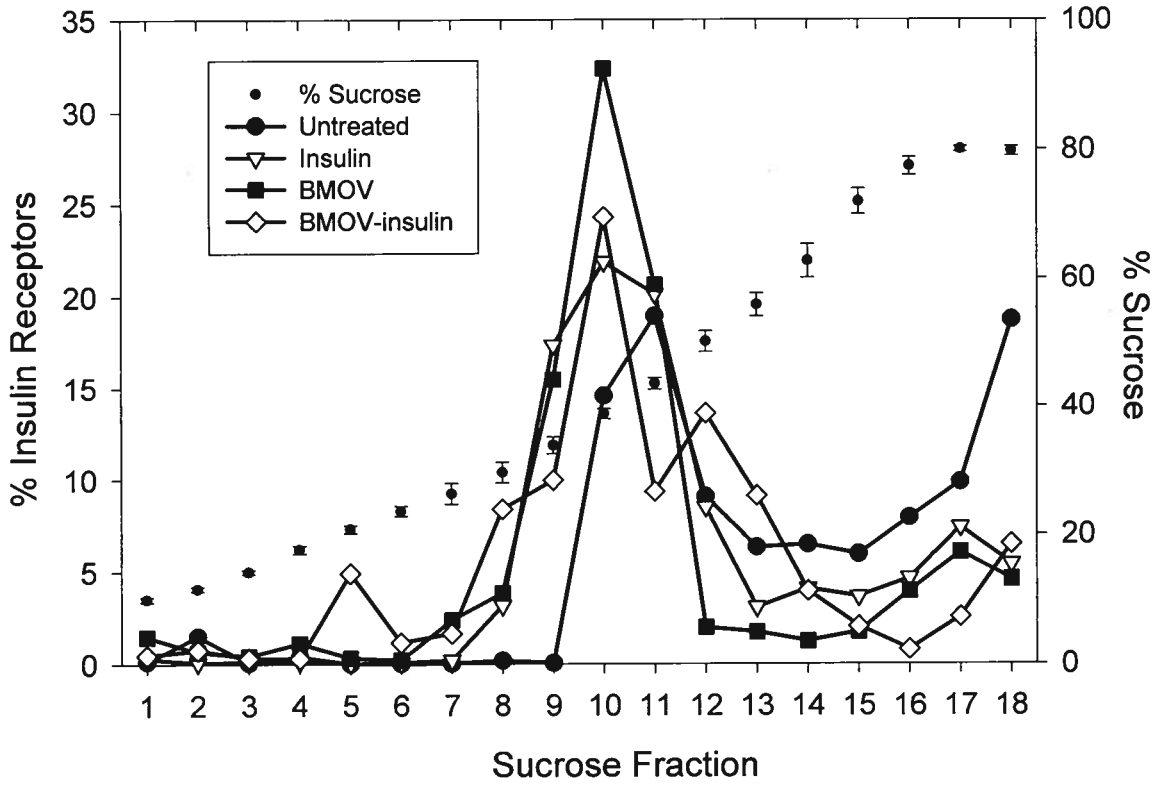
% Sucrose
Untreated
Insulin
BMOV
BMOV-insulin
% Insulin Receptors
% Sucrose
Sucrose Fraction
0
5
10
15
20
25
30
35
0
20
40
60
80
100
1 2 3 4 5 6 7 8 9 10 11 12 13 14 15 16 17 18

Figure 5.2

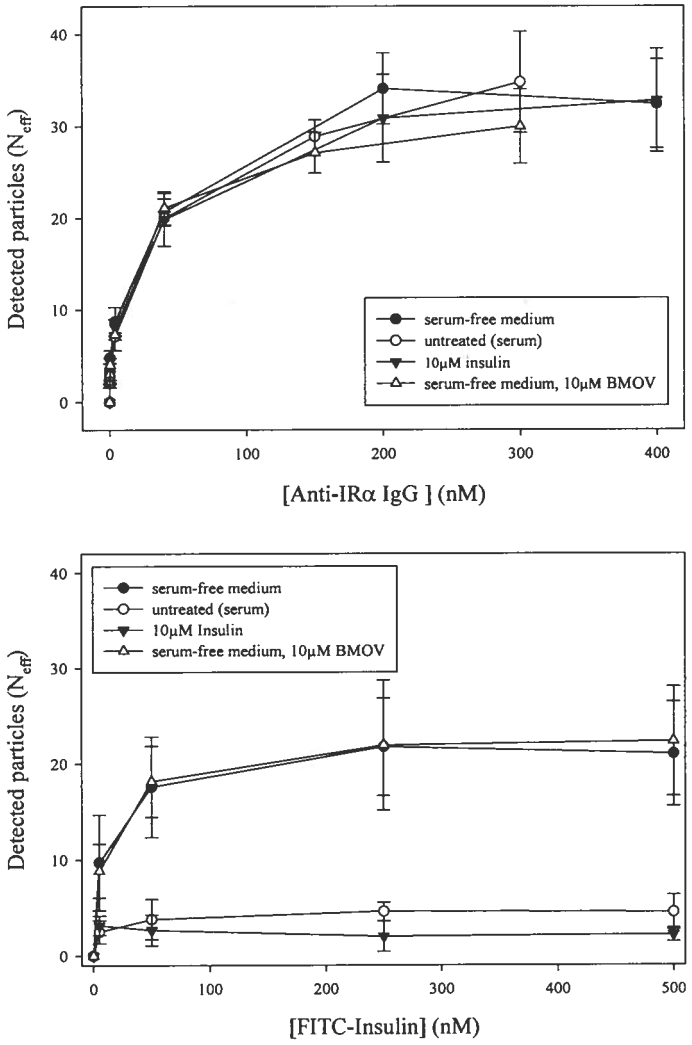
Detected particles (N_{eff})
[Anti-IRα IgG] (nM)
serum-free medium
untreated (serum)
10μM insulin
serum-free medium, 10μM BMOV
Detected particles (N_{eff})
[FITC-Insulin] (nM)
serum-free medium
untreated (serum)
10μM Insulin
serum-free medium, 10μM BMOV

Figure 5.3

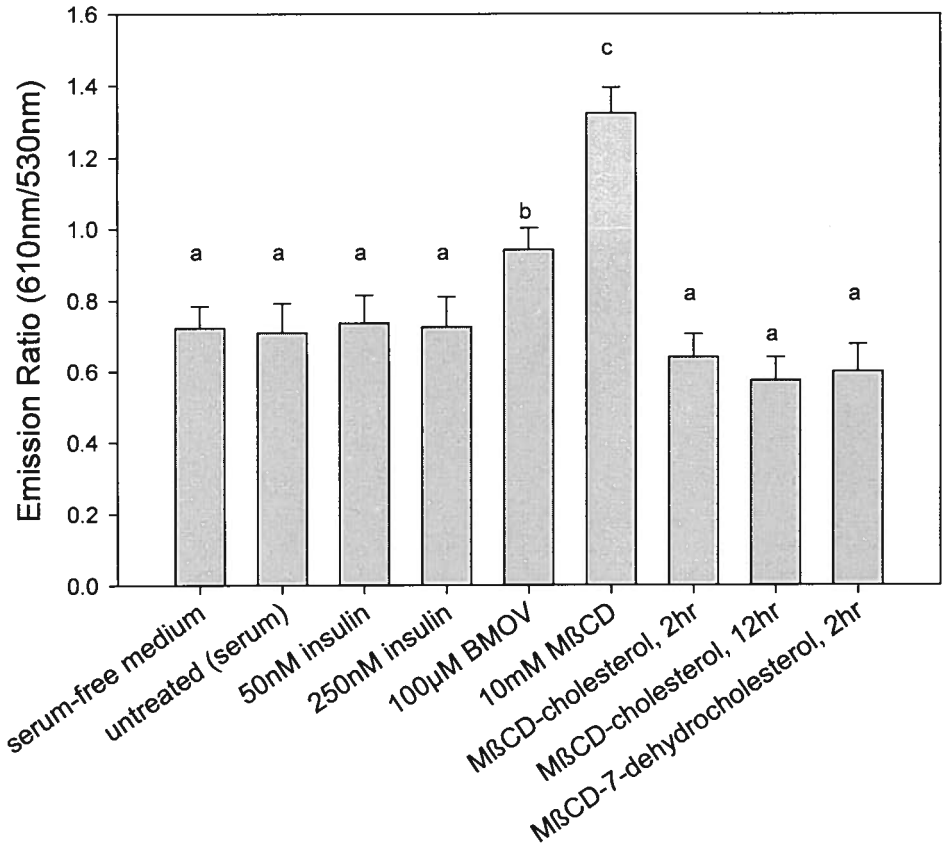
Emission Ratio (610nm/530nm)
1.6
1.4
1.2
1.0
0.8
0.6
0.4
0.2
0.0
a
a
a
a
b
c
a
a
a
serum-free medium
untreated (serum)
50nM insulin
250nM insulin
100μM BMOV
10mM MβCD
MβCD-cholesterol, 2hr
MβCD-cholesterol, 12hr
MβCD-7-dehydrocholesterol, 2hr

Figure 5.4

A.

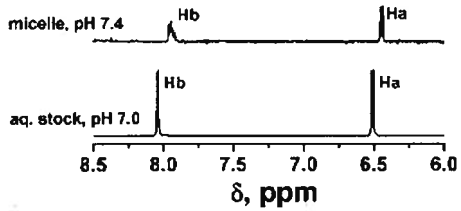

B.

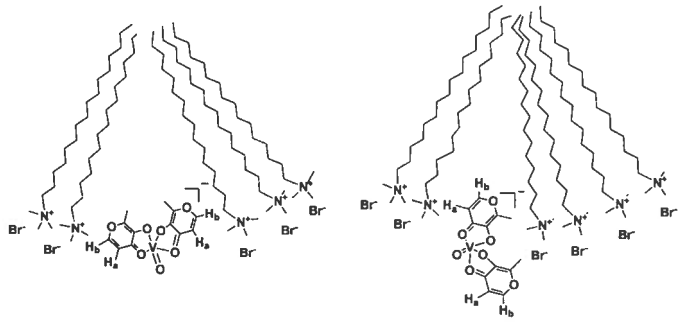

Figure 5.5

CHAPTER VI: Peter W. Winter performed all of the experiments presented herein.

Quantum Dot Probes for Single-Molecule Rotation of Cell Surface Proteins

Peter W. Winter[a], Deborah A. Roess[a] and B. George Barisas[a]

[a]Colorado State University, Fort Collins, CO, USA

Rotation of membrane proteins is a sensitive measure of their aggregation state and interactions. We have investigated the use of asymmetric quantum dots (QD) as non-bleaching imaging probes providing orientation-dependent optical signals from individual cell surface proteins. A commercial QD emitting at 605 nm measures 10.9 x 5.3 nm and exhibits an initial fluorescence anisotropy of 0.11. Calculated rotational correlation times (RCT) for rotations about the particle short and long axes, 0.18 μs and 0.12 μs respectively, suggest that this nanoparticle can probe μs timescale molecular rotation. These QDs, and the related 655nm QDs, conjugated using streptavidin to anti-insulin receptor antibody, are easily visualized bound to 2H3 cell insulin receptors (IR). Blinking of spots demonstrates imaging of individual QDs. We excite fluorescence from cell-bound QDs with non-polarized illumination and record orthogonally-polarized fluorescence images using an image splitter and an EMCCD camera. Image pairs are separated and one polarization is corrected for the optical path g-factor and for displacement, rotation and dilation relative to the other polarization. Time-dependent fluorescence from regions containing individual QDs in image pairs are extracted and the time-autocorrelation function for polarization fluctuations calculated either from actual polarization

or from a combination of auto- and cross-correlations of polarized fluorescence intensities. Individual 655 nm QDs exhibit peak polarization fluctuations with an RMS amplitude of 0.06. These fluctuations decay over 30-50 ms. Whether this slow decay represents hindered rotation of individual IR or results from crosslinking of multiple receptors by single QDs remains to be determined. Current work involves exploration of more highly-asymmetric QDs, use of faster detection methods and examination of the 2H3 cell Type I Fcε receptor where rotational dynamics on faster timescales have previously been explored in detail.

Supported by NIH grant RR023156 and NSF grant CHE-062826.

CONCLUSION

We have described the utilization of a variety of microscopic- and spectroscopic-based biophysical techniques to quantitatively examine the motions, interactions and local environment of transmembrane proteins on living cells at the single-molecule level. Our studies indicate that luteinizing hormone receptors, insulin receptors, insulin-like growth factor type-1 receptors and the high affinity IgE receptor all exhibit significant changes in either their motions, interactions with other lipids and proteins or local environment after exposure to receptor-specific ligands or to reagents that alter membrane composition. We have also shown that often these changes in receptor motions and interactions are accompanied by a redistribution of the receptors into or out of specialized lipid and cytoskeletal protein delineated membrane microdomains, known to be involved in cell signaling.